Development of a Novel Electron Detector with 80 kHz Frame Rate for Imaging Applications: Simulation of the Detector Response and First Experimental Results

Dissertation zur Erlangung des Doktorgrades

des Fachbereiches Physik

der Universität Hamburg

vorgelegt von

Ibrahym Dourki

Hamburg, 2019

Gutachter der Dissertation:	Prof. Dr. R. J. Dwayne Miller Prof. Dr. Günter Huber
Zusammensetzung der Prufüngskommission:	Prof. Dr. R. J. Dwayne Miller Prof. Dr. Günter Huber Prof. Dr. Daniela Pfannkuche Prof. Dr. Arwen Pearson Prof. Dr. Nils Huse
Vorsitzende der Prufüngskommission:	Prof. Dr. Daniela Pfannkuche
Datum der Disputation:	25.05. 2020
Vorsitzender des Fach-Promotionsausscuhsses PHYSIK:	Prof. Dr. Günter Hans Walter Sigl
Leiter des Fachbereiches PHYSIK:	Prof. Dr. Wolfgang Hansen
Dekan der Fakultät MIN:	Prof. Dr. Heinrich Graener

Eidesstattliche Versicherung / Declaration on oath

Hiermit versichere ich an Eides statt, die vorliegende Dissertationsschrift selbst verfasst und keine anderen als die angegebenen Hilfsmittel und Quellen benutzt zu haben.
Die eingereichte schriftliche Fassung entspricht der auf dem elektronischen Speichermedium.
Die Dissertation wurde in der vorgelegten oder einer ähnlichen Form nicht schon einmal in einem früheren Promotionsverfahren angenommen oder als ungenügend beurteilt.

Hamburg, den 20.12.2019

Unterschrift

Zusammenfassung

Die Beobachtung schneller Dynamiken in biologischen Systemen, wie die molekulare Selbstorganisation und Konformationsänderungen von Proteinen kann neue Erkenntnisse über ihre Struktur und Funktion ermöglichen. Es wurden zahlreiche Versuche unternommen, um zeitaufgelöste Dynamiken mittels Transmissionselektronenmikroskopie zu beobachten. Eine große Herausforderung dieser Experimente ist die eingesetzte Detektortechnologie, da die meisten derzeit in der Transmissionselektronenmikroskopie verwendeten Detektoren in Bezug auf die Bildrate noch recht langsam sind oder eine indirekte, auf Szintillation basierende Detektionstechnologie verwenden. Diese Arbeit fokussiert auf Simulationsstudien eines direkten Elektronendetektors, des EDET-80, der mit einer maximalen Bildrate von ca. 80 kHz (12,5 µs Belichtungszeit) arbeitet. Diese beispiellose Geschwindigkeit ermöglicht es dem EDET-80, Echtzeit- und Realraum-Bildgebungsexperimente mit Hilfe eines Transmissionselektronenmikroskops durchzuführen und Filme dynamischer Prozesse schneller als bisher möglich aufzunehmen. Um dieses Ziel zu erreichen, wurde zur Entwicklung dieses Detektors ein innovatives direktes Detektionsschema auf der Basis eines "depleted p-channel field effect transistor" mit nichtlinearem Ansprechverhalten verwendet. Darüber hinaus wurden detaillierte Monte-Carlo-Simulationsstudien durchgeführt, um den Detektor zu modellieren, zu entwerfen und zu charakterisieren sowie die Signifikanz verschiedener Effekte zu untersuchen, die die Abbildungsleistung des Detektors beeinträchtigen können. Die Simulationsstudien und die mit dem ersten EDET-80-Prototyp erzielten Ergebnisse zeigen, dass wir auf dem Weg sind einen leistungsstarken direkten Elektronendetektor zu entwickeln. Des Weiteren können die hier vorgestellten Simulationsergebnisse leicht angepasst werden, um die Leistung anderer direkter Elektronendetektoren zu verbessern. Außerdem wurden auch die Wechselwirkungen simuliert, die

die erreichbare räumliche Auflösung für Flüssigprobenzellen einschränken, die in der Transmissionselektronenmikroskopie eingesetzt werden, um Proben in ihrer natürlichen hydratisierten Umgebung abzubilden.

Abstract

The observation of fast dynamics occurring in biological systems, such as molecular self-assembly and conformational changes of proteins can provide new insights into their structure and function. There have been a great number of attempts to capture time-resolved dynamics by means of transmission electron microscopy. However, a primary challenge of these experiments lies in the employed detector technology, as most of the detectors currently used in transmission electron microscopy are somewhat limited in terms of frame rate or use indirect detection technology based on scintillation. This thesis focuses on simulation studies of a direct electron detector, EDET-80, operating with a maximum frame rate of approximately 80 kHz (12.5 µs frame time). Such unprecedented speed will enable the EDET-80 to carry out real-time and -space imaging experiments by means of transmission electron microscopy and record movies of dynamic processes faster than previously possible. To achieve this goal an innovative direct detection scheme, based on depleted p-channel field effect transistor technology with a non-linear response, is under development. We carried out detailed Monte Carlo simulation studies to model, design and characterize the detector and investigate the significance of several effects influencing the detector imaging performance. The simulation studies and the initial results delivered by the first EDET-80 prototype are promising a new direct electron detector with unprecedented time resolution. Moreover, the simulation results presented here can be readily adapted to advance the performance of other direct electron detectors. Furthermore, we also simulated the underlying effects limiting the achievable spatial resolution for liquid cells that are employed in transmission electron microscopy to preserve samples being imaged in their hydrated environment.

Contents

List of Figures

List of Tables

List of Publications

1. ***"Characterization and optimization of a thin direct electron detector for fast imaging applications"***,
   I. Dourki, F. Westermeier, F. Schopper, R.H. Richter, L. Andricek, J. Ninkovic, J. Treis, C. Koffmane, A. Wassatsch, I. Peric, S.W. Epp, and R.J.D. Miller, *Journal of Instrumentation*, **12**, C03047 (2017).

2. ***"Simulation of EDET-80 detector: A direct electron detector with 80 kHz frame rate for fast electron microscopy imaging applications"***,
   I. Dourki, F. Westermeier, F. Schopper, L. Andricek, R. Richter, J. Ninkovic, J. Treis, I. Peric, C. Koffmane, A. Wassatsch, E. Pinker, M. Polovykh, M. Predikaka, S. Epp, and R. J. D. Miller. (Manuscript, 2019).

List of Abbreviations

ADC	**A**nalogue to **D**igital **C**onverter
BSE	**B**ackscattered **E**lectrons
CCD	**C**harge **C**oupled **D**evice
CMOS	**C**omplementary **M**etal−**O**xide **S**emiconductor
CHC	**C**harge **H**andling **C**apacity
DEPFET	**DE**pleted **P**−channel **F**ield **E**ffect **T**ransistor
DE	**D**etection **E**fficiency
DMC	**DEPFET M**ovie **C**hip
DQE	**D**etective **Q**uantum **E**fficiency
DSSC	**DEPFET S**ensor with **S**ignal **C**ompression
ESF	**E**dge **S**pread **F**unction
FWHM	**F**ull-**W**idth at **H**alf **M**aximum
LSB	**L**east **S**ignificant **B**it
MTF	**M**odulation **T**ransfer **F**unction
PE	**P**rimary **E**lectron (**E**lectrons)
PSF	**P**oint **S**pread **F**unction
ROI	**R**egion **O**f **I**nterest
SNR	**S**ignal−to−**N**oise **R**tio
TEM	**T**ransmission **E**lectron **M**icroscopy (**M**icroscope)
LSF	**L**ine **S**pread **F**unction
XFEL	**X**-Ray **F**ree **E**lectron **L**aser

This thesis is dedicated to my great parents

My dearest wife and my lovely daughters

My beloved brothers and sisters
Thank you for your love, endless support and encouragement.

Chapter 1

Introduction

1.1 Motivations

Transmission Electron Microscopy (TEM) is one of the most powerful imaging tools available for biologists, physicists, and material scientists enabling acquisation of high resolution images to the near atomic resolution. Recent years have witnessed great improvements in image recording, processing techniques, as well as instrumentation such as sample environments and nanofluidic devices [1]. Moreover, a significant enhancement in spatial resolution has been realized by introducing energy filters (i.e. monochromators) and correcting the effects of spherical aberration [2, 3, 4, 5]. With these recent advances, the currently available electron microscope technology offers access to practically all object sizes, ranging from proteins [6, 7] to viruses [8, 9] and to the whole cell [10]. To a greater extent, researchers have demonstrated that it is possible to achieve near atomic resolution for specimens frozen in their hydrated environment (i.e. Cryogenic electron microscopy) [11, 12, 13, 14, 15] or completely dry specimens [16]. Unfortunately, under these conditions, the exploration of dynamic biological processes in their native aqueous environment is greatly impeded or completely infeasible.

Biological systems, such as cells, are complex systems containing a multitude

of different macromolecules, lipids, and nucleic acids. Additionally, these systems exhibit dynamic behaviors to accomplish their predefined tasks. These dynamic behaviors encompass a broad range of scales across both time and space, ranging from femtoseconds to hours and from angstroms to micrometers [17, 18]. Ideally, the visualization of fast dynamics occurring in living systems can provide new insights into the structure and function of these systems. Thereby guiding scientists to develop a fundamental understanding of the relationship between structure and dynamics with function. For instance, in situ-observation of molecular self-assembly (e.g. DNA origami), as well as conformational changes of proteins (e.g. protein folding and unfolding) via TEM can reveal fundamental mechanisms of biological systems. Therefore, the question arises: what is the necessary temporal resolution and frame rate required to capture such dynamics, and what are the boundary conditions to achieve this goal?

There have been a great number of attempts to capture time-resolved dynamics by means of TEM [19, 20, 17, 21, 22, 23]. However, a key problem with these experiments lies in the employed detector technology, as most detectors used in electron microscopy are somewhat limited in terms of frame rate, or in their detection process. On the one hand, difficulties arise from the inherently low contrast of biological specimens—as they consist mainly of low atomic number elements (i.e. hydrogen, carbon, nitrogen and oxygen), and are sensitive to radiation damage. On the other hand, these specimens must be transparent to the electron beam. Therefore, extremely thin samples of a few tens of nanometers up to maximally 1000 nm in special cases are required. A way forward to observe dynamical processes occurring in biological systems would be by establishing in situ conditions within a TEM by employing a liquid cell [1] and using advanced detector technology capable of catching fundamental dynamic processes with sufficient frame rate and imaging

performance. The aim of this thesis is to perform detailed simulation studies of a direct electron detector termed EDET-80 operating with a maximum frame rate of about 80 kHz (12.5 µs frame time). This detector will be devoted to carrying out real-time and real-space TEM imaging experiments, enabling recording movies of dynamic processes faster than previously possible. With sufficiently fast frame rate a wide range of dynamic processes can be observed in both a biology and material science context. Figure 1.1 gives a glance on some phenomena taking place in biology and material science, with respect to the spatial and temporal resolution required for the observation. It shows that an 80 kHz frame rate is sufficient to capture a significant range of conformational changes occurring on the microsecond to second time scale in biological systems such as protein folding [24, 25, 26]. This unprecedented speed for detectors in TEM applications grants access to a "hitherto" inaccessible "terra incognita".

In the course of this thesis the terms "electron beam" refers to the primary electrons of energy E emitted from the electron source and interacting with the sample and detector to create "electron charges" in form of electron-hole (e-h) pairs. Each electron charge is equal to the charge of the elementary electron. The interaction of primary electrons with matter and the working principle of TEM will be discussed in chapter 2 and chapter 3, respectively.

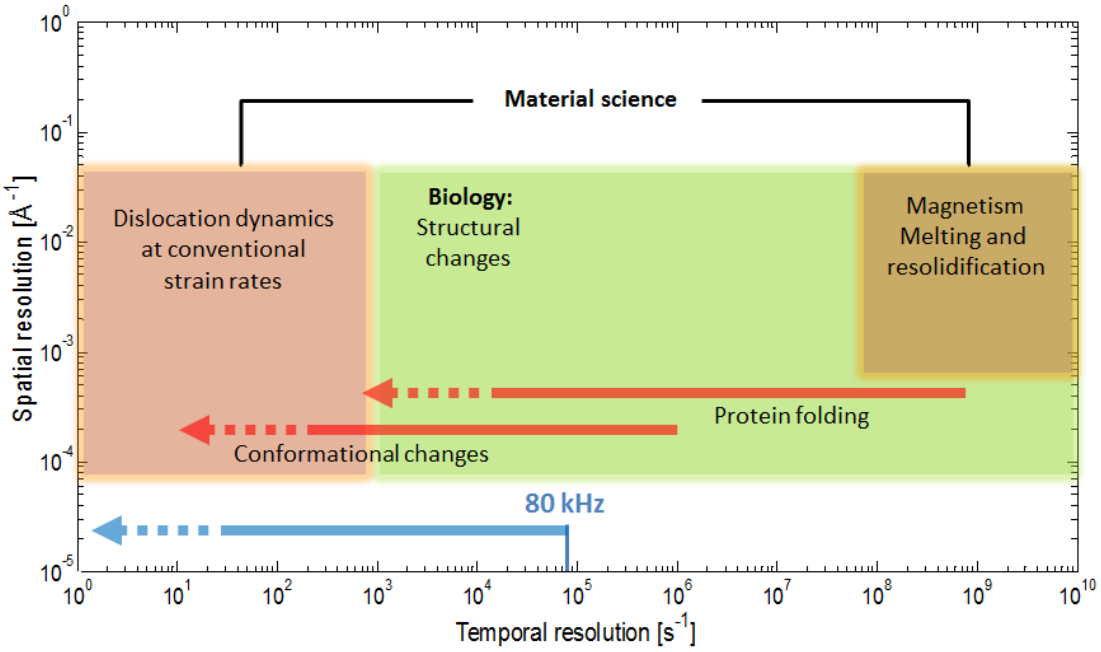

FIGURE 1.1: Classification of some phenomena in biology and material science according to their relevant temporal and spatial scale. The red arrows indicate the time scale of conformational changes and protein folding. The blue arrow shows the temporal range accessible by an 80 kHz frame rate detector. Adapted from [27].

1.2 Commercially Available Detectors for TEM

The first imaging detector used in electron microscopes was the classical photographic film. It was the gold standard for image recording for many decades. Nevertheless, the time-consuming post-processing steps and the digitalization of the films do not allow for direct feedback and high throughput measurements. Film is still used in some TEM applications but has obviously no relevance in capturing sample dynamics.

The advent of digital cameras facilitated the use of TEMs as a ubiquitous scientific tool. Nowadays, the majority of digital cameras are still based on an indirect detection process, where the primary electrons do not generate the detected signal

directly in the sensor, but first interact with a scintillating screen to create optical photons. These photons are subsequently detected by a Charge Coupled Device (CCD) or Complementary Metal-Oxide Semiconductor (CMOS) sensor coupled to the scintillating screen [28, 29, 30, 31] where they are then converted into electronic signal. This indirect detection mechanism has several intrinsic characteristics limiting the detector performance. For instance, the limited spatial resolution due to the spread of photons in the scintillating screen and the optical path (e.g. optical plate or optical fibers) guiding the photons into the sensor. In addition, indirect detectors have a lower detection efficiency.

A promising alternative is direct detection of electrons without a scintillator and optical coupling. Therefore, electrons are converted directly to a digital signal in the sensitive layer of the detector, potentially expanding the use of TEM to new applications [32, 33]. The indirect and direct detection mechanism will be discussed in more detail in chapter 4.

Detectors based on different technologies used in TEM experiments have a common drawback in the achievable frame rate. Currently, frame rate is not sufficient to reveal fast dynamics. Table 1.1 summarizes several important features of some commercially available detectors for TEM imaging applications. Detectors with small pixel size, shown in Table 1.1, can record images with high spatial resolution, but they have limited capability to capture fast dynamics occurring in living systems.

Another parameter which is important when dealing with large signals producing high contrast images is the Charge Handling Capacity (CHC) of a single detector pixel. It measures the maximum charge a pixel can hold, and it is one of the factors determining the achievable dynamic range of the detector. An improved dynamic range has the advantage of facilitating the interpretation of recorded data by minimizing the effect of pixel saturation in a recorded frame and reducing the effect

of the readout noise as presumably less readouts are necessary for the same information contents. Figure 1.2 shows the CHC of different detectors as a function of pixel size. Evidently, large area detectors with small pixels improve the spatial resolution, but at the expense of the CHC (i.e. dynamic range) and subsequently the readout speed, which scales with the number of pixels available in the detector. To achieve the desired frame rate (e.g. 80 kHz in the EDET-80 detector), a compromise between the pixel size and readout time must be found ensuring a sufficient spatial resolution and a wide dynamic range of the detector.

TABLE 1.1: Commercial direct and indirect imaging detectors devoted to TEM applications. Falcon 3EC, K2 Summit, DE-64 and Medipix3 are direct detectors while NanoSprint1200 and BioSprint12 are indirect detectors. M denotes magnification and fps stands for frames per second.

Detector	Pixel length (µm)	Number of pixels	Readout speed (fps)	Å/pixel at M=50,000
Falcon 3EC [34]	14	4096×4096	40	2.8
K2 Summit [35]	5	3838×3710	400	1
DE-64 [36]	6.5	8192×8192	42	1.3
NanoSprint1200 sCMOS [37]	6.8	4096×3008	55	1.36
BioSprint12 CCD [37]	10.8	4000×3200	25	2.16
Medipix3 with Merlin readout system [38]	55	256×256	500	11

The required features of the EDET-80 detector can be realized by adapting semiconductor detector technology available at the Halbleiterlabor (HLL) of the Max

Planck Society in Munich, which has already been introduced in high energy physics detectors devoted for specific applications where the frame rate is a key. In the following section a description of the HLL detector technology in high energy physics is provided and how it can be adapted to our TEM imaging detector.

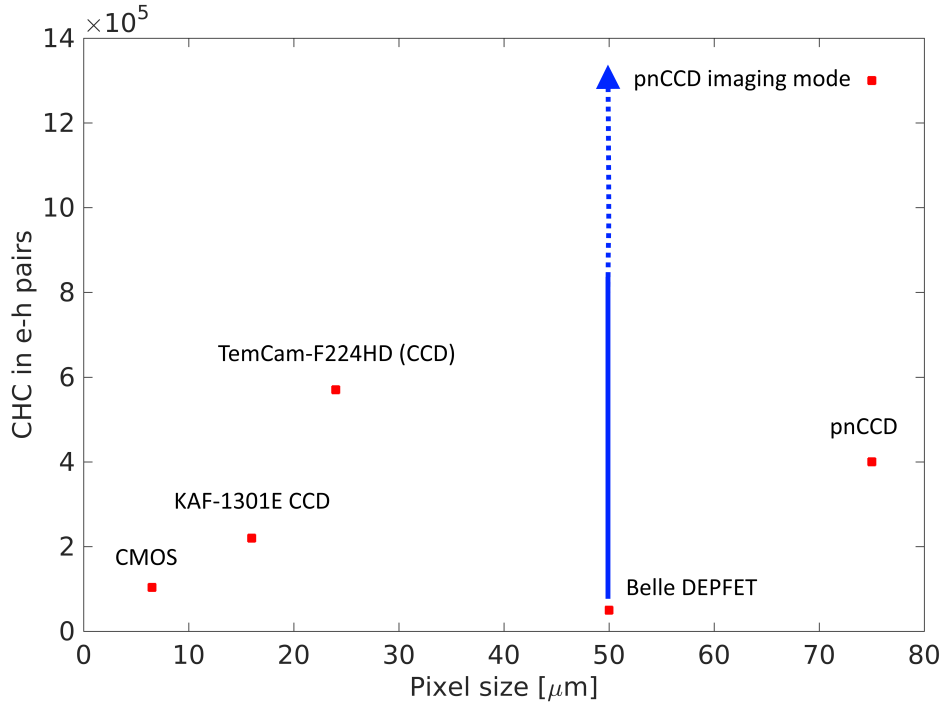

FIGURE 1.2: Charge handling capacity in electron-hole pairs per pixel of different commercial detectors [39, 40, 41, 42].

1.3 From Belle Pixel Detector to EDET-80 Detector

The Japanese Flavor Factory (KEKB B-Factory) located at the high-energy research facility KEK in Tsukuba is a double-ring collider with an 8 GeV electron and 3.5 GeV positron beams devoted to carrying out physics search beyond the Standard Model [43, 44]. The KEKB B-Factory was very successful during its operation from 1998 to 2010. It delivered the world's highest luminosity (2.11×10^{34} cm^{-2} s^{-1}), enabling scientists to demonstrate the violation of Charge-Parity symmetry (CP) in

B meson decays [45] predicted by the Kobayashi–Maskawa theory [46]. Based on this success, the KEKB was upgraded to SuperKEKB with a design luminosity of about 8×10^{35} cm^{-2} s^{-1} [47], which is 40 times higher than that achieved by KEKB. This achievement requires upgrading the Belle pixel detector for Belle II [48, 49] by introducing a new detection technology capable of handling the increased luminosity, reducing the background, high quality data collection with reasonable readout speed and providing high radiation hardness [50, 51]. The silicon sensors of the upgraded version of the Belle pixel detector must be thinned down to 75 µm to minimize multiple scattering effects and thus achieve an enhanced position resolution [52]. The upgrade of the central Silicon Vertex Detector (VXD) was one of the major features of the Belle II detector. The Belle II collaboration decided to use DEpleted P-channel Field Effect Transistor (DEPFET) [53] technology for the new detector as the DEPFET active pixel sensor can fulfill all the requirements set by the Belle II experiments. One of the most challenging aspects of the Belle II DEPFET pixel detector is the readout speed of the full frame, which is about 20 µs (50 kHz) [54].

DEPFET technology has the unique capability to detect and amplify the signal on a pixel level with high signal-to-noise ratio. It has been successfully implemented for experiments in high energy physics to detect particles undergoing fast decays, namely the Belle II DEPFET pixel detector. Transferring the DEPFET detector technology available at the Halbleiterlabor of the Max Planck Society from high energy physics to TEM imaging applications is challenging, as it requires pushing the boundaries of the current DEPFET technology used in Belle II to fulfill the requirements set by a fast readout of TEM images close to 80 kHz. Therefore, several modifications will be introduced in the EDET-80 detector to improve its overall imaging capabilities.

The charge handling capacity of the Belle II DEPFET pixel detector is about 50,000 electron charges per pixel, which is insufficient to capture high contrast TEM images. The CHC can be increased to a reasonable value (e.g. 3 million charges per pixel) by introducing an innovative concept of the signal storage mechanism, which is similar to the DEPFET sensor with Signal Compression (DSSC) at the sensor level. This was developed to perform fast X-ray imaging experiments at the European X-ray Free Electron Laser facility (European XFEL) in Hamburg [55]. A DEPFET with signal compression has the capability to cope with both single electron resolution and large dynamic range due to its non-linear characteristic curve. The desired speed can be achieved by implementing four-fold rolling shutter mode, especially a four-fold parallel readout similar to the Belle II pixel detector. The successful implementation of the DEPFET technology in Belle II experiments inspired us to engage in the EDET-80 project. The DEPFET technology used to develop the EDET-80 detector will be discussed in section 4.4 and section 4.5.

1.4 EDET-80 Project

The development of a new imaging detector requires considerable effort and the implementation of innovative ideas and technology. There are mainly three groups involved in the development of the EDET-80: The Halbleiterlabor (HLL) of the Max Planck Society in Munich, the ASIC- and Detector Laboratory Group of the Institute for Data Processing and Electronics (IPE) in Karlsruhe Institute of Technology (KIT) and the Atomically Resolved Dynamics Division at the Max Planck Institute for the Structure and Dynamics of Matter (MPSD) in Hamburg.

The development of fast readout electronics such as the Drain Current Digitizer (DCD) and the switchers has been mainly performed by the group of Prof. Ivan Peric at KIT. The DEPFET sensor development and fabrication have been done at

HLL in Munich. This includes the coordination of all fabrication processes such as silicon thinning, doping and the assembly of sensors and electronics on a single wafer.

The contribution of the MPSD to this project comprises, for instance, the thermal and electrical engineering, definition of materials and hardware and the fabrication of the mechanical detector design. As well as, the simulation and the optimization of the detector and the analysis of the obtained data.

Collaborative efforts are key for overcoming the challenges we encountered and the success of this project. At the early stage, we carried out simulation studies to investigate and understand the underlying phenomena that degrade detector performance and optimize the most convenient detector design. In addition, simulations offer the unique possibility to build different detector models and test new ideas before implementing them in the detector system. Thus, simulations have the advantage of improving detector imaging capabilities and reducing the fabrication cycles.

Several 3D simulation studies have been performed at different levels ranging from the simulation of a single pixel to the whole detector. Some simulation studies were performed at the HLL, which includes: the thermo-mechanical behavior of the whole detector, electronic readouts as well as the simulation of a $60\times60\times50$ μm^3 DEPFET cell. This encompasses the DEPFET response curve, the potential distribution within the DEPFET cell and the charge storage mechanisms. As a result, an innovative DEPEFT with non-linear response and a large charge handling capacity has been achieved. These desired DEPFET features will be described in detail in section 4.5.

Other simulations have been carried out at the MPSD to investigate the thermo-mechanical stability of the detector and laser annealing—which can serve to mitigate possible radiation damage of the detector. In addition, simulations of the interaction of radiation with detector materials have been also performed using GEANT4 Monte Carlo simulation toolkit [56, 57] to construct the detector, characterize its response and investigate the significance of several effects on the detector performance. In this thesis we started the simulation studies by constructing the detector geometry, irradiating the detector with an electron beam and investigating the resulting signal created in sensitive silicon layers of different thicknesses. This is an essential step to optimize the sensor thickness. We extended our simulation studies to investigate the effects of multiple electron scattering and backscattered electrons on detector imaging performance (e.g. spatial resolution) and charge sharing. Different detector configurations were tested for optimization, thereby showing an improved imaging performance. For example, we developed a new detector design reducing the contribution of backscattered electrons to the total detected signal from 58% to 5%. The effect of backscattered electrons is a serious issue degrading the imaging capabilities of direct electron detectors. The simulation studies of the EDET-80 detector are described in more detail in chapter 5 and chapter 6. The quantification of the imaging capabilities of the EDET-80 detector in terms of Signal-to-Noise Ratio (SNR), Modulation Transfer Function (MTF) and the Detective Quantum Efficiency (DQE) will be discussed in chapter 7. The quantity SNR, as its name indicates, is the detected signal divided by the noise. The quantities MTF and DQE describe the detector spatial resolution and the noise added by the detector to the recorded image, respectively. In addition, simulation studies of the radiation hardness and the shielding of the EDET-80 detector against primary electrons will be presented in chapter 8.

To evaluate the performance of the EDET-80 detector we compared its DQE as a function of spatial resolution to the DQE of current state-of-the-art detectors employed in transmission electron microscopy. This comparison shows that we are on the way to achieve a competitive direct electron detector. Finally, we performed measurements with a first EDET-80 prototype using an X-ray source (e.g. Cadmium-109 radioactive source). The measurements are in good agreement with the simulation results and will be discussed in chapter 9.

The observation of fast dynamic processes, such as dynamics of large proteins, occurring in a hydrated environment not only requires advanced direct electron detectors but also liquid cell technology to probe samples in near-realistic conditions. A liquid cell is a nanofluidic device enabling in situ imaging of objects suspended in water. A typical liquid cell used in TEM is shown in Figure 1.3.

One of the most important factors limiting the attainable TEM resolution in liquid samples is the thickness of liquid cells [58, 59] as they are several hundreds of nanometers thick and consist of silicon nitride ($\mathrm{Si_2N_3}$) membranes of several tens of nanometers [60, 61]. A thick liquid cell broadens the electron beam and degrades the SNR for biological specimens consisting of low-atomic number materials. In this thesis we also present a Monte Carlo simulation study to address this problem. This includes the factors restricting liquid cell TEM spatial resolution such as the thickness of the water layer, the vertical position of objects inside the liquid cell and the thickness of silicon nitride membranes. We found that the achievable resolution depends on the vertical position of the object within the liquid cell, which confirms the so-called top-bottom effect observed in liquid cell TEM [62]. This effect can be minimized in thinner liquid cells. Optimizing the parameters degrading the quality of liquid cell TEM images allows for better understanding of biological processes in

their native environments. The detail simulation study of liquid cells will be discussed in chapter 10.

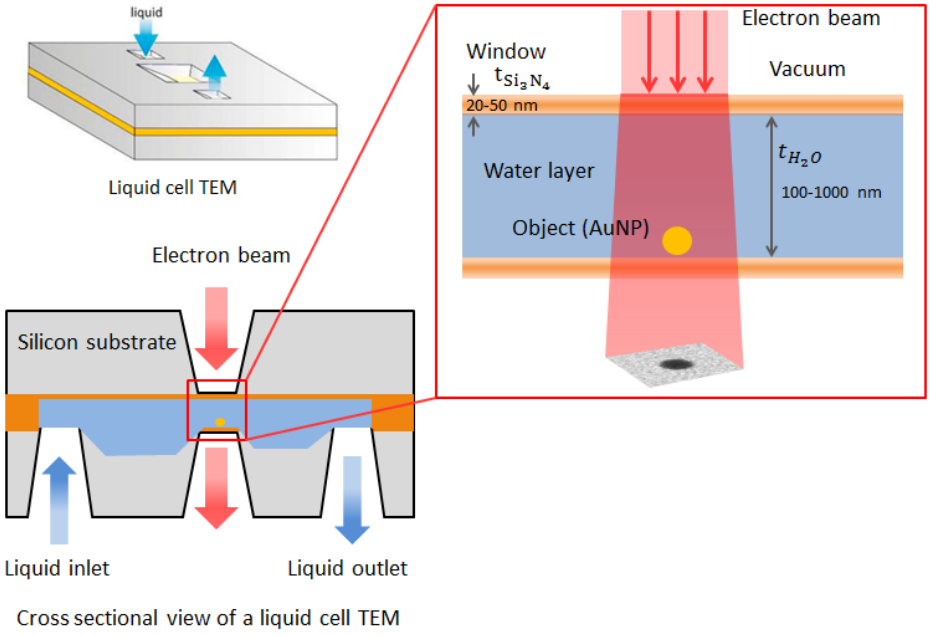

FIGURE 1.3: Liquid cell used in TEM and its cross sectional view. Orange color represents the silicon nitride windows and the blue color represents the liquid layer. Adapted from [1].

Chapter 2

Interactions of Electrons with Matter

This chapter describes the physics of the interaction of electrons with matter, which is fundamental to understand the image formation in a transmission electron microscope and the detection process in an electron detector. Without interaction no information can be obtained from the sample. Accelerated electrons can interact with the sample or pass through it without interactions. As a result, a wide range of signals are produced such as Bremsstrahlung radiation, X-ray and secondary electron emission, as illustrated in Figure 2.1. In general, there are two different types of interactions, namely elastic and inelastic interactions [63, 64, 65].

2.1 Elastic Electron Scattering

In the elastic scattering process the kinetic energy and the momentum of the electrons traversing the sample are conserved and there is thus no energy loss, but the incident electrons can be deflected out of the initial direction by the electric field of the atoms. This results in a lateral spread of the electron beam which leaves the material with an unchanged kinetic energy, E_{kin}, but with a change in travel direction relative to the incident electron beam.

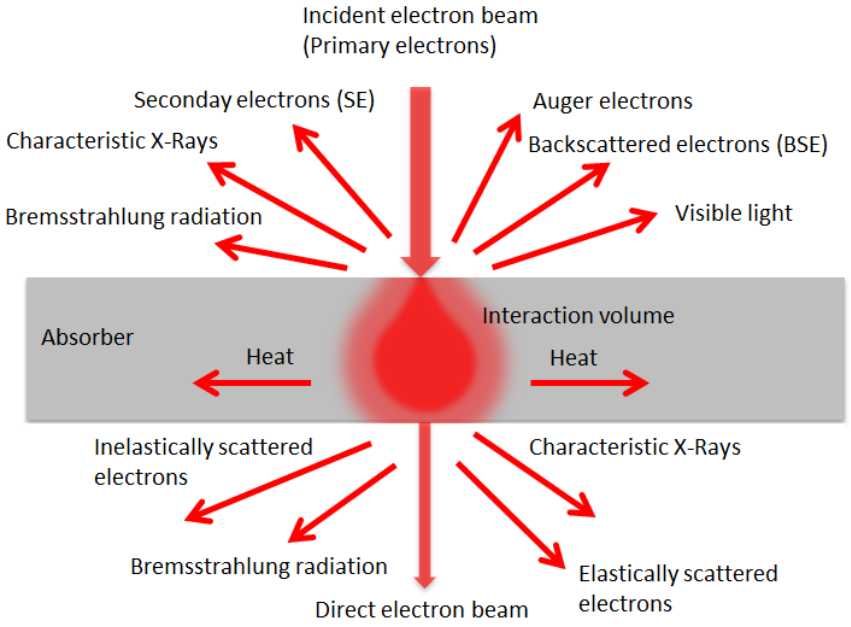

FIGURE 2.1: Interactions of electrons with a thin absorber. Adapted from [64, 66].

Electrons undergoing elastic scattering contribute mostly to the formation of contrast in TEM images. The differential cross-section of the elastic scattering of electrons is given by the following equation [64]

$$\frac{\mathrm{d}\sigma_r(\theta)}{\mathrm{d}\Omega} = \frac{Z^2\lambda_r^4}{64\pi^4 a_0^2\left[\left(\sin(\frac{\theta}{2})\right)^2 + \left(\frac{\theta_0}{2}\right)^2\right]^2}. \tag{2.1}$$

Where Z is the atomic number of the sample, $d\Omega$ is the solid angle, θ is the scattering angle and λ_r is the relativistic wavelength of the electron. The parameters a_0 and θ_0 are given by the following equations

$$a_0 = \frac{h^2\varepsilon_0}{\pi m_0 e^2}, \tag{2.2}$$

$$\theta_0 = \frac{0.117 Z^{1/3}}{E_{kin}^{1/2}}. \tag{2.3}$$

Where ε_0 is the vacuum permittivity and E_{kin} is the kinetic energy of the incident electron.

Equation 2.1 describes the screened, relativistic, differential Rutherford cross-section and it takes into account both the screening effect of the electron cloud defined by θ_0 and the relativistic effects which become significant for electrons with energies larger than 100 keV. Equation 2.1 is widely applied in TEM, but it has some limitations for higher energies above 300 keV and interactions with elements whose atomic number Z is larger than 30 [64]. The integration of equation 2.1 yields the total nuclear cross section, $\sigma_{nucleus}$, for elastic scattering of electrons into angles larger than θ.

$$\sigma_{nucleus} = 1.62 \times 10^{-24} \left(\frac{Z}{E}\right)^2 \cot^2(\frac{\theta}{2}). \tag{2.4}$$

Figure 2.2 shows the dependence of the screened relativistic Rutherford cross-section on the energy of the incident electron and the atomic number of the target. This elastic scattering cross-section has its maximum at very low scattering angles. Hence, most of the elastic scattering events (i.e. 98%) occur at very small angles ($\theta \leq 0.5°$) labeled with the shaded area and less events occur as the angle increases. Decreasing the electron energy from 300 keV to 100 keV increases the elastic scattering cross-section for a silicon sample by a factor of $\sim$9. Increasing the atomic number of the sample from Z=6 (i.e. carbon) to Z=79 (i.e. gold) increases the cross-section by a factor of $\sim$173. This increase in the elastic scattering events can be seen

in Figure 2.3, which shows Monte Carlo simulations of elastic scattering of electrons of 300 keV, 200 keV and 100 keV in a gold (Z=79) and a silicon (Z=14) targets of 100 nm thickness. Interestingly, most of the elastic scattering events have very small angels, as also demonstrated by equation 2.4.

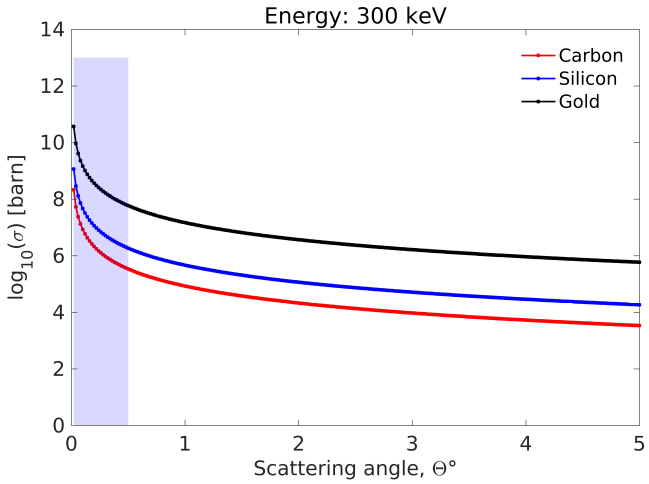

(a)

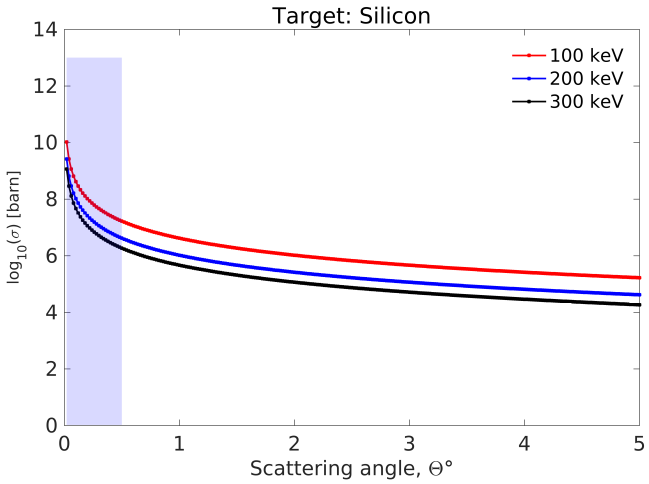

(b)

FIGURE 2.2: The logarithm of the screened relativistic Rutherford cross-section as a function of scattering angles, calculated from equation 2.4. (a) For three elements (carbon, silicon and gold) at 300 keV and (b) for silicon at 100 keV, 200 keV and 300 keV. 1 barn=10^{-24} cm^2.

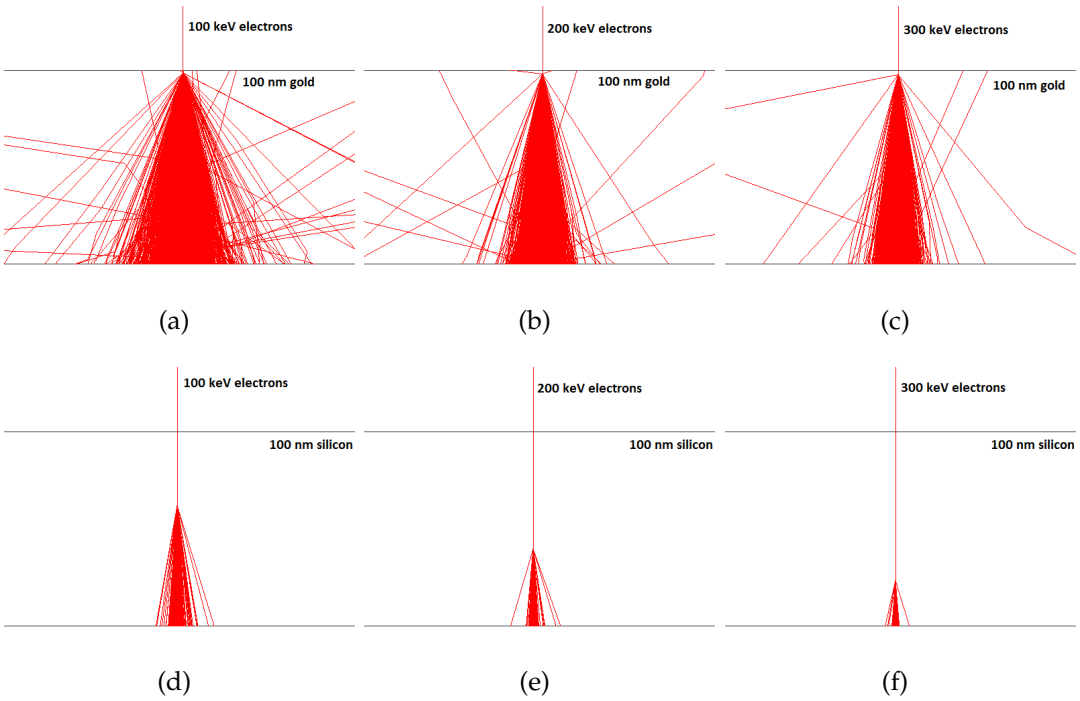

FIGURE 2.3: Monte Carlo simulations of elastic scattering of 2000 electrons in gold and silicon targets of 100 nm thickness. (a) Gold, 100 keV electrons, (b) gold, 200 keV electrons, (c) gold, 300 keV electrons, (d) silicon, 100 keV electrons, (e) silicon, 200 keV electrons and (f) silicon, 300 keV electrons.

Another instructive parameter is the mean free path Λ of elastic scattering. It is defined as the mean distance an electron travels between elastic scattering events and given by

$$\Lambda = \frac{1}{\sigma_{total}} = \frac{A}{\rho N_0 \sigma_{nucleus}}. \tag{2.5}$$

Where A is the atomic weight of the sample atoms, N_0 is the Avogadro's number (N_0=6.022 $\times$ 10^{23} atoms per mole), σ_{total} is the total elastic scattering cross-section and ρ is the density of the sample.

The differential cross-section given in equation 2.4 derived by Rutherford is

based on the classical model treating the electron as a particle and does not take into account the wave nature of electrons. To describe precisely the cross-section of elastic electron scattering, a wave model should be used. The wave behavior of electrons can be considered in the cross section calculation by introducing the concept of an atomic scattering factor $f_e(\theta)$ given by [64]

$$|f_e(\theta)|^2 = \frac{\mathrm{d}\sigma(\theta)}{d\Omega}, \tag{2.6}$$

where $f_e(\theta)$ is the amplitude of an electron wave scattered by an atom and $|f_e(\theta)|^2$ is proportional to the scattering intensity. The scattering factor can well describe the cross-section of elastic scattering at low angles where the Rutherford model is not suitable. The scattering factor, $f_e(\theta)$, is given by the Mott-Bethe formula which relates the electron scattering factor to the X-ray scattering factor $f_x(\theta)$ [67] by

$$\begin{aligned} f_e(\theta) &= \frac{2m_e e^2}{4\pi h^2 \varepsilon_0}\left(\frac{\lambda}{2\sin\theta}\right)^2 (Z - f_x(\theta)) \\ &= 0.023934\left(\frac{\lambda}{\sin\theta}\right)^2 (Z - f_x(\theta)). \end{aligned} \tag{2.7}$$

The values of the X-ray scattering factor $f_x(\theta)$ are available for atoms and ions in the international tables for crystallography, volume C [68].

Using equation 2.7 the variation of the atomic scattering factor as a function of scattering angle for a single isolated atom can be calculated for $\sin(\theta)/\lambda \neq 0$ ($\sin(\theta)/\lambda > 0.02$). Values of $f_e(\theta)$ for $\sin(\theta)/\lambda \leqslant 0.02$ are taken from the international tables for crystallography, volume C, as equation 2.7 becomes less accurate for low values of $\sin(\theta)/\lambda$.

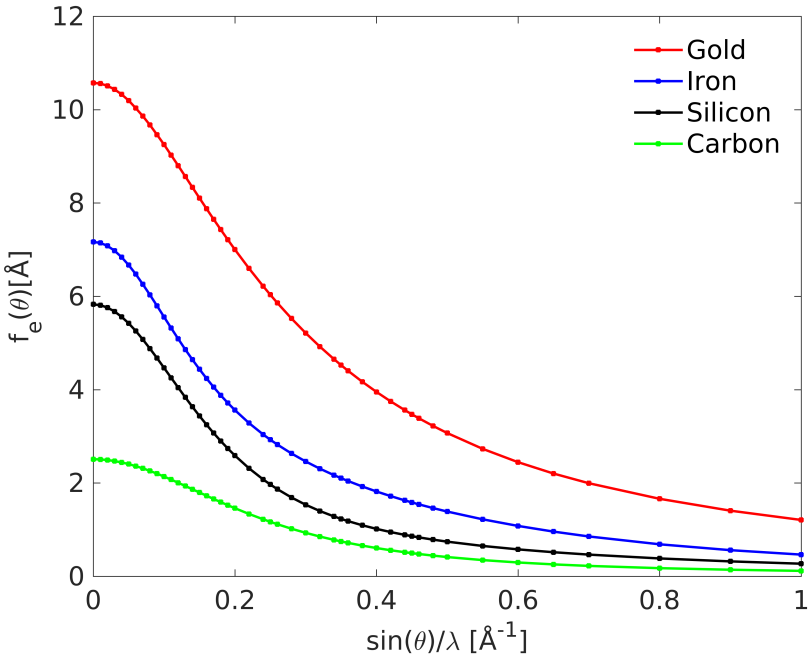

FIGURE 2.4: Atomic scattering factor as a function of scattering angle. It increases as the atomic number of the sample atoms increases and decreases as the scattering angle increases.

As can be seen in Figure 2.4, the atomic scattering factor changes with the wavelength of electrons λ, the scattering angle θ and the atomic number Z of the target. It decreases with increasing scattering angle or decreasing wavelength. For a given scattering angle, it increases as the atomic number increases. $f_e(\theta)$ is large for small angles ($\theta \simeq 0$) and decreases strongly as the scattering angle increases.

2.2 Inelastic Electron Scattering

Inelastic scattering occurs when the incident electrons lose a detectable amount of their kinetic energy, ΔE, as a result of an interaction with the atoms of the sample. Inelastic scattering is always incoherent due to the change of the wavelength and generally has smaller scattering angles compared to elastic scattering [65]. Because

the incident electrons lose energy, change directions and the wavelength, the chromatic aberration of the TEM objective lens becomes significant and deteriorates the image quality, especially as the sample gets thicker and the atomic number becomes smaller so that inelastic scattering dominates [69, 59, 63]. This inelastic scattering contributes to the background and causes also radiation damage while transferring electron energy to the atoms of the samples.

2.3 Energy Loss of Electrons

Electrons deposit their kinetic energy in the material (e.g. detector) they traverse via inelastic scattering. Transmission electron microscopy typically uses electrons in the energy range from 100 to 400 keV to investigate samples [70]. In this range, the energy loss of these electrons by Cherenkov and Bremsstrahlung can be neglected compared to the energy loss by ionization and excitation, which are the dominant mechanism of electron energy loss [71]. The average energy loss for electrons passing through the detector can be approximated using the Bethe-Bloch formula [72, 73] describing the mean energy loss per unit of distance traveled (stopping power) and can be expressed in different forms such as [74]

$$-\frac{\mathrm{d}E}{\mathrm{d}x} = 2\pi N_A r_e^2 m_e c^2 \rho \frac{Z}{A}\frac{z^2}{\beta^2}\Big[\ln\Big(\frac{2m_e\gamma^2\beta^2c^2W_{max}}{I^2}\Big) - 2\beta^2\Big]. \tag{2.8}$$

In this relation, r_e =2.817$\times$ 10^{-13} cm is the classical electron radius, m_e is the electron rest mass ($m_e = m_0$ =511 keV), z is the charge of the incident particle and W_{max} is the maximum energy that can be transfered to a free electron in a single collison and is given by

$$W_{max} = \frac{2m_e c^2 \beta^2 \gamma^2}{1 + 2\frac{m_e}{M}\sqrt{1+\beta^2\gamma^2} + \frac{m_e^2}{M^2}}, \tag{2.9}$$

Where $\gamma = 1/\sqrt{1-\beta^2}$ and M is the mass of the incident particle. For an electron of mass $M = m_e$ equation 2.9 reduces to

$$W_{max} = \frac{2m_e c^2 \beta^2 \gamma^2}{2 + 2\sqrt{1+\beta^2\gamma^2}}. \tag{2.10}$$

The mean excitation potential I depends on the atomic number of the absorbing material and is given by the following equation

$$I = \begin{cases} 12 + \frac{7}{Z}, & \text{for } Z < 13. \\ 9.76 + 58.8 \times Z^{-1.19}, & \text{for } Z \geqslant 13. \end{cases} \tag{2.11}$$

The Bethe-Bloch formula shown in equation 2.8 is the general formula for calculating the energy loss. However, two refinements must be introduced into this equation, namely the density effect correction δ and the shell correction C. These two parameters can be neglected in some cases. The density effect correction is significant at high energies while the shell correction is necessary at low energies. The corrected Bethe-Bloch formula becomes [74, 75]

$$-\frac{\mathrm{d}E}{\mathrm{d}x} = 2\pi N_A r_e^2 m_e c^2 \rho \frac{Z}{A}\frac{z^2}{\beta^2}\Big[\ln\Big(\frac{2m_e\gamma^2\beta^2c^2W_{max}}{I^2}\Big) - 2\beta^2 - \delta - 2\frac{C}{Z}\Big]. \tag{2.12}$$

or

$$-\frac{\mathrm{d}E}{\mathrm{d}x} = K \times \rho \frac{Z}{A} \frac{z^2}{\beta^2} \Big[\ln \Big(\frac{2m_e \gamma^2 \beta^2 c^2 W_{max}}{I^2} \Big) - 2\beta^2 - \delta - 2\frac{C}{Z} \Big]. \tag{2.13}$$

Where the factor K is constant, $K = 2\pi N_A r_e^2 m_e c^2 = 153.54$ keV.cm^2/g.

Figure 2.5 depicts the mean energy loss of electrons in silicon calculated using equation 2.13.

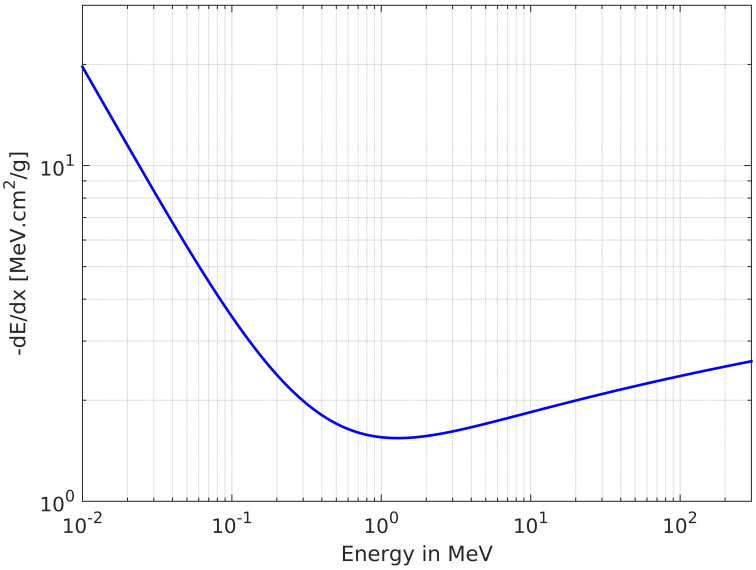

FIGURE 2.5: Mean energy loss of electrons in silicon calculated using the Bethe-Bloch formula given by equation 2.13.

In sufficiently thin materials (e.g. thin detectors), the energy loss of electrons due to ionization is subject to large statistical fluctuations. Obviously, the Bethe-Bloch formula fails to describe these fluctuations which were investigated in depth by Landau. The energy loss distribution of electrons passing through a thin medium can be well described by the Landau distribution [76], which is characterized by a most probable value (mpv). The Landau distribution is described by the following probability density function [76, 74, 77]

$$f(\lambda) = \frac{1}{\sqrt{2\pi}} \exp\left(-\frac{1}{2}\left(\lambda + \exp(-\lambda)\right)\right). \tag{2.14}$$

Here λ is the reduced energy variable given by

$$\lambda = \frac{\Delta E - \Delta E_{mp}}{\xi}, \tag{2.15}$$

where ΔE and ΔE_{mp} are the energy loss and the most probable energy loss, respectively. The quantity ξ is the scale of the Landau distribution comes from the Rutherford scattering cross-section and it is given by the following formula

$$\xi = 2\pi N_a r_e^2 m_e c^2 \rho x \frac{Z z^2}{A\beta^2} = 153.54 \rho x \frac{Z z^2}{A\beta^2} \quad \text{keV}, \tag{2.16}$$

where x is the thickness of the material and the most probable value of the Landau distribution is defined by

$$\Delta E_{mp} = \xi(\ln(\xi) - \ln(\varepsilon) + 1 - C_E), \tag{2.17}$$

where C_E=0.577 is the Euler constant and $\ln(\varepsilon)$ is expressed by

$$\ln(\varepsilon) = \ln\left[\frac{I^2(1-\beta^2)}{2m_e c^2 \beta^2}\right], \tag{2.18}$$

and

$$\beta = \sqrt{1 - \frac{m_e^2 c^4}{(m_e c^2 + E)^2}}. \tag{2.19}$$

For an electron of mass m_e and energy E_e=300 keV traversing 50 µm thick silicon layer whose density is ρ=2.33 g/cm^3, the most probable value can be calculated from the above equations:

ξ=1.4785 keV, β= 0.7765, $\ln(\varepsilon)$= -10.6764 and ΔE_{mp}=16.6586 keV.

The average energy required to generate one e-h pair in silicon is w=3.62 eV [78] and thus the most probable value becomes ΔE_{mp}=4600 e-h pairs for a 50 µm thick silicon layer, 2636 e-h pairs for a 30 µm thick silicon layer and 1691 e-h pairs for a 20 µm thick silicon layer. Figure 2.6 shows examplary the energy deposition of 300 keV electrons passing through a 20 µm thick silicon layer. The energy deposition follows a Landau distribution characterized by the most probable value (mpv). For thick materials, the Landau distribution is no longer valid and the distribution of the energy deposition shows a nearly Gaussian distribution.

Having discussed how the electrons interact with matter, the next section of this thesis describes the working principle of the transmission electron microscope.

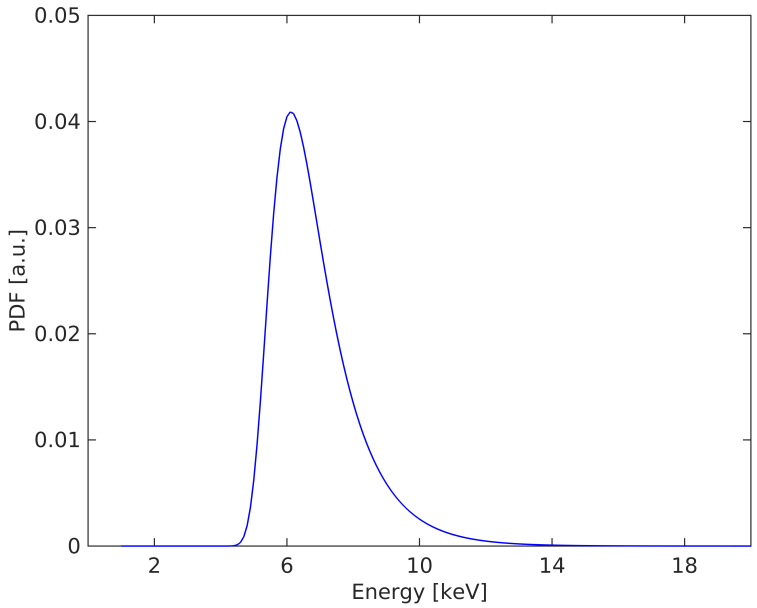

FIGURE 2.6: Distribution of the energy deposited by 300 keV electrons in 20 µm thick silicon layer. The integral of the distribution is normalized to unity to get a probability density function (PDF).

Chapter 3

Transmission Electron Microscopy

In this chapter, the working principle of the Transmission Electron Microscope (TEM) is presented.

The electron microscope was invented in 1930 by two Germans, the engineer Max Knoll and the physicist Ernst Ruska, to solve the problem of spatial resolution in a light microscope which is ultimately restricted by the wavelength of visible light [79]. A transmission electron microscope uses a beam of high energy electrons emitted by a cathode and travelling in a vacuum. These electrons are shaped by circular magnetic lenses to illuminate very thin samples and produce magnified images of the internal structure of the samples being investigated with much higher magnification than an ordinary light microscope. Electrons exiting the sample at different angles as a result of electron-sample interactions will interact with the detector that converts them into a useful signal to form two-dimensional intensity images of the samples.

3.1 Electron Wavelength and TEM Resolution

Electron is an elementary particle carrying a single negative charge of q=-1.602$\times 10^{-19}$ C [80] and a mass of m_e=9.109 $\times 10^{-31}$ kg [80]. However, an electron can not only be

described as a particle but also as a wave characterized by a wavelength λ given by the general form of the De Broglie equation [81]

$$\lambda = \frac{h}{p}. \tag{3.1}$$

Where h=6.626$\times 10^{-34}$ J.s [80] is Planck's constant, $p = m_e v_e$ is the momentum of the moving electron, m_e and v_e are the electron mass and velocity, respectively.
The relationships between kinetic energy of the electron E_{kin}, the momentum p and the accelerating voltage V are given by [82]

$$\begin{aligned} E_{kin} &= \frac{1}{2} m_e v_e^2 \\ &= \frac{p^2}{2m_e} \\ &= eV. \end{aligned} \tag{3.2}$$

By combining equation 3.1 and equation 3.2 we obtain the dependence of the electron wavelength on the accelerating voltage, as shown in the following equation

$$\begin{aligned} \lambda &= \frac{h}{\sqrt{2 m_e E_{kin}}} \\ &= \frac{h}{\sqrt{2 e m_e}} \frac{1}{\sqrt{V}} \text{Å}. \end{aligned} \tag{3.3}$$

Taking into account the values of e, h and m_e yields the following relation

$$\lambda = \frac{12.265}{\sqrt{V}} \text{Å}. \tag{3.4}$$

The velocity of electrons in TEM is about 70% and 78% of the speed of light using an accelerating voltage of 200 kV and 300 kV, respectively [63], thus relativistic effects must be considered. Taking into account Einstein's special theory of relativity, the equation of De Broglie should be rewritten to include these relativistic effects.
The relativistic mass m of an electron is given by [63]

$$m = \gamma m_0, \tag{3.5}$$

in this equation, m_0 is the rest mass of the electron used in classical physics. The relativistic factor γ (i.e. Lorentz Factor) is expressed as follows

$$\gamma = \frac{1}{\sqrt{1 - \frac{v_e^2}{c^2}}} = \frac{1}{\sqrt{1 - \beta^2}}. \tag{3.6}$$

Where $\beta = v_e/c$ and $c = 2.998 \times 10^8$ m/s [80] is the speed of light in a vacuum.
According to the special theory of relativity, the total energy of an electron is given by [63]

$$mc^2 = E_{kin} + m_0c^2 = E_{kin} + E_0. \tag{3.7}$$

Where E_0=m_0c^2= 511 keV is the rest energy of the electron, mc^2 is the total energy of the accelerated electron and E_{kin} is its kinetic energy.
Inserting now equation 3.5 into equation 3.7 leads to

$$v_e = c \times \sqrt{(1 - \frac{1}{(1 + E_{kin}/E_0)^2}}. \tag{3.8}$$

Using an accelerating voltage of V=200 kV the velocity of electrons becomes v_e=2.0859$\times 10^8$ m/s and reaches thus 69.53% of the speed of light.
The relativistic momentum is given by

$$p_r = \frac{m_0 v_e}{\sqrt{1 - \beta^2}}. \tag{3.9}$$

This yields

$$m^2c^4 = p_r^2c^2 + m_0^2c^4. \tag{3.10}$$

Now the relativistic wavelength, λ_r, of the electron is obtained [82]

$$\begin{aligned} \lambda_r = \frac{h}{p_r} = \frac{hc}{p_r c} &= \frac{hc}{\sqrt{(E_{kin} + m_0c^2)^2 - (m_0c^2)^2}} \\ &= \frac{hc}{\sqrt{E_{kin}(E_{kin} + 2m_0c^2)}}. \end{aligned} \tag{3.11}$$

Replacing hc in equation 3.11 with $\lambda c\sqrt{2m_0E_{kin}}$ results in equation 3.12, which relates the relativistic wavelength, λ_r, to the non-relativistic wavelength, λ, of the

electron

$$\lambda_r = \frac{\lambda}{\sqrt{1 + \frac{E_{kin}}{2m_0c^2}}}. \tag{3.12}$$

As $E_{kin}/2m_0c^2 \geqslant 0$, this equation demonstrates that the relativistic wavelength of the electron is smaller than the non-relativistic wavelength, which has the advantage of enhancing the achievable spatial resolution.

The theoretical resolution d in the transmission electron microscope can be determined by Abbe's equation [83]

$$d = \frac{0.612\lambda}{n \times \sin(\alpha)}. \tag{3.13}$$

Where d is the resolution, α is the half aperture angle and n is the refractive index. The product $n \times \sin(\alpha)$ is called the numerical aperture. In a TEM the vacuum refractive index for electrons is n=1. Furthermore, $\sin(\alpha) \simeq \alpha$ (α is very small angle) and thus equation 3.13 simplifies to

$$d = \frac{0.612\lambda}{\alpha}. \tag{3.14}$$

By inserting λ as given in equation 3.4 d can be expressed by

$$d = \frac{0.7506}{\alpha\sqrt{V}}. \tag{3.15}$$

As a result, the resolution at an accelerating voltage V=200 kV and a half aperture angle α=0.01 rad is d=5.3 nm. The maximum resolution in transmission electron microscope is limited by several factor such as uncorrected spherical and chromatic aberrations, sample preparation or sample thickness.

3.2 Working Principles of TEM

Transmission electron microscope operates comparably to a standard light microscope to a large extent. It uses electrons instead of visible light to obtain high resolution images and electromagnetic lenses instead of glass lenses to shape the electron beam. The basic schematic layout of a TEM is illustrated in Figure 3.1.

TEM consists of four main parts: An electron source, electromagnetic lenses, sample holder and the imaging system, which is of primary importance in this thesis. The electron source generates electrons that are accelerated into vacuum in the microscope column and the condenser lens acts like an optical lens to focus the electrons onto a certain part of the sample. Electrons traversing the sample with large angles are excluded by a condenser aperture and the objective lens focuses the transmitted electron beams to form the first image. An intermediate lens can further magnify the first image and the projector lens projects the electrons onto a detector measuring the final magnified image of the sample.

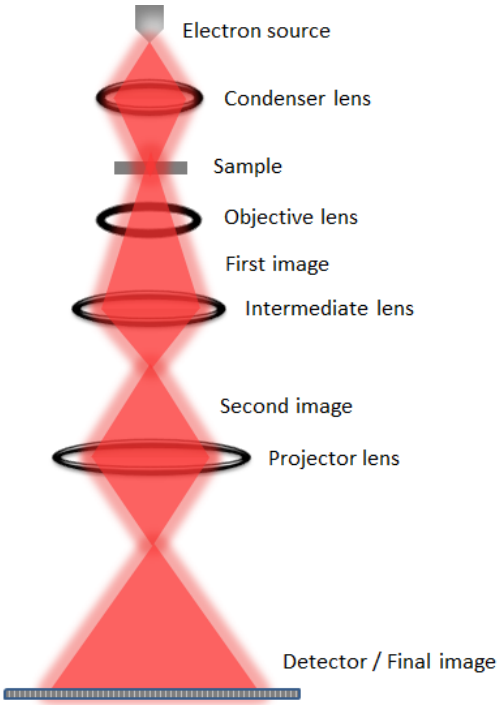

FIGURE 3.1: Schematic diagram of transmission electron microscope. Adapted from [84].

Chapter 4

Electron Detectors for Transmission Electron Microscopy

Transmission electron microscopy has witnessed tremendous technical progress. Nevertheless, electron detectors for TEM applications are often still based on traditional indirect detection technology, which limits the spatial resolution and more importantly constrains the sensitivity. Only recently commercial direct detectors for electron microscopy have been introduced. In this chapter, different types of imaging detectors used in TEM will be discussed. First, photographic films have been used in TEM for a long time and they are still used in some TEM applications. CCD detectors, invented by Boyle and Smith in 1970, were introduced in TEM imaging applications twelve years later (1982) and have dramatically pushed the boundaries of TEM imaging performance. Finally, our direct electron detector (EDET-80 detector) based on DEPFET technology will be presented.

4.1 Photographic Films

Imaging in electron microscopy was for many decades performed by means of photographic film. The film characteristics are a significant Detective Quantum Efficiency (DQE) at high frequency (e.g. Nyquist frequency), a large number of extremely small pixels, excellent spatial resolution and a large active area which provides a wide Field Of View (FOV) [85, 86, 31, 87]. The DQE of photographic film can reach at 300 keV electrons and at half Nyquist resolution about 35% when digitizing with a 6 µm pixel size [85]. Thus, a 10 cm×10 cm photographic film provides a digital image of about 16.6k×16.6k pixels, which is larger than all the images obtained with digital detectors. However, photographic films suffer from several unavoidable disadvantages—films must be mechanically loaded and unloaded in a TEM, backscattered electrons from the film holder contribute to the total generated signal, a narrow dynamic range resulting in very low contrast images and post-processing of the film (e.g. chemical development, washing, drying, optical scanning and digitization). These post-processing steps are complicated and time-consuming, thus preventing immediate access to the recorded data. In addition, photographic films produce images with large contribution of granular noise and are not convenient for recording large data sets. Currently, electronic detectors are increasingly used for electron microscopy applications, but photographic films are still utilized in some electron microscopy applications where high spatial resolution and large FOV are of primary interest.

4.2 Indirect Electron Detectors

The indirect detection mechanism of electrons requires two steps and has, therefore, fundamental limitations degrading detector imaging performance. In the first step, the interaction of primary electrons with a high-Z scintillating screen (e.g. Cesium Iodide (CsI) or Gadolinium Oxysulfide (Gd_2O_2S)), leads to some extent, to the generation of optical photons, which spread isotropically in all directions within the scintillating screen before being detected. This leads to a loss of a large amount of useful photons that can be used to form the image, thus allowing only a small fraction of photons to reach the CCD sensor. Scintillating screens have some intrinsic limitations. Their conversion efficiency is poor and it is, for example, about 15% for CsI:Tl [88], meaning that only 15% of the energy deposition can be converted into photons. Furthermore, the wavelength of the emitted photons is in the order of about 550 nm for most scintillators while the CCD sensor has a peak sensitivity at 700 nm [29] resulting thus in a decreased quantum efficiency (QE) of CCD. In the second step, these optical photons are converted into an electronic signal detected by a CCD or a Complementary Metal-Oxide Semiconductor (CMOS) sensor coupled to the scintillating screen by means of a fiber optic plate [28, 29, 30, 31]. The scattering of electrons and optical photons within the scintillating screen and at the interface of the fiber optic plate restricts the spatial resolution of indirect detectors [89, 90, 91, 92, 93, 94] and leads to a low DQE as well as low Modulation Transfer Function (MTF) [95], which describes the spatial resolution of a detector. The DQE of a fiber-optic coupled CCD irradiated with 300 keV electrons lies between 9% and 13% at hlaf Nyquist resolution [85, 96], about 3 times lower than that of the photographic film. Figure 4.1(a) shows the scattering of a single primary electron of 300 keV and the spread of optical photons created in a 50 µm thick CsI

scintillating screen and Figure 4.1(b) shows the corresponding Point Spread Function (PSF). This PSF becomes much wider as the thickness of the scintillating screen increases, as displayed in Figure 4.1(c, d) for a CsI scintillating screen of 70 µm and 100 µm thickness, respectively. Importantly, increasing the thickness of the scintillating screen improves the detection efficiency and thus the Signal-to-Noise Ratio (SNR), but at the expense of the spatial resolution. These fundamental limitations of scintillating screens restrict the application of indirect detection of electrons in TEM imaging experiments, especially under low-electron dose conditions. Direct detection of electrons can overcome the limitations encountered in indirect detection technology.

CCD cameras are widely used in the transmission electron microscopy, but their readout speed is still the main factor limiting the achievable time resolution in TEM imaging applications. The required time to read out a full frame with a CCD camera is somewhat slow due to the transfer mechanism (i.e. the interline transfer) of the charge created in a CCD pixel, which has a direct impact on the readout speed. Consequently, the acquisition time of the full frame with a CCD camera varies from second to millisecond time scales [97] and it is thus not relevant to capture fast dynamics in biology.

In contrast to the CCD, the CMOS technology has the capability to directly read out the charge in the same pixel allowing for parallel readout of many pixels, which results in an increased frame rate. This process of signal processing on a pixel level consumes much less power than the CCD camera and has the potential to enhance the frame rates [98]. The current generation of CMOS-based detectors are practical for direct electron detection due to their significantly improved radiation hardness [99] and can operate at a typical frame rate of 100-1000 frames per second [96].

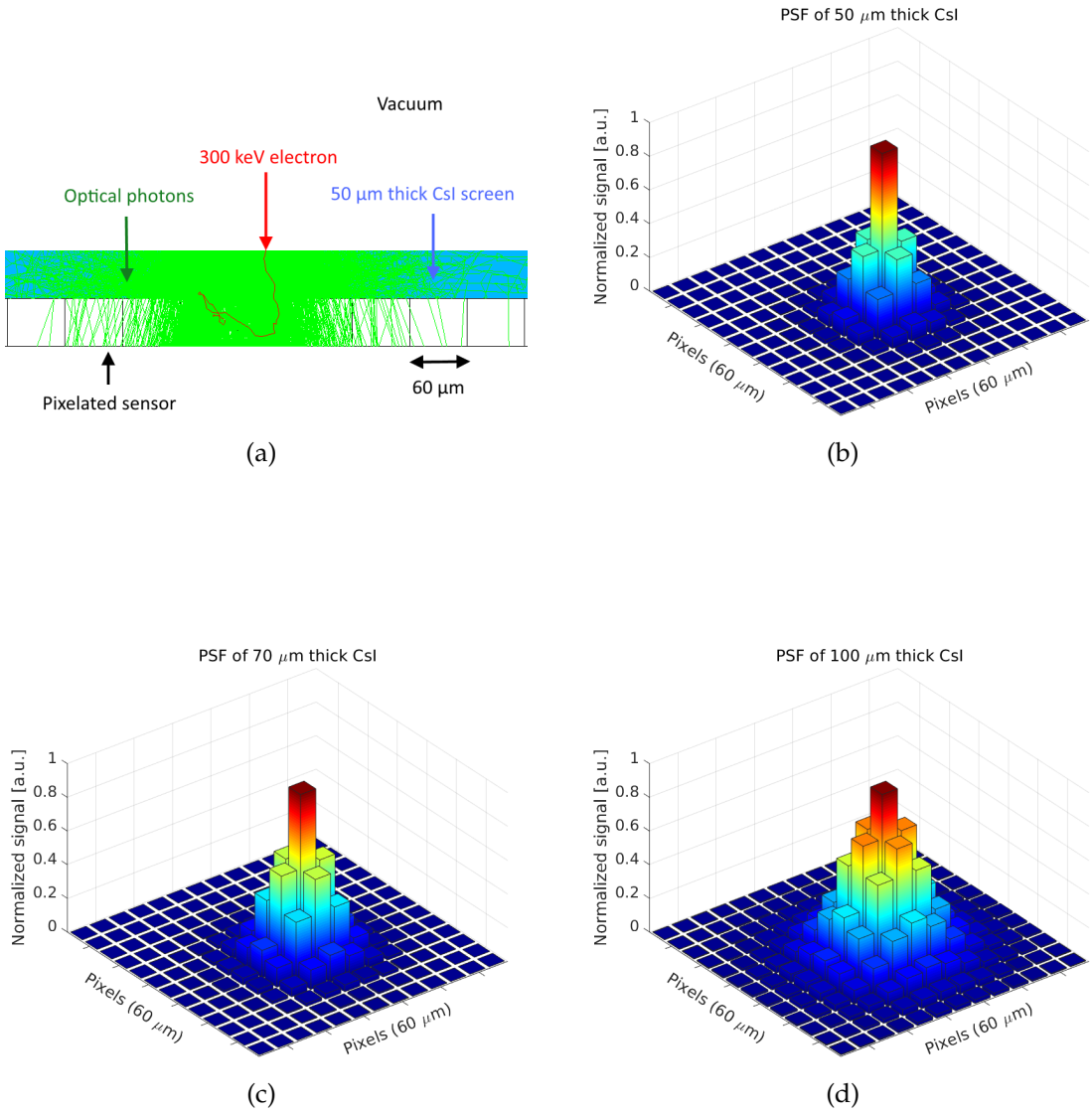

FIGURE 4.1: Simulation of optical photons created in an indirect detector. (a) Scattering and spread of optical photons generated by one primary electron of 300 keV in a 50 µm thick CsI scintillating screen, (b) PSF of optical photons leaving a 50 µm thick CsI screen. (c) PSF of optical photons leaving a 70 µm thick CsI screen. (d) PSF of optical photons leaving a 100 µm thick CsI screen. These simulations were performed with GEANT4 simulation toolkit [56].

The best achievable temporal resolution using a 16 Mega-pixel direct electron detectors based on CMOS is about 2.5 ms [100]. This is still far from our desired temporal resolution (i.e. $\sim$12.5 µs).

4.3 Direct Electron Detectors

Direct electron detectors do not rely on an intermediate light conversion step. They directly convert the energy deposition of primary electrons into electrical signals without a scintillator, providing the highest detection performance such as significant SNR, excellent DQE and high spatial resolution [101, 95, 92, 102, 85, 100, 103]. Figure 4.2 shows a direct electron detector irradiated with an electron beam of 300 keV, the corresponding PSF and the lateral spread of the electron beam, which becomes larger with increasing detector thickness. It is worth noting that the PSF of a direct detector increases as the detector gets thicker, but it is much narrower than that of an indirect detector shown in Figure 4.1. Therefore, direct detectors have dramatically improved the image quality in electron microscopy [32, 101, 103, 100, 23] and, in particular, for low dose applications such as imaging radiation sensitive samples [104].

The main downside of direct detection is the radiation damage, which is a common issue encountered in all kinds of detectors used in TEM and becomes very serious in a direct detection scheme. For example, radiation damage was found to be severe when CCDs were used to directly detect electrons [105], which causes degradation of the performance and the lifetime of the detector [106]. Another limitation of using CCDs as direct detectors is the relatively restricted charge handling capacity of CCD pixels. The huge number of e-h pairs created by primary electrons in the sensor easily exceeds the full well capacity (i.e. charge handling capacity) of

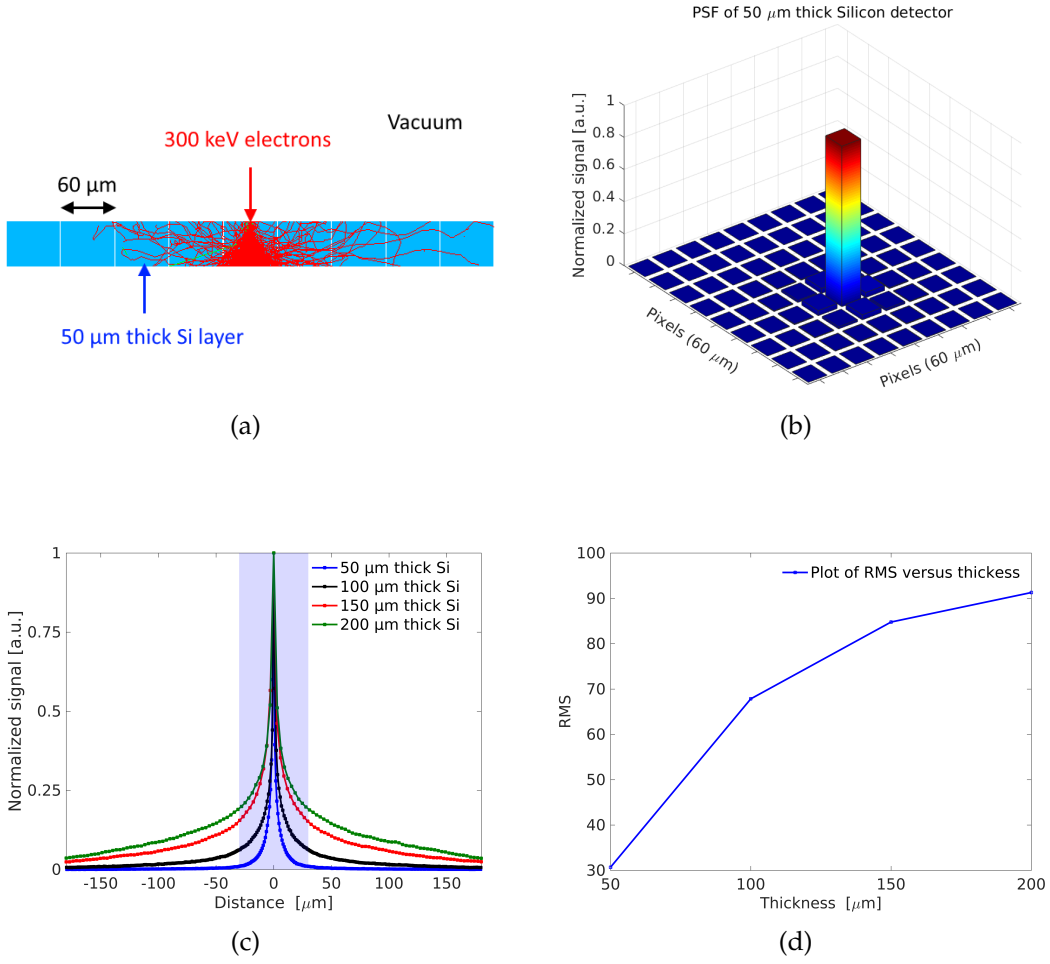

FIGURE 4.2: Simulation of 300 keV primary electrons passing through a direct silicon detector. (a) 300 keV electrons passing through 50 µm thick silicon detector. (b) PSF of electrons in 50 µm thick silicon detector. (c) Lateral spread of a 300 keV electron beam as a function of detector thickness. Shaded area represents the pixel size. (d) Root mean square of the lateral spread as a function of detector thickness.

a CCD pixel. Consequently, a small number of primary electrons will saturate the pixel, resulting in low contrast images.

In summary, most of the detectors used in diverse imaging applications, including those devoted to TEM, do not have a wide dynamic range due to a limited full well capacity, and they are also still relatively slow in terms of frame rate or use an indirect detection process based on scintillators. The direct detection technology of electrons has been used in this work to develop a new detector with improved imaging performance. This can be realized by providing innovative solutions to increase, for example, the frame rate and the dynamic range, decrease the number of scattered electrons from the detector housing and thus achieve a high SNR ensuring single electron detection. A wide dynamic range and a single electron detection capability can be attained by using the DEPFET technology [53]. This technology has already been successfully introduced in high energy physics to build very thin detectors (e.g. DELLE II pixel detector [54]), minimizing multiple scattering of charged particles and providing excellent position resolution. In this thesis, DEPFET technology has been utilized for the first time to develop a direct electron detector and carry out real-space and real-time experiments using a TEM. Therefore, it is useful to understand how a DEPFET pixel detector works.

4.4 DEPFET Pixel Detector

DEpleted P-channel Field Effect Transistor (DEPFET) can be utilized as an active silicon sensor to detect electrons. The structure of a DEPFET pixel is illustrated in Figure 4.3. It combines the detection and amplification of the signal in the same pixel [53] showing thus an excellent noise performance [107, 108]. This can be accomplished by using the so-called sideward depletion technology used in semiconductor drift chambers [109] and integrating a P-channel Field Effect Transistor (FET)

into every pixel on the top of a high resistivity n-type silicon bulk which becomes completely depleted by applying a sufficiently high negative voltage to the back-side p+ contact. The FET has three terminals, namely the source (S), the drain (D) and the external gate (G).

Thinning technology available for silicon [110] provides the possibility to vary the sensor thickness according to the needs of the experiment [111, 112, 113, 114]. In addition, its very good SNR and low power consumption allow building very thin detectors without extra material for cooling and mechanical support [115]. A thin sensor has the advantage of minimizing the effect of multiple electron scattering and charge sharing between neighboring pixels, leading to a narrow point spread function and improved image resolution. A DEPFET can simultaneously detect the incident particle and amplify internally the signal generated in the pixel. Therefore, small signals can also be detected, making DEPFET a convenient detector to detect single electron hits with high probability. It also offers the possibility of repetitive non-destructive readout of the charge signal, thus reducing the readout noise significantly [116, 117].

An ionizing particle (e.g. electron) passing through the sensitive silicon layer, which is the fully depleted n-type silicon bulk of a DEPFET, generates e-h pairs along its trajectory. These charge carriers are separated by means of the electric field created inside the n-type silicon bulk (n-Si bulk). The holes drift toward the backside by applying a sufficiently high negative voltage to the backside p+ contact to make it the most negative node. A deep n-implant located directly underneath the FET channel creates the so-called internal gate by producing a local potential minimum for electrons due to the higher n-concentration. Electrons are thus accumulated in the formed internal gate (regardless of whether the DEPFET is turned on or off) and induce additional charge carriers in the FET channel, which results in an

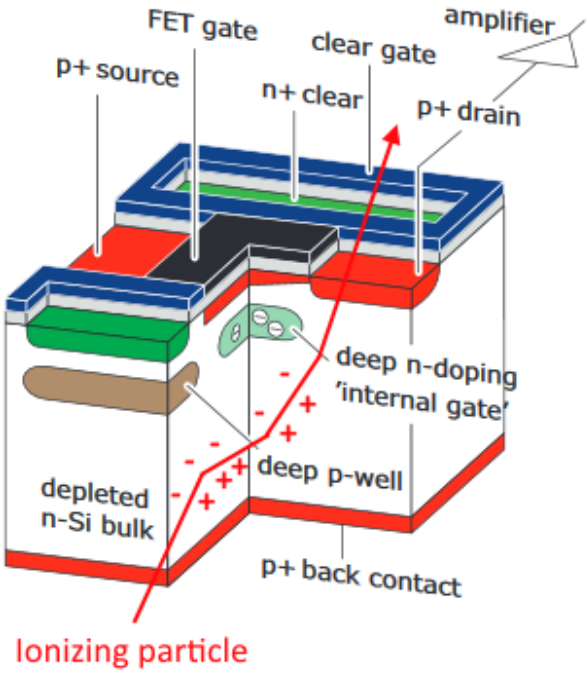

FIGURE 4.3: Structure of a DEPFET pixel. Adapted from [43].

increase of the channel conductance, inducing a current through this channel (i.e. drain current). The drain current is proportional to the number of electrons accumulated in the internal gate and shows an almost linear behavior. This increase in the drain current indicates that a particle has hit the detector and deposited energy. The external gate of the DEPFET switches the pixels on and off. The collected electrons and the thermally generated electrons can be removed from the internal gate by applying a positive voltage pulse to the clear contact, a process that is known as clearing.

If the drain to source voltage V_{DS} and the external gate voltage V_{GS} are constant, the drain current I_D is proportional to the charge accumulated in the internal gate. The DEPFET amplification g_q is given by the following equation [118]

$$g_d = \left.\frac{\delta I_D}{\delta Q}\right|_{V_{GS},V_{DS}}. \tag{4.1}$$

Here δI_D is the change in transistor current caused by the collected charge δQ.

DEPFETs are used in several applications such as biomedical imaging [119], X-ray astronomy [120, 121] and high energy physics experiments [122, 123, 54] (e.g. the Belle II pixel detector). To build a detector with high dynamic range and single hit detection capability, the DEPFET must have a non-linear response (i.e. non-linear amplification).

4.5 DEPFET Pixel Detector with Non-linear Response

The shape of the DEPFET response and the number of bits of the Analog-to-Digital Converter (ADC) are the key factors determining the achievable dynamic range of a DEPFET-based detector. Therefore, the dynamic range can be improved to handle large amounts of charges created in a given pixel by implementing a convenient ADC and improving the charge handling capacity of DEPFET pixels. The signal storage capability can be enhanced by using a concept of signal storage mechanism similar to that of DEPFET Sensor with Signal Compression (DSSC) at the sensor level, which was developed to perform fast X-ray imaging experiments at the European X-ray Free Electron Laser facility (European XFEL) in Hamburg [55]. A DEPFET with signal compression has the capability to cope with both single electron resolution and large dynamic range due to its non-linear characteristic response curve. This can be achieved by extending the internal gate into the region below the source, creating thus overflow regions where charges can also be stored,

improving the charge handling capacity of the detector. That means that small detected charges are completely stored in the internal gate and largely affect the transistor current, while large charges created by high electron doses are additionally stored in the overflow regions and correspondingly have less effect on the transistor current. As a result, a non-linear DEPFET response—which is a non-linear amplification, is achieved giving the required features of single-electron detection capability and the extended dynamic range, which enables the detector to record high contrast images.

The basic concept of a DEPFET with signal compression at sensor level is illustrated in Figure 4.4 and described in more detail in [55, 124]. The technology of a DEPFET with non-linear response has been introduced for the first time in the EDET-80 detector devoted to fast TEM imaging applications. The development of this imaging system is the result of cooperative efforts with the Halbleiterlabor (HLL) of the Max Planck Society in Munich, the ASIC- and Detector Laboratory Group of the Institute for Data Processing and Electronics (IPE) in Karlsruhe Institute of Technology (KIT) and the Atomically Resolved Dynamics Division at Max Planck Institute for the Structure and Dynamics of Matter (MPSD) in Hamburg.

Despite their unique features, DEPFETs suffer from radiation damage induced by the ionizing radiation [115, 126, 114]. This induced radiation damage is mainly caused by the accumulation of positive charge carriers in the oxide layer, which have a direct impact on the voltage applied at the gate contact for readout, thus causing a significant shift of the threshold voltage to more negative values [115, 126, 114]. A threshold voltage is a value of the gate voltage corresponding to the onset of a significant drain current in the transistor. However, it was demonstrated that DEPFETs are still operational after irradiation with doses of 8 Mrad and subsequent temperature annealing [114]. Another study has proved that DEPFETs can tolerate

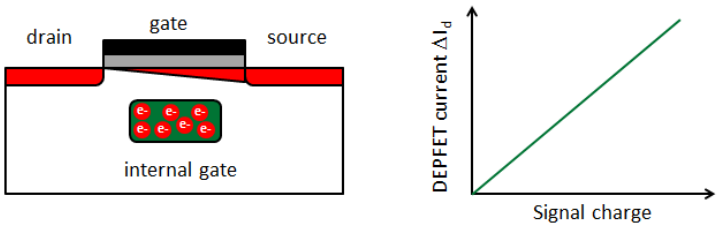

(a)

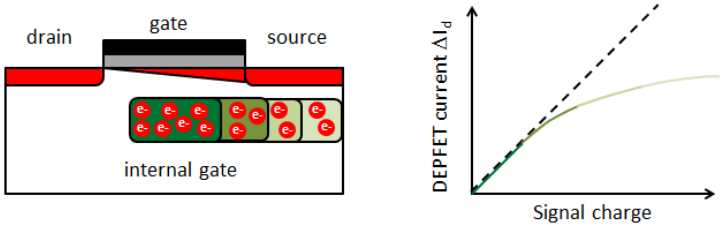

(b)

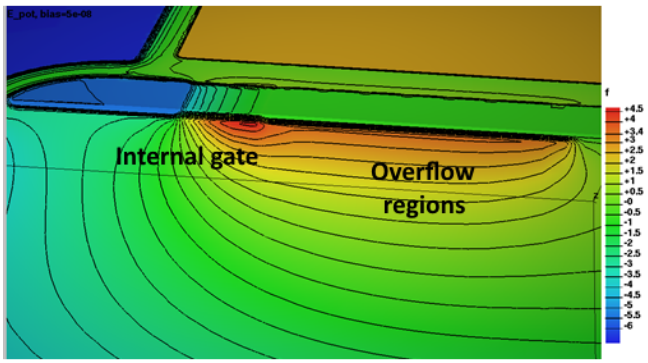

(c)

FIGURE 4.4: Comparison of a standard DEPFET sensor with linear response and a non-linear DEPFET sensor with signal compression. (a) Stantard DEPFET with linear response. (b) DEPFET with non-linear response, the color contrast indicates the variation of the space charge density of the internal gate resulting in a potential depth variation. (a) and (b) are adapted from [124]. (c) Shows the extension of the internal gate below the source and the simulated potential of DEPFET with non-linear response. The electrons are first accumulated in the internal gate because of its most positive potential and when the internal gate is saturated the additional electrons spill over into the overflow regions. This simulation was performed by K. Gärtner and R. Richter using Oskar3 [125].

a radiation dose up to 10 Mrad [43]. The radiation damage of the EDET-80 will be discussed in chapter 8.

4.6 EDET-80 Detector

The electron detector we have developed is a direct-electron-hit silicon detector operating with a maximum frame rate of 80 kHz (80,000 frames per second) and named EDET-80 detector dedicated to exploring fast dynamical processes taking place in biological samples using a TEM. It is one megapixel detector with a total active area of approximately 61.44×61.44 mm^2, offering a wide field of view at high magnification. The EDET-80 detector consists of four identical quadrants, each quadrant having a 512×512 pixel matrix with 60 µm×60 µm pixel size. To be able to detect a high number of electrons of high kinetic energy while maintaining excellent detection efficiency and significant SNR, the sensitive silicon layer is thinned down to 50 µm. All the four quadrants of the EDET-80 detector are read out simultaneously in rolling-shutter mode with column parallel amplification and digitization. The rolling shutter is implemented four-fold to increase the readout speed by a factor of four. As in the Belle II pixel detector based on DEPFET technology [43, 54] one sensor row can be read out in 100 ns and therefore 100 ns×512/4 results in total readout time of 12.8 µs for an entire frame, providing a frame rate of 78.1 kHz. This unprecedented speed is sufficient to capture a large range of dynamic processes occuring in chemistry and biology [127, 27]. It will also allow us to perform dose fractionation experiments and make so-called "molecular movies". For example, 100 frames make a movie of 1.28 ms. It should be noted that a continuous operation of the EDET-80 at 78.1 kHz frame rate will result in a net data rate of about 82 Gigabytes/s. To avoid such a challenge for data transfer and storage, the EDET-80 detector was designed to operate in a burst mode with a maximum rate of

100 bursts per second. Each burst contains up to 100 frames with a time separation of 12.8 µs or 78.1 kHz between subsequential frames. The signals streaming from the sensor are immediately digitized by the Drain Current Digitizer (DCD) of 8-bit resolution and temporarily stored in the Digital Movie Chip (DMC) which can store 100 frames. These stored frames are then transferred to the back-end data storage systems between the bursts.

The EDET-80 detector will be used in a TEM to carry out time-resolved imaging experiments and study the fast molecular dynamics occurring in biological systems. However, biological specimen are very sensitive to the electron beam and therefore a very low electron dose must be used to avoid the radiation induced damage of the sample being imaged [128, 129, 130, 131, 132, 133], which leads to a degradation of the SNR and the contrast of the resulting image. Excellent detective quantum efficiency of the detector is thus needed to improve the image quality for electron-beam sensitive samples. A thin detector based on DEPFET [53] technology with a non-linear characteristic response [55, 124] can fulfill the challenging requirements to build a fast direct electron detector for TEM applications.

Table 4.1 summaries the EDET-80 detector specifications, and Figure 4.5 shows a prototype design and a simplified block diagram of the detector concept presented in this thesis.

TABLE 4.1: Specifications of the EDET-80 detector devoted to fast TEM imaging applications.

Detector parametrs	**Specifications**
Sensor area (4 quadrants)	Area: 61.44×61.44 mm^2 (1024×1024 pixels)
One quadrant	512×512 pixels
Pixel size	60×60 μm^2
Silicon sensor thickness	50 µm
Maximum frame rate (fps)	80,000
Detection efficiency at 300 keV	∼100 %
Operation temperature	-10 °C
Charge handling capacity	up to 3 million electrons
Dynamic range per pixel	up to 325 primary electrons @ 300 keV
ADC (DCD) resolution	8-bits
Number of frames stored in DMC	100
Shutter mode	Four-fold rolling shutter
Data stream	Burst with 100 frames
Readout	DCD + DEPFET Movie Chips (DMC)
DEPFET noise	σ_{d}=9 nA
DCD noise	σ_{dcd}=50 nA
Fano noise	σ_{Fano}=30 e^-

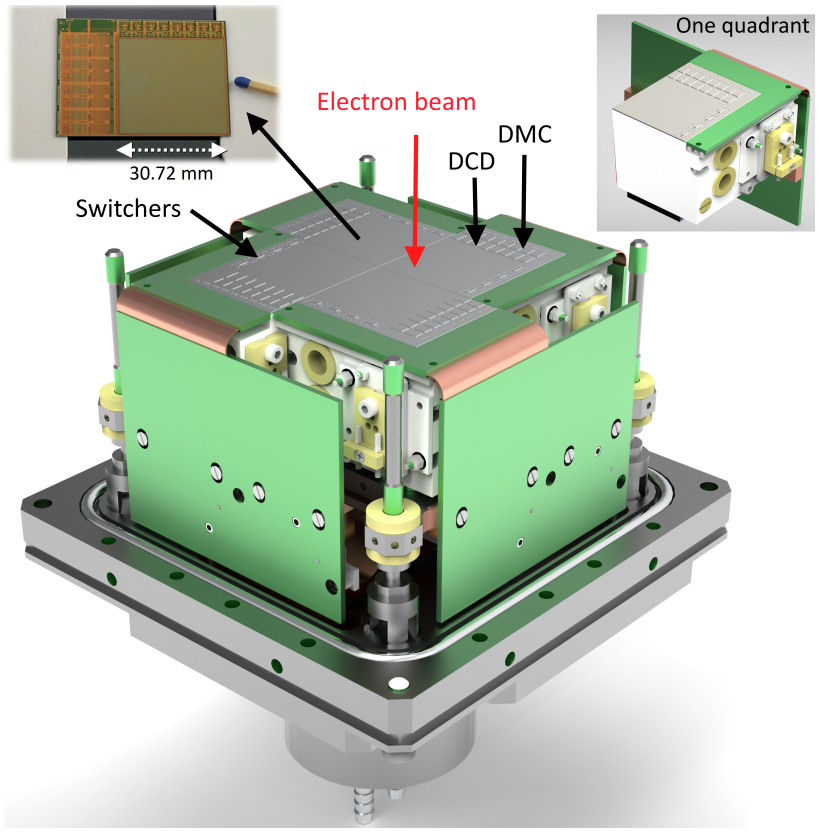

(a)

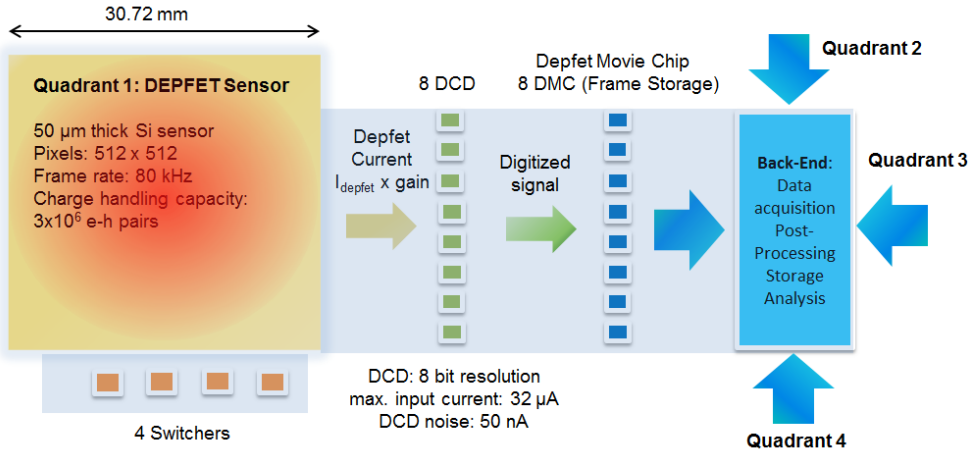

(b)

FIGURE 4.5: Prototype design and a simplified concept of the EDET-80 detector. (a) Shows a 3-D view of the EDET-80 design comprising four quadrants. The inset in the top left shows one of the first produced 50 µm thick silicon sensors and the inset in the top right shows one quadrant of the EDET-80 detector. (b) Illustrates a simplified block diagram of one quadrant of the EDET-80 concept based on DEPFET technology.

After having discussed the TEM detectors and the innovative DEPFET technology implemented in the EDET-80 detector, we move on to describe the simulation studies of this detector. Monte Carlo Simulations are an excellent tool available for designing detectors, characterizing, understanding their response and identifying the most promising detector configuration. Therefore, they play a key role in the process of new detector development. The next chapter describes the Monte Carlo Simulation studies performed in the development process of the EDET-80 detector.

Chapter 5

Simulation of the EDET-80 Detector

In order to develop an innovative detector, characterize its response and investigate the significance of several effects that can degrade the imaging performance of the detector, Monte Carlo simulation studies were carried out. In this chapter, Monte Carlo simulation studies of the EDET-80 detector are presented. This includes the investigation of the signal generated in a silicon sensor of different thicknesses and the effect of backscattered electrons on the total signal created in the sensor. This effect is one the main factors limiting the imaging performance of direct electron detectors.

5.1 Monte Carlo Simulation Tool

Developing a novel direct electron detector for TEM imaging applications is, in fact, a complicated and challenging process. It requires the exploration of the whole detector system, the physics and materials involved in all detector components to achieve the desired detector imaging performance. To facilitate this development process, simulations are thus crucial and necessary. It is the only tool available to accurately predict and understand the behavior of the complete detector system, develop and achieve the best detector performance and experimental setup optimized

for the desired applications. GEANT4 was chosen in this study to model and characterize the EDET-80 detector because it is one of the most advanced and practical simulation tools. GEANT4 is a powerful Monte Carlo simulation toolkit, which stands for Geometry ANd Tracking (version 4). It is a general-purpose Monte Carlo toolkit for the simulation of particles passing through and interacting with materials [56, 57]. It was originally developed for use in high energy physics. But now, it is widely and increasingly used in various research areas such as medical physics, radiation protection, space science, detector development, and nuclear physics. In general, it can be used in any research field involving the interaction of radiation with matter. It is written in C++ programming language and offers a complete range of functionalities required to build flexible simulation frameworks including geometry modeling capabilities, materials involved, event generation and tracking of particles through materials. It is a free software package available from the GEANT4—Collaboration web site [134] and has a complete set of accurate physics models describing the interactions of particles with matter across a very wide energy range spanning from eV to PeV [135, 136]. User-friendly visualization drivers and graphical user interfaces are also supported in this simulation toolkit. Therefore, an efficient particle transport framework like GEANT4 offers a complete set of tools to simulate and predict the detector response based on different scenarios without building and testing all the possible prototypes, which is not a feasible approach.

Figure 5.1 illustrates the simulation architecture of GEANT4. The user has to develop at least three mandatory classes and three optional classes to make a GEANT4 based-application delivering some outputs (e.g. energy deposition in detector). In these simulation studies we used low energy electromagnetic physics "Livermore model", which is relevant to track electrons with high accuracy [137].

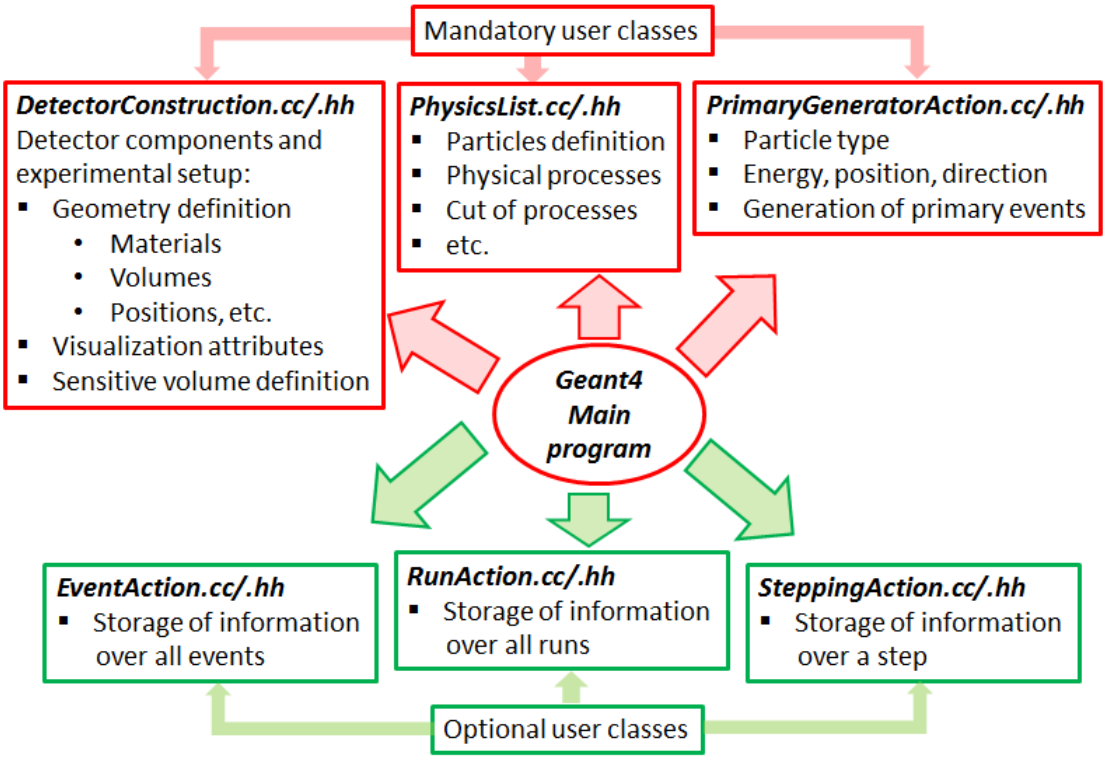

FIGURE 5.1: Mandatory user classes and optional user classes needed to make a GEANT4 application [137, 138].

Here, we used GEANT4 (version GEANT4.9.6.p03) to develop an innovative direct electron detector starting from the exploration of several factors limiting the detector imaging performance such as geometrical parameters of the detector system (e.g. materials involved, detector housing and design, thickness of sensor, etc.) and physical processes (e.g. signal creation by incident electrons, detection efficiency, electron scattering, charge sharing, backscattered electrons (BSE)). Thus, a new direct electron detector showing improved imaging performance compared to other available detectors has been achieved. In addition, the results presented in this work could be a useful aid for detector developers and might be readily adopted to advance the performance of other direct electron detectors.

5.2 Simulation of Signal Generation in Silicon-Based Direct Electron Detectors

The EDET-80 detector being simulated in this chapter is composed of four identical quadrants (see Figure 4.5(a)). Each quadrant operates as an individual detector whose active area is covered by various insulating and conducting layers (i.e. entrance layers) of different materials and thicknesses like aluminum, silicon dioxide SiO_2, silicon nitride Si_3N_4, silicon and copper. Given that these four detector quadrants must be assembled and integrated into detector housing, in addition to the detector operating in vacuum, an appropriate mechanical design is needed for supporting the sensor, integrating the cooling system onto the mechanical housing and offering thus flexibility in adapting the detector to a TEM vacuum chamber. Moreover, the detector housing can reduce the fraction of backscattered electrons, protect the sensor from mechanical damage and allows handling the detector safely. Therefore, the construction of an advanced detector housing is of great importance here. New ideas in detector development imply the construction of a proof-of-concept device. At an early stage, we used Monte Carlo simulation to implement and test our ideas prior to the detector construction. Hence, detailed simulation studies were performed to achieve an advanced detector operating with significant improvements in imaging performance. The practical way to start simulating the detector described in section 4.6 and explore step by step the factors degrading the detector performance is to investigate the performance of various basic detector configurations as this provides useful information to further improve the detector and achieve thus the desired imaging performance.

In the first step, we calculated the signal charge (e-h pairs) generated in thin

sensitive silicon layers (i.e. silicon sensors) of 30 µm and 50 µm thickness irradiated with a 300 keV electron beam. These electrons are energetic enough to penetrate thin silicon layers as illustrated in Figure 5.2. Consequently, a large fraction of transmitted electrons is expected to return to the silicon sensor by backscattering from the supporting substrate, which increases the number of electrons producing charges in the sensor. The effect of backscattered electrons on the detector performance will be discussed later. The incident electrons interacting with the sensitive layer (i.e. 30 µm and 50 µm thick silicon layers) lose their energy via inelastic scattering, namely ionization and bremsstrahlung processes. The multiple elastic scattering of electrons leads to the beam spread which increases the amount of the charge sharing between pixels and degrades the detector imaging performance. The energy deposited by each primary electron can be converted into e-h pairs using the following equation [139]

$$N_{eh} = \frac{\Delta E}{w}. \tag{5.1}$$

Where ΔE is the energy deposition and w=3.62 eV is the energy required to create one e-h pair in silicon. The rate of the energy deposition and the subsequent mean number of e-h pairs depends on the energy of the electrons, the thickness and the atomic number Z of the sensitive layer material.

The distribution of the energy deposition of electrons passing through thin silicon layers cannot be quantified by the Bethe-Bloch formula [72, 73] because of the large statistical fluctuation of the energy loss. Instead, it can be well described by the skewed Landau distribution [76] characterized by the most probable value (mpv). Figure 5.3(a-c) shows the distributions of e-h pairs generated by 300 keV

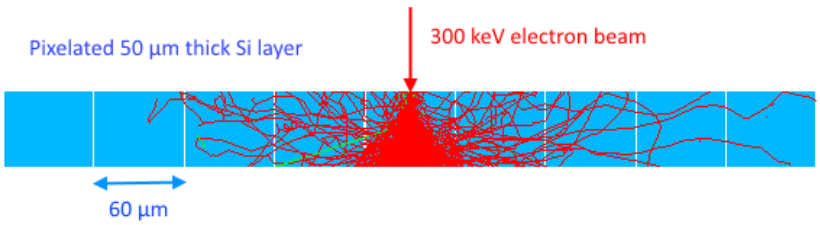

(a)

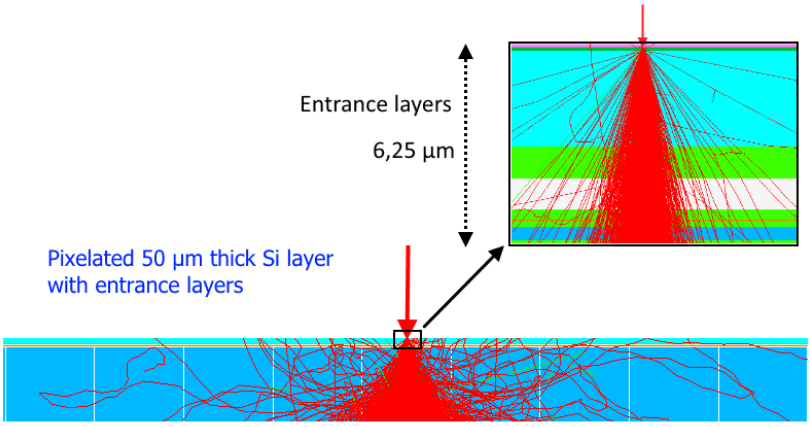

(b)

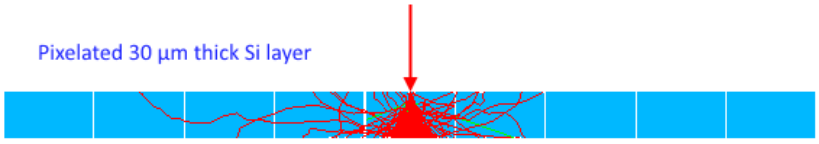

(c)

FIGURE 5.2: Simulation of the tracks of 1000 primary electrons of 300 keV in a 50 µm and a 30 µm thick silicon sensors. Due to elastic electron scattering the electron beam spreads much wider in a 50 µm thick silicon layer than in a 30 µm thick silicon layer. (a) Shows the simulated tracks of 1000 electrons of 300 keV in a 50 µm thick silicon sonsor without entrance layers. (b) Shows the simulated tracks of 1000 electrons of 300 keV in a 50 µm thick silicon sensor with entrance layers and the inset depicts the spread of the electron beam in the entrance layers. (c) Shows the simulated tracks of 1000 electrons of 300 keV in a 30 µm thick silicon sensor without entrance layers.

electrons in a 30 µm and a 50 µm thick silicon layer, as well as the Landau distribution fitted to the resulting simulation data [140]. The most probable value and the mean value of the Landau distributions are mpv=4850 e-h pairs, mv=7780 e-h pairs in a 50 µm thick silicon layer and mpv=2626 e-h pairs, mv=3995 e-h pairs in a 30 µm thick silicon layer.

The entrance layers shown in the inset of Figure 5.2(b) are in total 6.25 µm thick and decrease slightly the energy of primary electrons, which results in a slight increase in the number of e-h pairs created in the sensitive silicon layer (i.e. about 7.5% for 300 keV electrons in a 50 µm thick silicon sensor). The insets in Figure 5.3(a, b) show the energy spectra of electrons after having traversed 50 µm and 30 µm thick silicon sensors. The distributions of e-h pairs created by multiple events (multiple primary electrons) can be reconstructed from the distribution of e-h pairs created by single events (single primary electrons), as shown in Figure 5.3(c). Here the distributions of e-h pairs created by 1 to 4 events in a 50 µm thick silicon sensor are displayed. Let us assume 1000 single primary electrons (PE_1, PE_2,..., PE_{1000}) producing 1000 numbers of e-h pairs (N_1, N_2, ..., N_{1000}) which are Landau distributed. The reconstruction of the distribution of e-h created, for example, by two events is obtained by summing over all consecutive pairs of single event data set (i.e. $\mathrm{N}_1 + \mathrm{N}_2$, $\mathrm{N}_3 + \mathrm{N}_4$,..., $\mathrm{N}_{999} + \mathrm{N}_{1000}$). By repeating the same procedure we can reconstruct the distributions of multiple events. Figure 5.3(d) shows that the calculated mean and most probable values of multiple event distributions increase linearly versus the number of electrons hitting the detector.

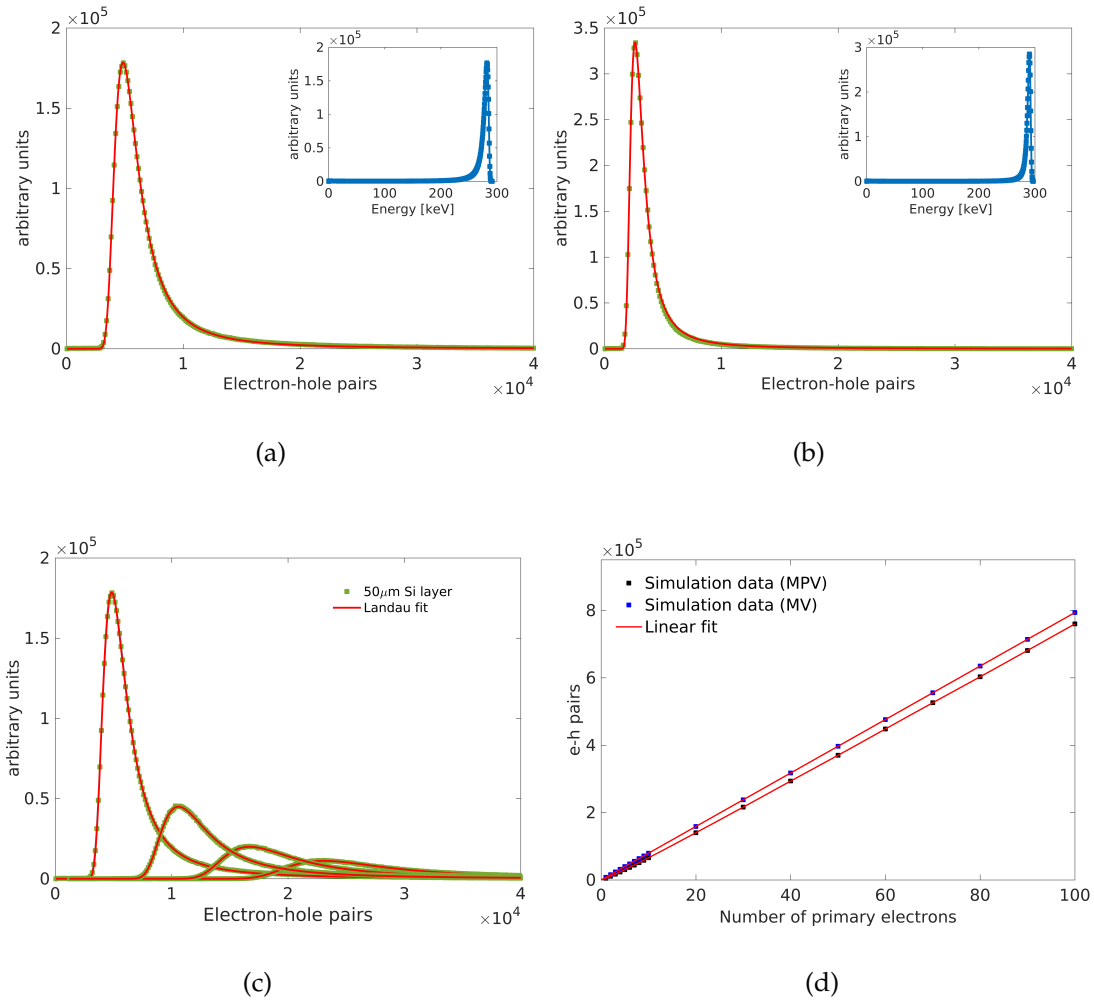

FIGURE 5.3: Distribution of e-h pairs (green squares) created by single primary electrons (single events) of 300 keV in (a) a 50 µm thick silicon layer and (b) a 30 µm thick silicon layer. The inset shows the energy spectrum of electrons after having traversed the silicon layer. (c) Example of the distributions of e-h pairs created by single and multiple events (e.g. 1 to 4 events) in a 50 µm thick silicon layer. The solid red lines in (a, b, c) are fits of a Landau distribution to the data, (d) average number and most probable vlaue of e-h pairs created in a 50 µm thick silicon layer versus the number of primary electrons hitting the silicon layer.

To validate our simulation results, we use Landau's theoretical model as described in section 2.3 to calculate the most probable values. The theoretical most probable values are in good agreement with the simulated most probable values, as

listed in Table 5.1.

TABLE 5.1: Comparison of simulated and theoretical most probable values (mpv) of charges (e-h pairs) created by 300 keV primary electrons in silicon sensors of different thicknesses.

Silicon sensor thickness [µm]	10	20	30	40	50
Theoretical most probable value	789	1690	2636	3608	4600
Simulated most probable value	837	1623	2626	3678	4850

The signal generated in a silicon detector depends on the thickness of the silicon sensor and the energy of the incident electrons, as depicted in Figure 5.4. As the material thickness increases, the energy deposition of electrons traveling through that material, and consequently the signal (e-h pairs), increases too. For instance, in 50 µm and 500 µm thick silicon layers, a primary electron of 300 keV produces on average about 7780 e-h pairs and 76500 e-h pairs, respectively. The number of e-h pairs created in a silicon sensor of given thickness decreases with increasing electron energy for the considered energy range (see Figure 5.4).

As only a given amount of charge can be collected in the internal gate of a DEPFET pixel detector, a thin sensor with excellent Detection Efficiency (DE) is needed to enhance the dynamic range of the detector by detecting only a fraction of the incident electron energy. Using DEPFET thinning technology, it is feasible to thin down the sensitive silicon layer of a DEPFET to 50 µm, which is the optimal thickness, ensuring outstanding detection efficiency (DE $\simeq$100%) and a high dynamic range of about 325 primary electrons of 300 keV per pixel. Furthermore, a thin sensitive silicon layer can minimize the contribution of multiple electron scattering to the point spread function and improves thus the spatial resolution of the

detector.

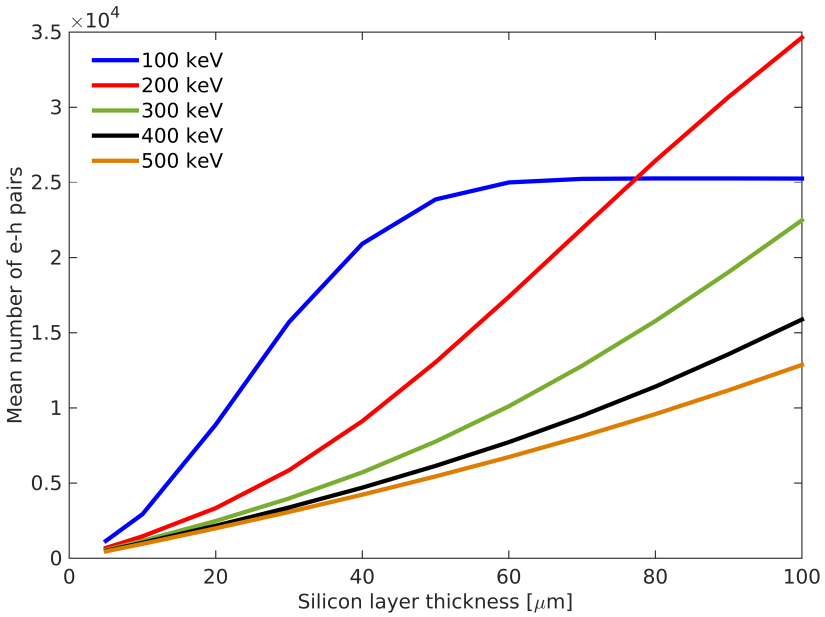

FIGURE 5.4: Mean number of e-h pairs per primary electron generated in a silicon layer of increasing thickness and for electron energies of 100, 200, 300, 400 and 500 keV.

However, 300 keV electrons have a mean travel range of about 450 µm in silicon and they will, therefore, pass through a thin silicon sensor (e.g. 50 µm thick silicon sensor) and can backscatter from the detector housing or supporting substrate into the silicon sensor. This results in an increase in the total signal generated in the sensor, as shown in Figure 5.5. This additional signal created by backscattered electrons behaves like noise, degrading the detector performance. It must consequently be reduced as much as possible. It is thus useful to calculate the fraction of the signal created by backscattered electron, as presented in the next section.

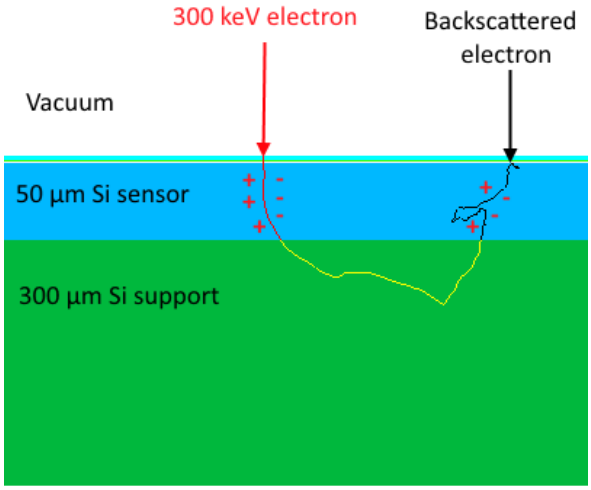

FIGURE 5.5: Simulation of the track of one primary electron of 300 keV in a silicon detector supported by 300 µm silicon support. The black trajectory represents the backscattered electron which produces additional charges in the sensor.

5.3 Impact of Backscattered Electrons on the Detector Signal

Thin sensors can easily be penetrated by energetic electrons. For instance, a 50 µm thick silicon layer irradiated with an electron beam of 300 keV, as previously shown in Figure 5.2(a), absorbs on average only about 9.4% of that energy and the transmitted electrons still have a mean energy of 270 keV (see inset in Figure 5.3(a)). Consequently, a fraction of these electrons will be scattered by the material supporting the thin sensor and can re-enter it, producing additional signal, as shown in Figure 5.6(a) and Figure 5.6(c), and degrading the detector performance [141, 142, 93, 143, 144, 145]. Figures 5.6(a) and Figure 5.6(c) also show that the electrons backscattered from an underlying support material are on average detected at some distance from the position of the impinging electron beam

as a consequence of the additional scattering events in the support material. The fraction of backscattered electrons depends on the atomic number of the material involved. It has been experimentally demonstrated that even electrons backscattered from low-atomic number materials, such as plastic supporting substrate, can significantly degrade the modulation transfer function of the detector at high spatial resolution [85]. This finding supports our simulation results depicted in Figure 5.6(c) and Figure 5.7(a), which show that supporting a sensor with low-atomic number substrates is still affecting the detector point spread function and increasing the noise in the detector.

The fraction of backscattered electrons can be reduced by thinning the supporting substrate to enable the electrons to traverse the thinned substrate with fewer scattering events. This technique is referred to as backthinning [99, 146, 142]. Figure 5.7(a) shows how the additional signal generated by backscattered electrons in the detector increases as the atomic number and thickness of the supporting substrate increase. This additional signal increases with increasing thickness until a saturation level is reached. For instance, a 150 µm thick silicon substrate is enough to reach the saturation level for incident electrons of 300 keV in a 50 µm thick silicon sensor. A similar behavior of the signal created by backscattered electrons has been observed in [147, 148]. Figure 5.7(b) shows the linear relationship between the saturated signal and the effective atomic number (for $Z \leqslant 14$) of the investigated materials.

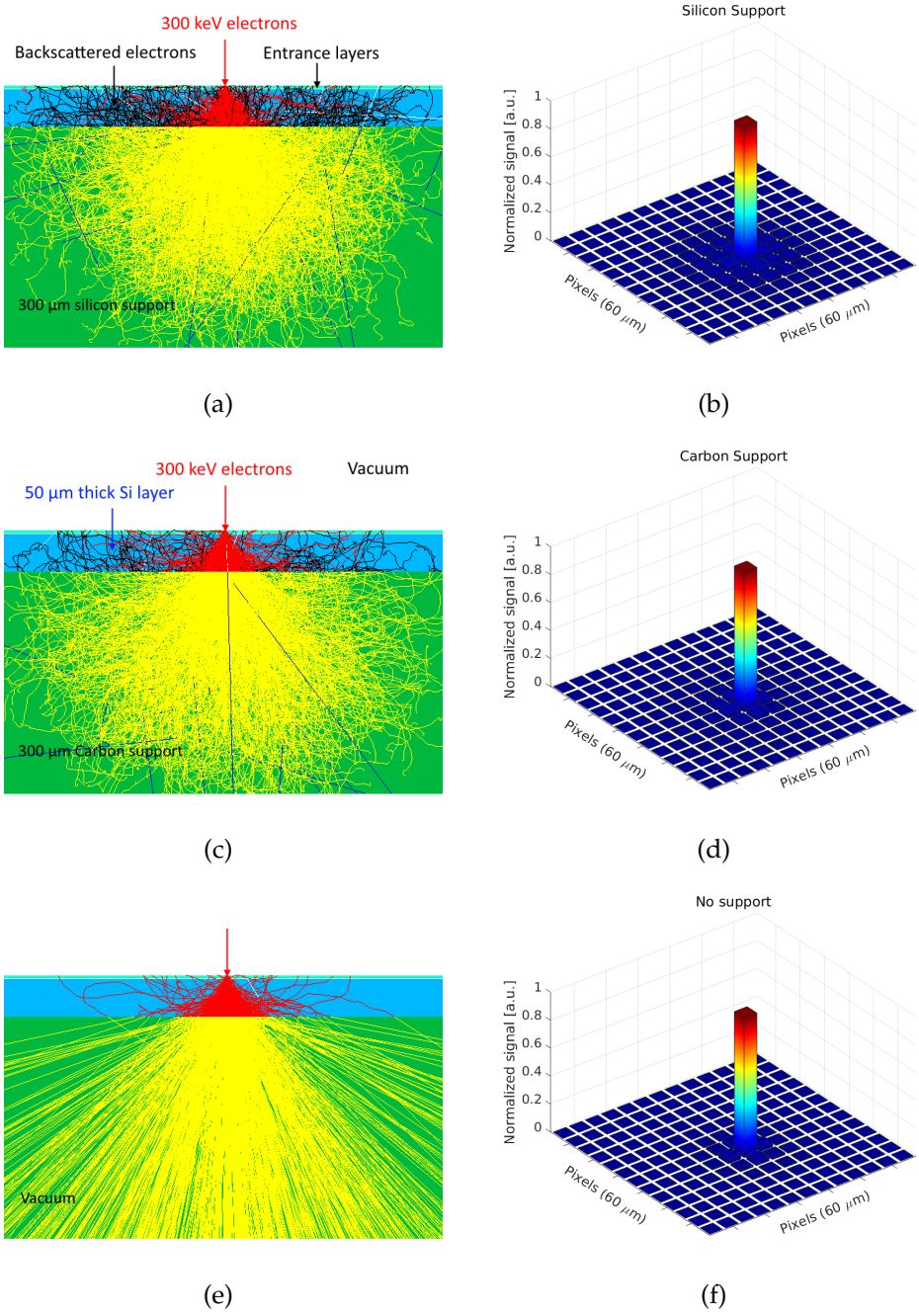

FIGURE 5.6: Simulation of the tracks of 1000 primary electrons of 300 keV in a 50 µm thick silicon sensor (blue layer) supported by two different substrates of 300 µm thickness. The corresponding PSFs are obtained from one million events and they are normalized to one. Black tracks represent electrons traveling back from the support layers into the silicon sensor. Blue trajectories represent X-rays in the support layers, white trajectories are X-rays in the sensitive layer and yellow tracks show electrons in the support layers and vacuum. (a) 50 µm thick silicon sensor supported by 300 µm thick silicon substrate, (b) corresponding PSF of (a), (c) 50 µm thick silicon sensor supported by 300 µm thick carbon substrate, (d) corresponding PSF of (c). (e) 50 µm thick silicon sensor without supporting substrate and (f) corresponding PSF of (e).

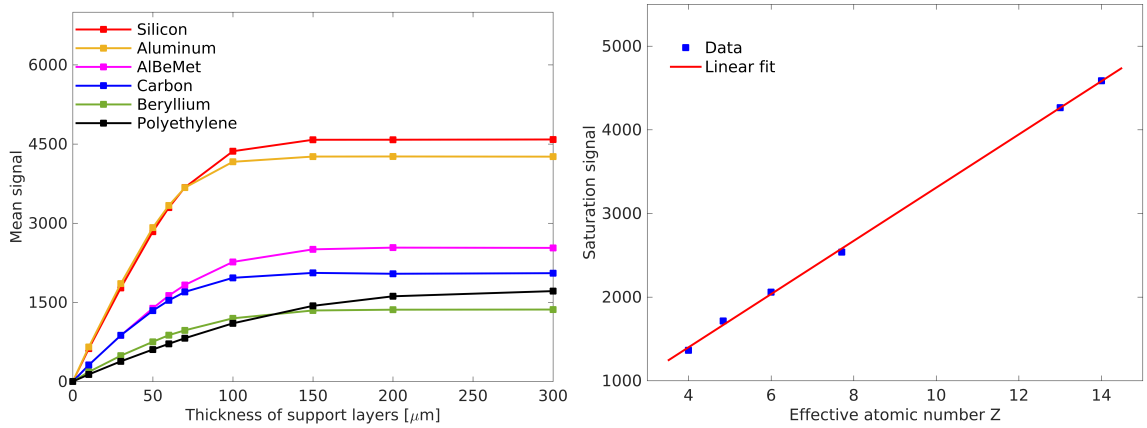

(a) (b)

FIGURE 5.7: Mean additional signal created by backscattered electrons in a 50 µm thick silicon sensor. (a) Mean signal (e-h pairs) created by backscattered electrons in a silicon sensor versus thickness of supporting substrates of different materials. (b) Saturated mean signal (e-h pairs) versus effective atomic number of supporting substrate.

5.4 Impact of Multiple Electron Scattering on the Spatial Resolution of the Detector

Spatial resolution is the ability of the detector to resolve small details in the object being imaged. It is usually expressed in terms of the modulation transfer function, which measures the ability of a detector to transfer the contrast from the object to its final image as a function of spatial frequency, describing thus the contrast transfer at a certain level of image detail. The MTF is defined as [149]

$$\mathrm{MTF} = \frac{\mathrm{M(Output)})}{\mathrm{M(Input)}}, \tag{5.2}$$

where the modulation M is given by

$$\mathrm{M} = \frac{\mathrm{Signal_{MAX}} - \mathrm{Signal_{MIN}}}{\mathrm{Signal_{MAX}} + \mathrm{Signal_{MIN}}}. \tag{5.3}$$

Figure 5.8 shows how three detectors transfer signals of various spatial frequencies from the input to the output of these detectors. The MTF can be evaluated using different techniques such as the MTF calculation from the PSF and Line Spread Function (LSF) or the Edge Spread Function (ESF) [150, 151]. The ESF, LSF and MTF were calculated in this work using the slanted edge method, which is the most appropriate approach for estimating the spatial response of imaging detectors and is thus standardized as an ISO standard, namely ISO 12233.

The slanted edge method [152, 153, 154, 155, 156, 157] is widely used to calculate the MTF because it is easily implemented and produces sufficiently accurate results. This method is realized by imaging a sharp, high contrast edge (e.g. a Tungsten or Lead edge) slightly tilted ($\sim$3 degrees) with respect to the horizontal or vertical direction of the image matrix to increase the sampling rate of the ESF. The differentiation of the oversampled ESF gives the LSF and the MTF is obtained by applying a Fourier transformation to the LSF derived from the ESF [158]. Figure 5.9 shows the setup used to image the slanted edge and Figure 5.10 describes the processing steps to obtain the ESF, LSF and finally the MTF. The edge images are processed with the aid of a software package developed by RAI Labs [159] to obtain the MTF as a function of spatial frequency.

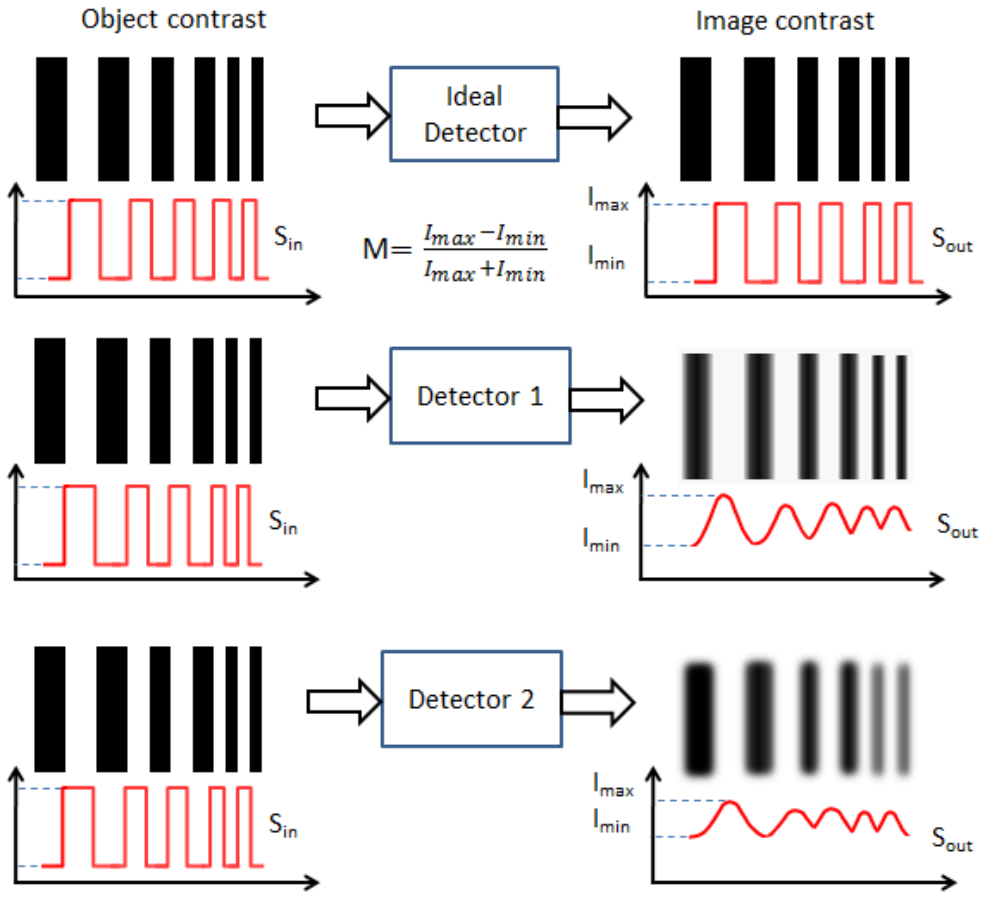

FIGURE 5.8: Examples of signal transfer at various spatial frequencies from the input to the output of three detectors. The contrast of the image recorded by the ideal detector is 100% and it is degraded in the image recorded by detector 1 and even further degraded by detector 2. That means that the MTF of the ideal detector is better than the MTFs of the two other detectors (i.e. $\mathrm{MTF}_{\mathrm{ideal}} > \mathrm{MTF}_1 > \mathrm{MTF}_2$).

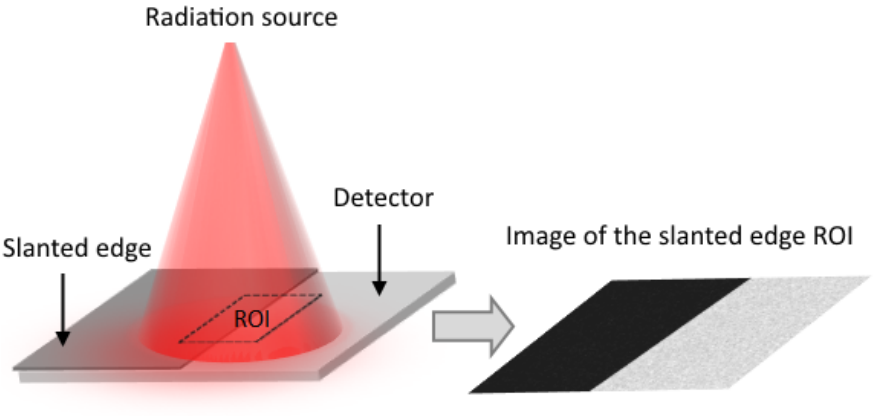

FIGURE 5.9: Schematic representation of the slanted edge method to calculate the ESF, LSF and the MTF of a detector. It is based on imaging a thin edge made up of a strong absorbing material such as tungsten. The edge is slightly rotated with respect to the x-direction or y-direction of the image matrix.

In addition to backscattered electrons, also multiple electron scattering within the sensor deteriorates the detector performance. In order to investigate the effect of multiple electron scattering on the detector MTF, the silicon sensor thickness was varied between 30 µm and 200 µm resulting thus in increased multiple electron scattering events. Figure 5.11 shows the MTFs of sensors of increasing thickness. For example, the MTF of a 30 µm thick silicon sensor surpasses the MTF of a 50 µm thick silicon sensor across all spatial frequencies. This is explained by the large spread of the electron beam in a 50 µm thick silicon sensor due to multiple scattering of electrons, which degrades the MTF. Thinning the sensor results in reduced scattering of electrons within the sensor, smaller charge spread and thus a further remarkable improvement in the MTF. However, thinner sensors also decrease the detection efficiency of the detector and subsequently the DQE. Therefore, the thickness has to be determined as a trade-off between spatial resolution and detection efficiency. In this investigation a 50 µm thick silicon sensor is the optimal senor of the

EDET-80 detector as it delivers a very good MTF, detects all primary electrons hitting the detector (∼100% detection efficiency) and provides a wide dynamic range. Furthermore, it is straightforward to thin down a silicon sensitive layer to 50 µm using DEPFET thinning technology.

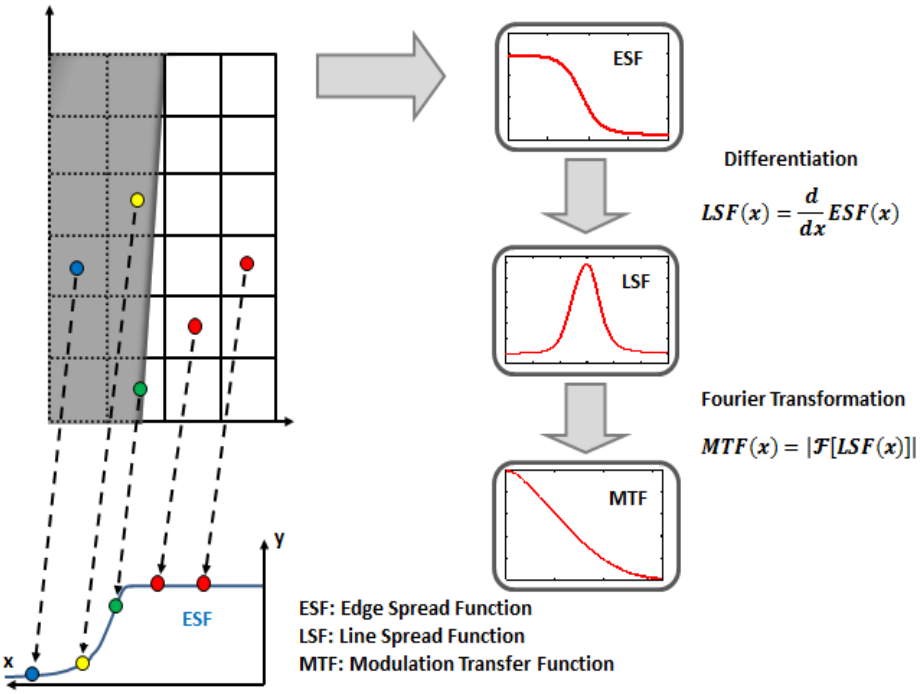

FIGURE 5.10: Analysis steps of the ROI of the slanted edge image to obtain the MTF. Pixel data are projected parallel to the edge and are accumulated in bins whose width is smaller than the detector pixel size. The projected data form the ESF, which is then differentiated to give the LSF. The MTF is obtained by a Fourier transformation of the LSF.

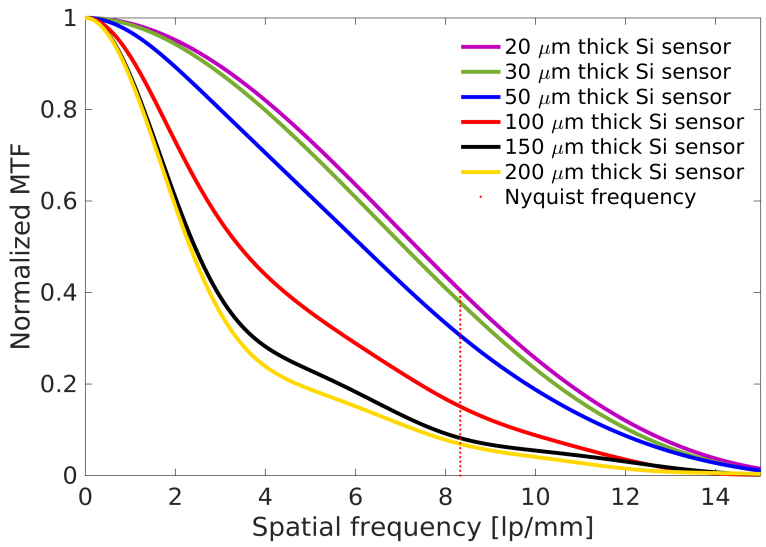

FIGURE 5.11: MTFs of silicon sensors of different thicknesses but with the same pixel area (60×60 µm^2). Thicker sensors have a poor MTF due to the large spread of the electron beam within the sensor.

5.5 Impact of Pixel Size on the Spatial Resolution of the Detector

The spatial resolution and the modulation transfer function directly depend on the pixel size of the detector. Here, the impact of pixel size on the MTF is investigated by decreasing the pixel size of a 50 µm thick silicon sensor from 60 µm to 15 µm. The smaller the pixel size, the better the spatial resolution and MTF, as demonstrated in Figure 5.12. However, the pixel size is a compromise between manufacturing feasibility, spatial resolution, SNR, readout speed and charge handling capacity. A detector with a large pixel area is preferred in some imaging applications where a high frame rate and a large charge handling capacity of the pixel are required to achieve a large dynamic range and high SNR. Despite their excellent spatial resolution, detectors with smaller pixel size show more charge sharing, have a limited charge handling capacity and a degraded SNR. In addition, the readout speed of the

detector scales with the total number of pixels. Therefore, to facilitate the data acquisition, the pixel size must be kept somewhat large. A large pixel area minimizes the total number of pixels available in the sensor and makes it easy to achieve the desired high readout speed. The pixel size of the EDET-80 detector was chosen to be 60 µm×60 µm, which is optimal to achieve the desired detector features.

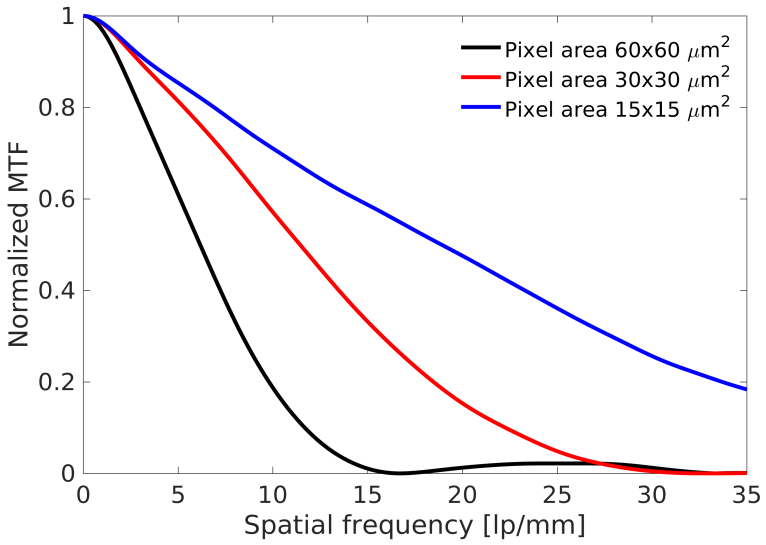

FIGURE 5.12: Effect of pixel size on the MTF in a 50 µm thick silicon sensor. The MTF is improved for smaller pixel size.

5.6 Impact of Backscattered Electrons on the Spatial Resolution of the Detector

We have already investigated the contribution of backscattered electrons to the total detected signal, as shown in Figure 5.7. Now, we explore the effect of these backscattered electrons on the spatial resolution of the detector. The signal created in a thin sensor (e.g. 50 µm thick) supported directly by a silicon substrate, as shown in Figure 5.6(a), is the sum of two signals—one is produced by the primary electrons and

the second by the backscattered electrons. It is interesting to note that, in the case of a silicon substrate of 200 µm thickness, about 58% of the total signal created in the sensor is due to backscattered electrons. Therefore, the backscattered electrons strongly degrade the MTF and make it fall off rapidly with increasing spatial frequency, in particular at low spatial frequencies, as shown in Figure 5.13. The MTF of the supported 50 µm thick silicon sensor degrades faster than the MTF of a free-standing sensor (i.e. an unsupported 50 µm thick sensor). Generally, the MTF of the supported sensor can be divided into two MTFs. The first MTF is produced directly by primary electrons hitting the detector and the second MTF is produced by the electrons being backscattered from the supporting substrate and reaching the sensor at large lateral distances.

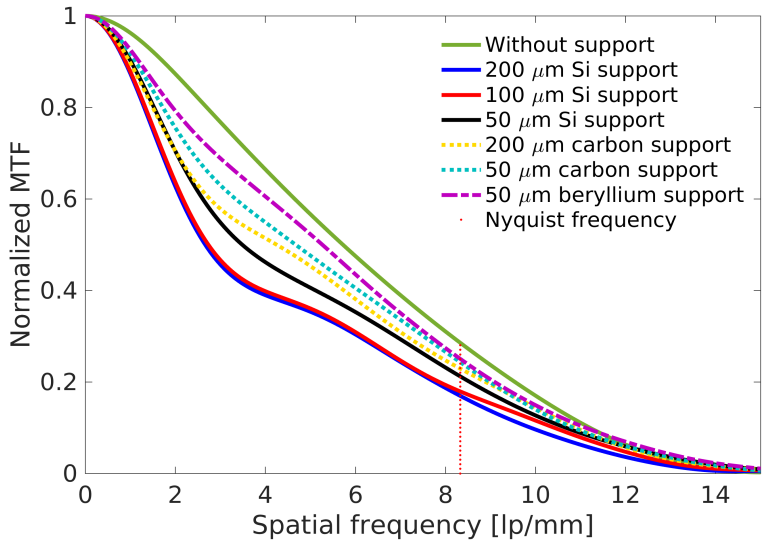

FIGURE 5.13: Impact of backscattered electrons on the MTF of various detector configurations. A free-standing silicon sensor of 50 µm thickness offers the highest MTF and when supporting this sensor with beryllium, carbon and silicon the MTF degrades depending on the thickness and the supporting material.

From these results it is clear that thinning the supporting substrate can reduce the fraction of backscattered electrons and enhance the MTF of the detector. This

MTF improvement by thinning the sensor supporting substrate is in agreement with the experimental observations reported by McMullan *et al.* [142]. However, the effect of backscattered electrons on the MTF is still significant for thinner substrates (e.g. 50 μm thick silicon support) and even for substrates made up of low-atomic number materials such as carbon or beryllium. Our studies would be much more interesting if we could minimize the contribution of the backscattered electrons degrading the detector performance. In the section that follows we will describe in greater detail an advanced detector design that can largely minimize the effect of backscattered electrons on the detector imaging performance.

Chapter 6

Design Optimization of the EDET-80 Detector

This chapter describes the simulation studies we performed to optimize the detector geometry and minimize the effect of backscattered electrons on the total detected signal. Then we investigate the capability of the optimized detector design to handle high and low electron dose. Moreover, we compare the images of tiny carbon rings captured by the optimized detector and other detectors. Finally, we discuss the effect of charge sharing between pixels. The most important findings in this chapter are the advanced detector design and the response curves of the EDET-80 detector to the primary electrons, which were calculated using an innovative approach.

6.1 Reduction of Backscattered Electrons in the EDET-80 Detector Design

To reduce the contribution of backscattered electrons to the total signal created in the sensor, a new detector design concept is needed. Detailed Monte Carlo simulation studies were performed to reduce this additional signal and investigate the

effects of different design parameters on the detector performance. One approach to minimize this undesirable signal is to prevent the backscattered electrons from reaching the sensitive area by introducing a vacuum gap between the sensitive area and the detector backplane (electron beam dump). Figure 6.1(a) and Figure 6.1(b) show two different detector geometries irradiated with a uniform-planar electron beam of 300 keV to investigate and optimize the detector housing by minimizing the fraction of backscattered electrons reaching the sensor from the backside. A vacuum gap is introduced in both detector geometries, but the walls of the detector housing illustrated in Figure 6.1(a) are straight whereas the detector housing shown in Figure 6.1(b) has slightly sloped walls.

The resulting images of the planar electron beam are shown in Figure 6.1(c) and Figure 6.1(d). Average profiles along one dimension of the sensitive area are calculated using these two detector geometries and increasing the vacuum gap between the sensitive layer and the detector backplane from 2.5 mm to 40 mm. It turns out that the backscattered electrons hitting the sensor are not uniformly distributed at small gaps (i.e. 2.5 mm, 5 mm and 10 mm) and show an almost uniform distribution at larger gaps (i.e. 15 mm and larger). The pixels in the vicinity of the walls detect the largest signals, as shown in Figure 6.1(e), due to the contribution of electrons scattered by the walls. This effect can be reduced by introducing an insensitive area between walls and sensor, as shown in Figure 6.1(f).

The optimization of the detector housing capable of reducing a significant fraction of backscattered electrons requires further investigation of the detector housing consisting of different materials. The mean signal created by backscattered electrons is calculated and plotted as a function of the gap size using different housing materials, as shown in Figure 6.2(a). From these results it is clear that a detector housing consisting of low atomic number materials (or coated with low-atomic

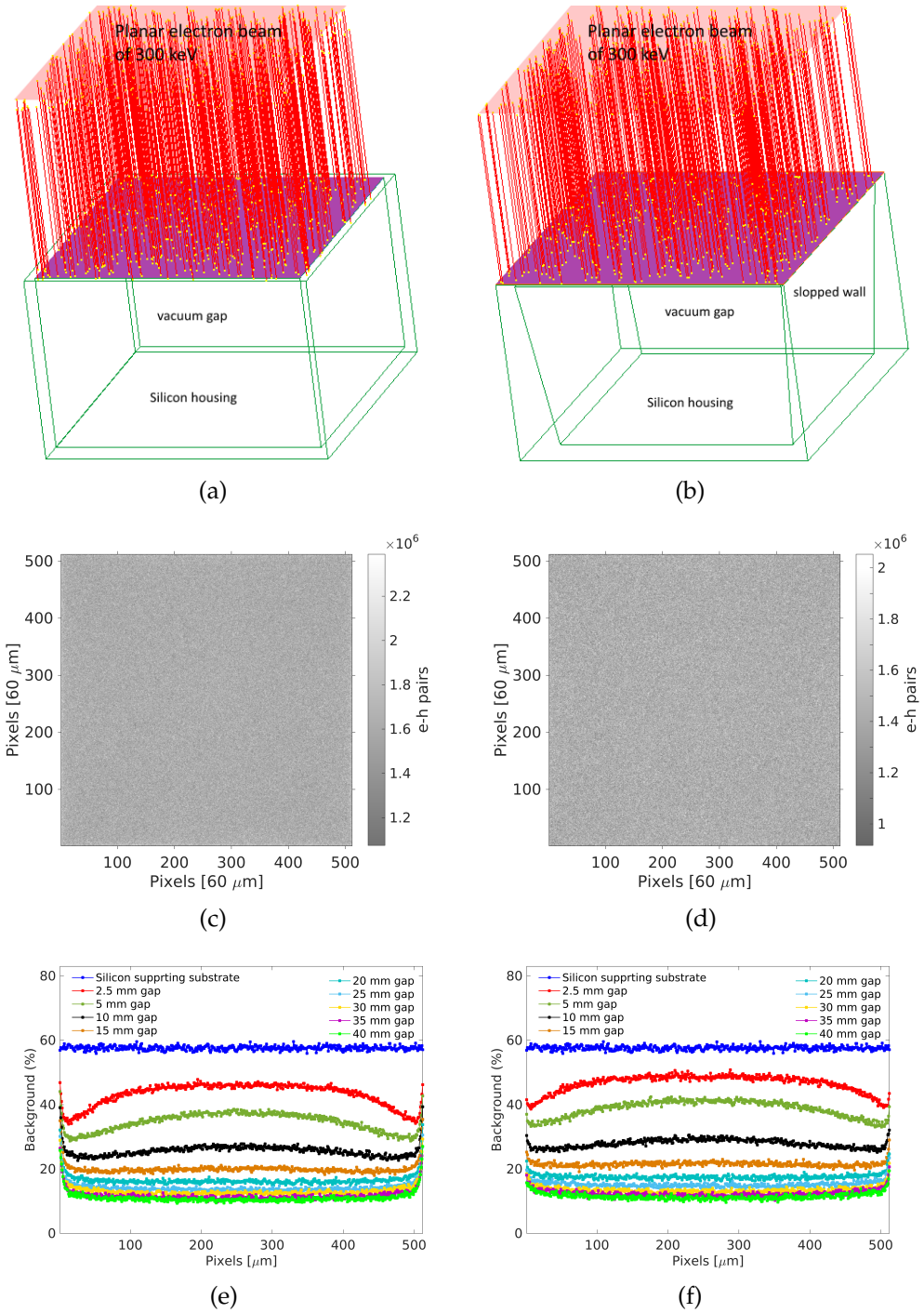

FIGURE 6.1: Two detector geometries irradiated with a planar electron beam of 300 keV to investigate the effect of a vacuum gap on the signal created by backscattered electrons. (a) Detector has a silicon housing with straight walls. (b) Detector has a silicon housing with sloped walls. (c) Resulting image of a uniform planar beam obtained with (a) using a vacuum gap of 15 mm. (d) Resulting image of a uniform planar beam obtained with (b) using a vacuum gap of 15 mm. (e) Mean profile obatined from (c) at different vacuum gaps and (f) mean profile obtained from (d) at different vacuum gaps. In (b) an additional insensitive area between sensitive area and walls has been introduced.

number materials) and including a larger vacuum gap can greatly minimize the fraction of backscattered electrons, but the space available in a TEM should be considered when optimizing the size of the vacuum gap. Thus, 35 mm was chosen as an optimized vacuum gap of our detector housing. Figure 6.2(b) shows that the fraction of backscattered electrons increases as the thickness of the sloped walls at the backplane of the detector housing becomes thicker. In other words, there is a proportional relationship between the signal generated by backscattered electrons in the sensor and the slope of the walls of the detector housing. In a next step, another advanced detector geometry was simulated in which the detector housing has both sloped and straight walls resulting in a robust and flexible detector housing. The cross-sectional view of this advanced detector design is shown in Figure 6.3(a). This detector housing is made up of silicon coated with carbon, has a vacuum gap, sloped walls, an additional vacuum cavity and insensitive areas between the walls and the first sensitive pixels of the sensor. These insensitive areas have the advantage of reducing the fraction of electrons scattered from the walls and hitting the pixels in the vicinity of the walls, thus avoiding the fast saturation of these pixels. Figure 6.3(b) shows a cross-sectional view of the whole detector system without carbon coating, which was constructed based on the simulation studies presented in this thesis.

The approach presented here to solve the problem of noise produced by backscattered electrons demonstrates that it is possible to minimize the unwanted signal created by backscattered electrons by choosing a convenient detector housing material, an optimized vacuum gap and an appropriate bottom thickness of the sloped walls. Further improvement can be achieved using low-atomic number materials to construct the detector housing or by coating the detector housing, made up of relatively high-atomic number materials, with low-atomic number materials. The

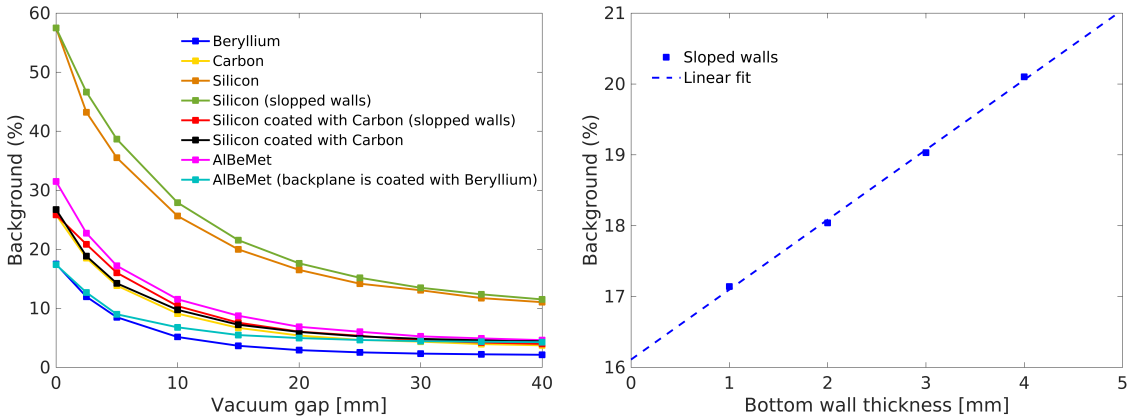

(a) (b)

FIGURE 6.2: Additional signal due to backscattered electrons as a function of the vacuum gap, material of the detector housing and the bottom thickness of sloped walls. (a) Comparison between coated and uncoated detector housings made up of different materials. (b) Background as a function of bottom thickness of sloped walls using a silicon housing with 20 mm vacuum gap.

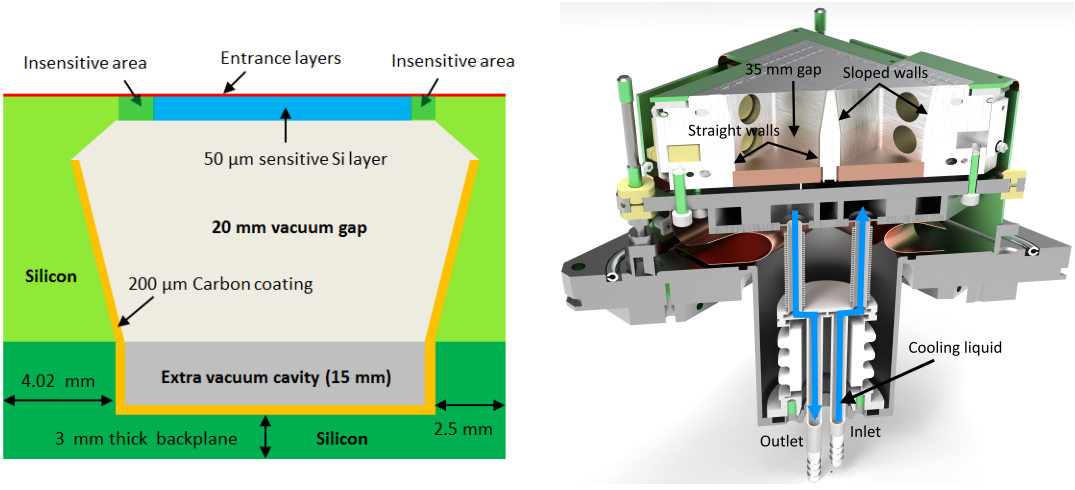

(a) (b)

FIGURE 6.3: Cross-sectional views of the EDET-80 detector design. (a) Cross-sectional view of one quadrant of the detector. The dimensions shown in (a) are not to scale. (b) Cross-sectional view of the complete detector geometry constructed based on the simulation studies.

results presented in Figure 6.2(a) show that a silicon housing including a vacuum gap of 25 mm and straight walls reduces the additional signal created by backscattered electrons from about 58% to 14% and it can be further reduced to 5% if the silicon housing is coated with carbon, which is similar to the results obtained from a carbon housing.

The detector design shown in Figure 6.4(a) will be further investigated, keeping the optimized vacuum gap at 35 mm and changing the material of the detector housing and the energy of primary electrons. Using this detector housing design, it is straightforward to coat the additional cavity or construct it completely from materials composed of low-atomic number elements such as carbon or beryllium. Figure 6.4(b) shows the resulting mean signal per pixel for different detector housing materials with 35 mm vacuum gap. It should be noted here that the lower the energy of primary electrons, the smaller the fraction of backscattered electrons from the detector housing. This means that 200 keV electrons produce less background signal than 300 keV electrons.

Introducing some further modifications in this innovative detector housing such as making the backplane design similar to that of the walls of an anechoic chamber or introducing holes in the walls of the detector housing do not further improve significantly the detector performance. The detector design described earlier is expected to achieve the desired imaging performance.

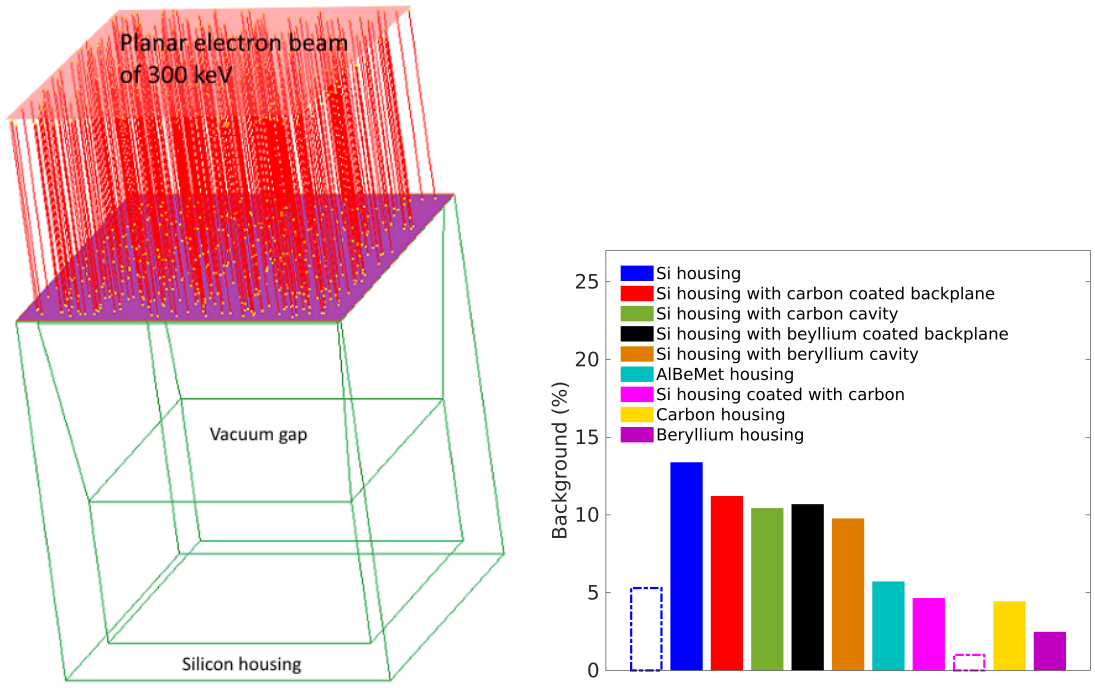

(a) (b)

FIGURE 6.4: (a) EDET-80 detector design combining both sloped walls and an additional cavity with straight walls and (b) mean signal per pixel produced by backscattered electrons using different detector housing materials at a vacuum gap of 35 mm. Filled bars and empty bars represent data for 300 keV and 200 keV primary electrons, respectively. Same colors label the same detector geometry.

6.2 Achievable Dynamic Range and Single Electron Resolution of the EDET-80 Detector

The shape of the DEPFET response and the number of bits of the Analogue-to-Digital Converter (ADC) are the key factors determining the achievable dynamic range and single electron resolution of the EDET-80 detector. The EDET-80 detector can handle a large amount of charges created in a given pixel by implementing an 8-bit Drain Current Digitizer (DCD), which is an ADC, and making use of a

DEPFET sensor with signal compression at the sensor level [55] to improve the dynamic range. As described in section 4.5, a DEPFET with a non-linear characteristic response curve provides the required technology to cope with both single electron resolution and large dynamic range. Figure 6.5(a) shows the shape of the simulated response of the EDET-80 detector based on a DEPFET sensor with signal compression at the sensor level. We can obviously distinguish two different regions, namely a linear and a non-linear region. At low dynamic range, i.e. small signals (<10^5 e-h pairs, < 10.8 primary electrons of 300 keV), the DEPFET response curve is linear as shown in Figure 6.5(b), which results in a linear amplification of the signal with a gain, defined as $g_q = \mathrm{d}I/\mathrm{d}Q$, of about $g_q = 2.1064 \times 10^{-4}$ µA/electron. After that, the gain starts decreasing and reaches at $3{\times}10^6$ electrons a value of about g_q =3.7133$\times10^{-5}$ µA/electron, resulting in the desired non-linear amplification. This enables the EDET-80 detector to integrate up to three million electrons per pixel (i.e. 325 primary electrons of 300 keV). Consequently, both single electron resolution and large dynamic range can be achieved. A primary electron of 300 keV generates on average a charge of about 9250 electrons in the EDET-80 setup illustrated in Figure 6.4(a) and produces a current I =1.948 µA. The 8-bit DCD of the EDET-80 detector can digitize a maximal current of 32 µA, resulting in $32/2^8$ =0.125 µA per least significant bit (0.125 µA/LSB), which corresponds to 594 electrons. Table 6.1 summaries the number of electrons per DCD bin at different gain settings of the DCD. These gain settings k of the DCD serve as an amplifier.

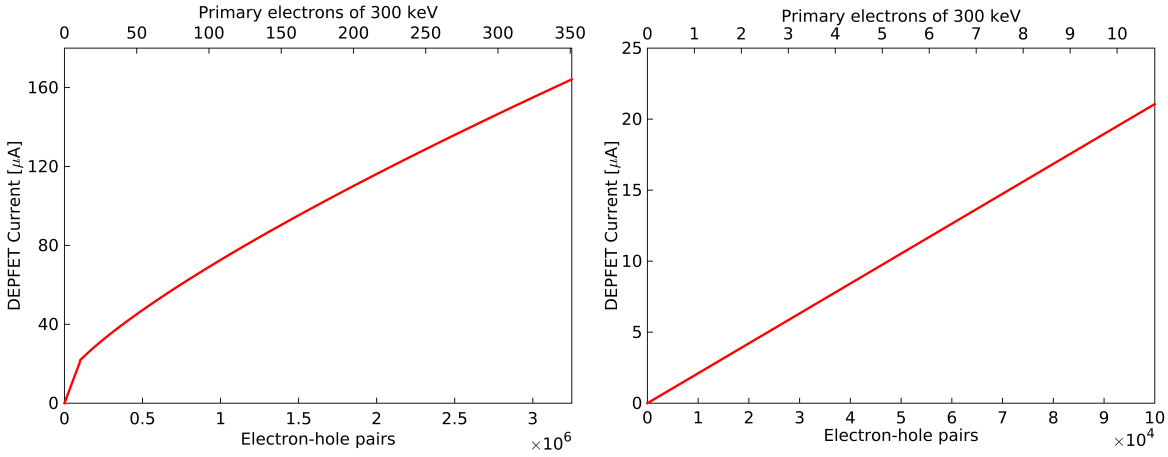

(a) (b)

FIGURE 6.5: EDET-80 response in terms of current as a function of charge created by primary electrons in a DEPFET pixel. (a) Shows the simulated non-linear response of the DEPFET sensor used in EDET-80 as a function of charge and primary electrons after pedestal subtraction. Please note that there are two different regions, a linear and non-linear region. (b) Shows a zoom of the linear region of (a).

TABLE 6.1: Number of electrons per Least Significant Bit (LSB) at different gain settings of the DCD. High gain settings (k=2, k=1 and k=0.667) are well suited for single electron resolution and small gain settings ($k \leqslant$0.2) are useful for high dynamic range.

Gain k	2	1	0.667	0.2	0.182	0.167	0.154	0.1
Charge per LSB	297	594	890	2970	3264	3557	3857	5940

To investigate the ability of our detector to cover both a wide dynamic range and resolve single electron hits, simulations were performed and the simulated signal generated in the detector was processed passing through all the signal processing stages in the detector to finally obtain the digitized signal at the output. A DCD with an 8-bit resolution and 50 nA noise is used to digitize the current providing thus 256 grayscale levels (i.e. 0: black and 255: white). This investigation was performed through several steps that are illustrated in Figure 6.6 and Figure 6.7. For the sake

of clarity, we do not show the results obtained from all events. Otherwise, the plots would appear extremely crowded.

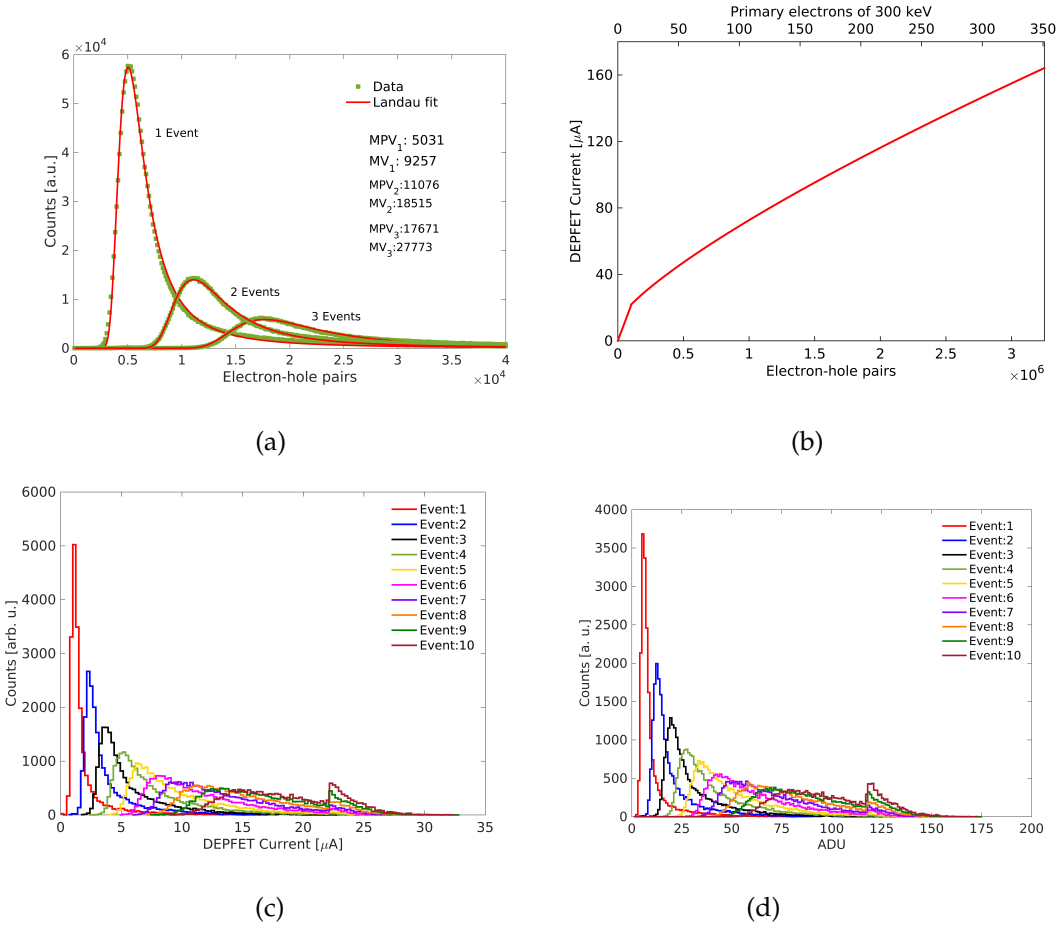

(a) (b)

(c) (d)

FIGURE 6.6: Processing of the signal created in the EDET-80 by 300 keV primary electrons. (a) Example of three e-h pair distributions created in the EDET-80 by single electron events, two electron events and three electron events of 300 keV. (b) Non-linear DEPFET response curve used to convert e-h pairs into current being digitized. (c) Example of ten DEPFET current distributions generated by primary electrons in the EDET-80. (d) Digitization of (c) using a DCD gain setting of k=0.667.

In the first step, we calculated the distributions of e-h pairs created by primary electrons of 300 keV in the sensor (Figure 6.6(a)). The sensor recording the signal is not pixelated and thus the effect of charge sharing between pixels is excluded. In the second step, we evaluated the DEPFET current produced by e-h pairs using the

relationship shown in Figure 6.6(b), which shows the DEPFET current (i.e. drain current) in a pixel as a function of charges (i.e. e-h pairs). As a result, we obtained the DEPFET current distributions generated by primary electrons, as depicted in Figure 6.6(c). In the third step, the resulting current distributions are digitized by a DCD with an 8-bit resolution for each gain setting. The resulting signal distributions are in digital units and shown in Figure 6.6(d) for a gain setting of k=0.667. It is worth noting that the distributions of 6 to 10 events depicted in Figure 6.6(c) and Figure 6.6(d) show an edge at 22.16 µA and ADU=119 , respectively, due to the kink appearing at $\sim 10^5$ e-h pairs in the plot of the DEPFET response shown in Figure 6.6(b). This kink represents the transition point between the linear DEPFET response and the non-linear DEPFET response. The last step is of particular importance as it describes our novel approach to investigate the detector response in terms of primary electrons and delivers plots that can be used to determine the number of detected electrons from the recorded digital signal. In this approach the distributions of digitized signals presented in Figure 6.6(d) are necessary to calculate the mean number of primary electrons as a function of ADUs taking into account all the overlaps between ADU distributions, meaning that a given ADU can be produced from several events with different weights. This can be mathematically expressed as follows

$$\overline{PE}(i) = \frac{\sum_{j}^{n} PE_j^i \times C_j^i}{\sum_{j}^{n} C_j^i}. \tag{6.1}$$

Here $\overline{PE}$ denotes the mean number of primary electrons detected at an ADU=i, PE_j^i is the number j of primary electrons occuring C_j^i times at an ADU=i. Let us take as an example the case of ADU=50 to understand how we calculated $\overline{PE}$ as a

function of ADUs. The value ADU=50 can be created by 1 to 10 primary electrons of 300 keV, as shown in Figure 6.6(d), but with different weights that are summarized in Table 6.2.

TABLE 6.2: Number of primary electrons PE producing an ADU=50 with different weights in the detector operating with a DCD gain setting of k=0.667.

ADU=50										
Event (PE)	1	2	3	4	5	6	7	8	9	10
Counts	15	62	116	221	355	469	446	217	44	1

Inserting these values in equation 6.1 gives $\overline{PE}(50)\simeq$5.76 primary electrons. This describes that a signal of ADU=50 is produced by $\sim$5.76 primary electrons when operating the detector with a DCD gain setting of k=0.667.

This approach may raise concerns about the effect of charge sharing between pixels which certainly affects the value of $\overline{PE}$. To consider this effect, we calculated the distributions of ADUs created by primary electrons and charge sharing. The events (i.e. primary electrons + charge sharing) are now termed "event fraction". Figure 6.7(b) illustrates 9 additional distributions of the event fractions between event 1 and event 2. An event fraction 1.1 means that there is 10% contribution of charge sharing in the total detected signal. Consequently, the new value of $\overline{PE}$ is now $\sim$5 instead of $\sim$5.76. The same procedure has been used for each ADU and each DCD gain setting to finally obtain the relationship of primary electrons as a function of ADUs, as shown in Figure 6.7(c). Please note that the plots in Figure 6.7(c) are calculated taking into account all possible events including event fractions (i.e. up to 3000 events) and all DCD gain settings (i.e. 8 DCD gain settings), thus leading to 3000$\times$8 distributions of digitized signals.

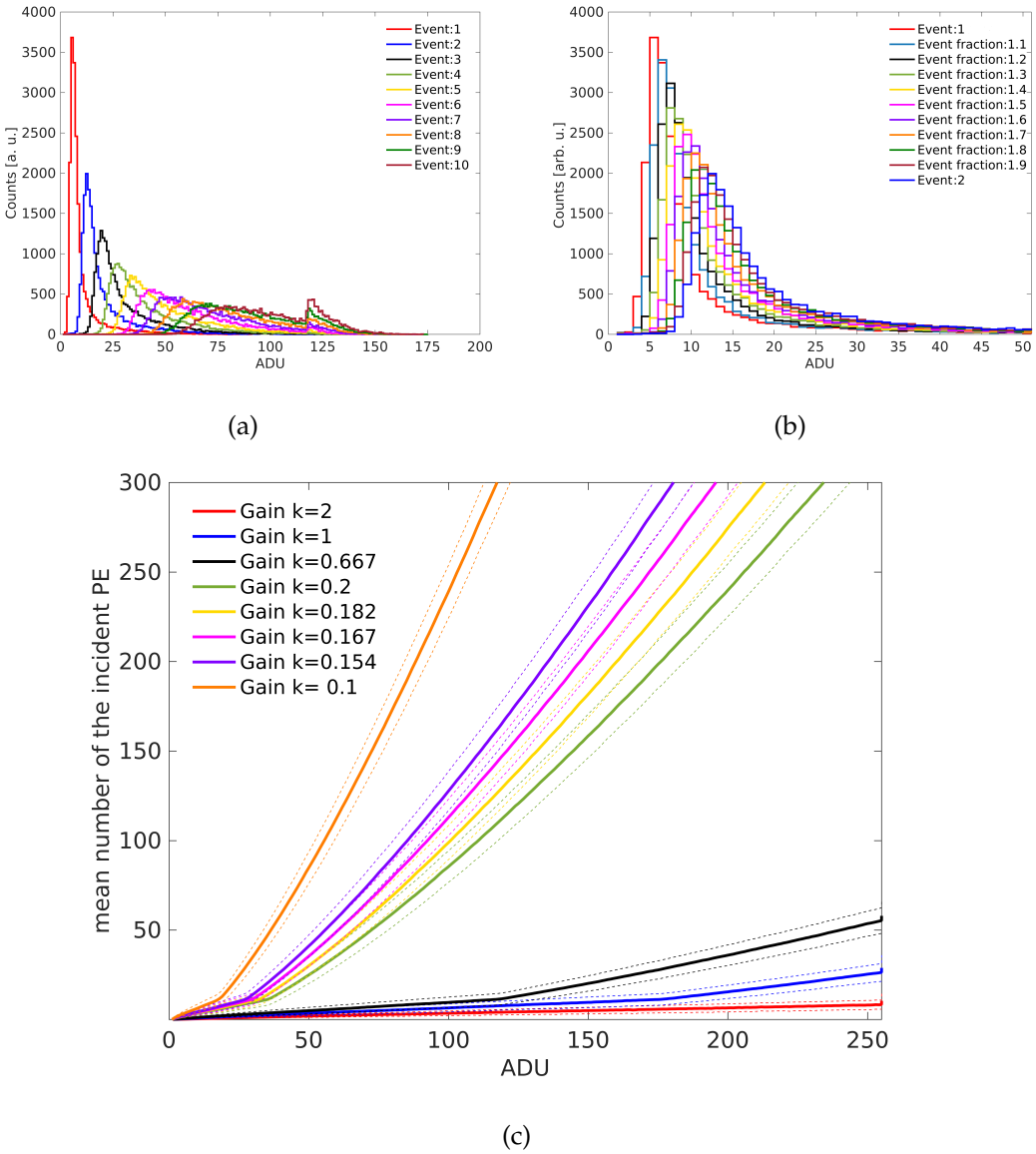

FIGURE 6.7: Processing of the signal created in the EDET-80 by 300 keV primary electrons. (a) Distribution of digitized signals using a DCD gain setting of k=0.667. The distributions are created by 1 to 10 events. (b) Example of distributions created by a fraction of events. (c) EDET-80 response curves. Dashed thin lines represent the standard deviation for the solid lines of the same colors.

These response curves of the EDET-80 detector are of crucial importance as they allow us to determine from a given detected signal in ADU the mean number of

primary electrons that interacted with the detector to generate this signal. Furthermore, they demonstrate that our EDET-80 detector can detect single electrons and handle a wide dynamic range using an appropriate DCD gain setting. For instance, high DCD gain settings such as k=2, k=1 and k=0.667 are suitable for imaging applications requiring low electron dose (single electron detection). Other gain settings (i.e. $k \leqslant 0.2$) can preserve the range up to 300 primary electrons and they are thus suitable for high-electron dose applications and, hence, high dynamics range. In addition, we will see later in this thesis the applicability of the results shown in Figure 6.7(c) in estimating the imaging performance of the EDET-80 detector.

The same calculations were performed to obtain the response curves of a free standing silicon sensor. The resulting curves shown in Figure 6.8 are close to the result obtained for the optimal detector geometry shown in Figure 6.7(c).

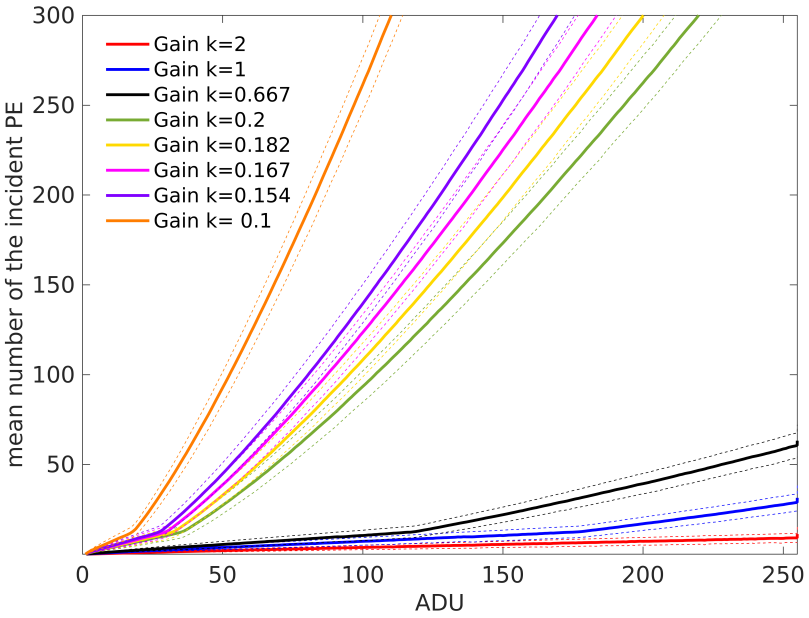

FIGURE 6.8: Response curves of a free standing silicon sensor irradiated with 300 keV electrons. Dashed thin lines represent the standard deviation for the solid lines of the same colors.

It is interesting to investigate the response curves of the EDET-80 detector irradiated with 200 keV electrons. The EDET-80 setup shown in Figure 6.4(a) was used and the previously described calculations were performed to obtain the EDET-80 response curves. The obtained results are shown in Figure 6.9. It should be noted that one primary electron of 200 keV generates on average about 15470 e-h in the EDET-80 detector shown in Figure 6.4(a). This large amount of charge enhances the signal but limits the dynamic range of the detector. Also, it may restrict its capability to resolve single hits as 200 keV electrons undergo more scattering events than 300 keV electrons. Therefore, a significant increase in the charge sharing between pixels can be observed, as we will see at the end of this chapter.

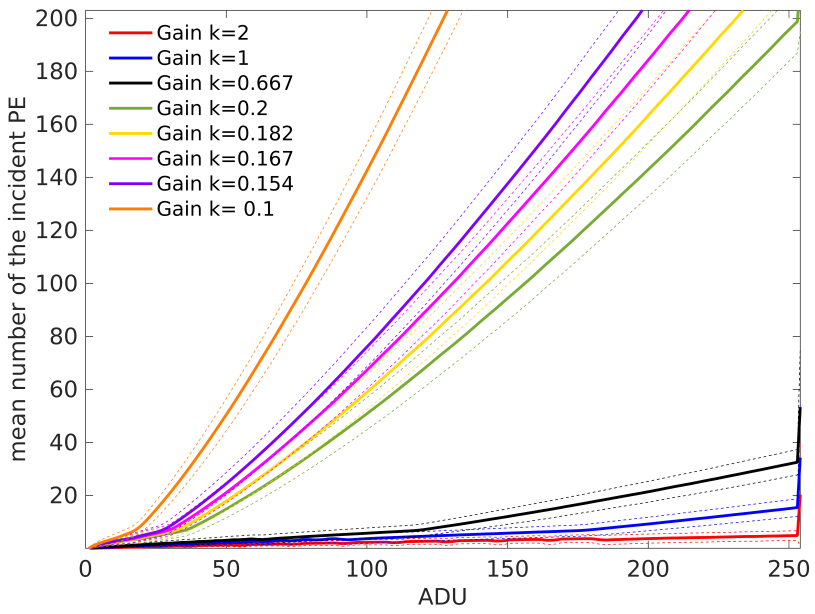

FIGURE 6.9: Response curves of the EDET-80 irradiated with 200 keV electrons. Dashed thin lines represent the standard deviation for the solid lines of the same colors.

6.3 Carbon Ring Imaging with the EDET-80 Detector

To investigate the imaging performance of the EDET-80 detector and compare it to the performance of other detector designs, tiny carbon rings were imaged using the simulation setup illustrated in Figure 6.10.

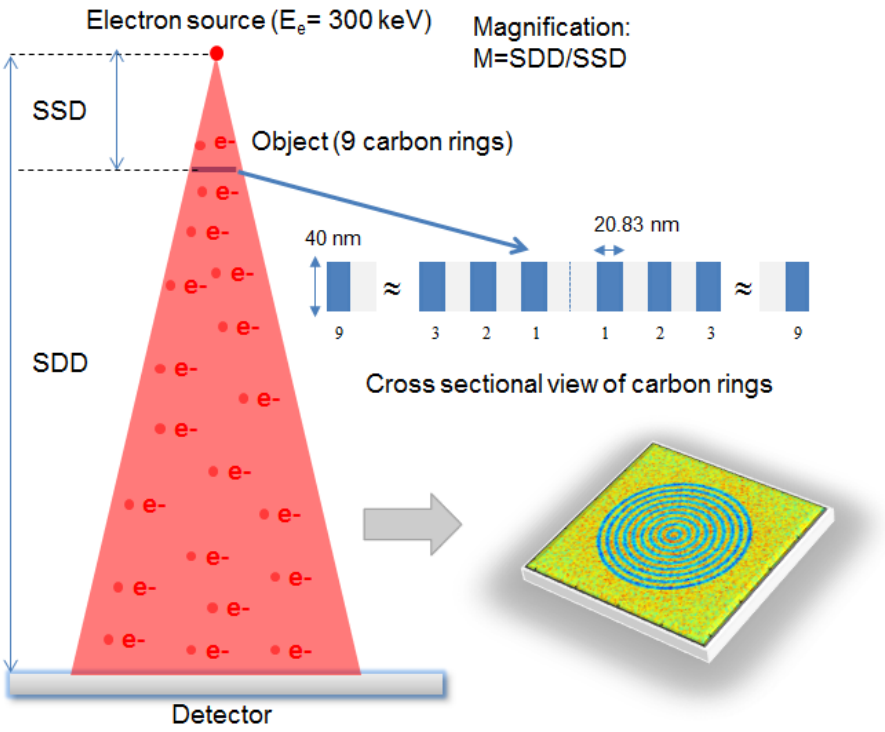

FIGURE 6.10: Schematic illustration of the simulation setup used to investigate the imaging performance of the EDET-80 detector. Carbon rings are represented by hollow cylinders, SSD stands for the distance between the electron source and the sample. SDD stands for the distance between the electron source and the detector.

The carbon rings being imaged are irradiated with a cone-shaped electron beam of 300 keV, producing an average flux of 225 electrons per pixel at the detector. The obtained images are magnified by a factor of M=12,000 onto the detector. The

magnification can be determined by changing the electron Source-to-Sample Distance (SSD) and the electron Source-to-Detector Distance (SDD). Figure 6.11 shows images of these carbon rings after digitization using a low DCD gain setting (i.e. k=0.1) which is suitable for a large dynamic range (e.g. 225 primary electrons per pixel), as well as the corresponding radial profiles of the signal intensity in each digitized image. The design of the detector housing is of crucial importance and can dramatically affect the imaging capability of the detector as previously discussed. From these results, it is clear that supporting a sensor with a silicon substrate significantly increases the contribution of backscattered electrons to the total signal, thus decreasing the imaging performance of the detector. It is interesting to note that the final detector geometry including a 35 mm vacuum gap and carbon-coated housing acts close to a free-standing sensor (i.e. a sensor without supporting substrate).

To compare the integrated radial profiles shown in Figure 6.11 and Figure 6.12(a), we calculated the mean of the relative difference between local maxima and local minima of the peaks appearing in the integrated radial profiles. Then, we normalized it to the mean of the relative difference between local maxima and local minima obtained from the free-standing detector geometry (i.e. setup 1). The obtained results are shown in Figure 6.12(b).

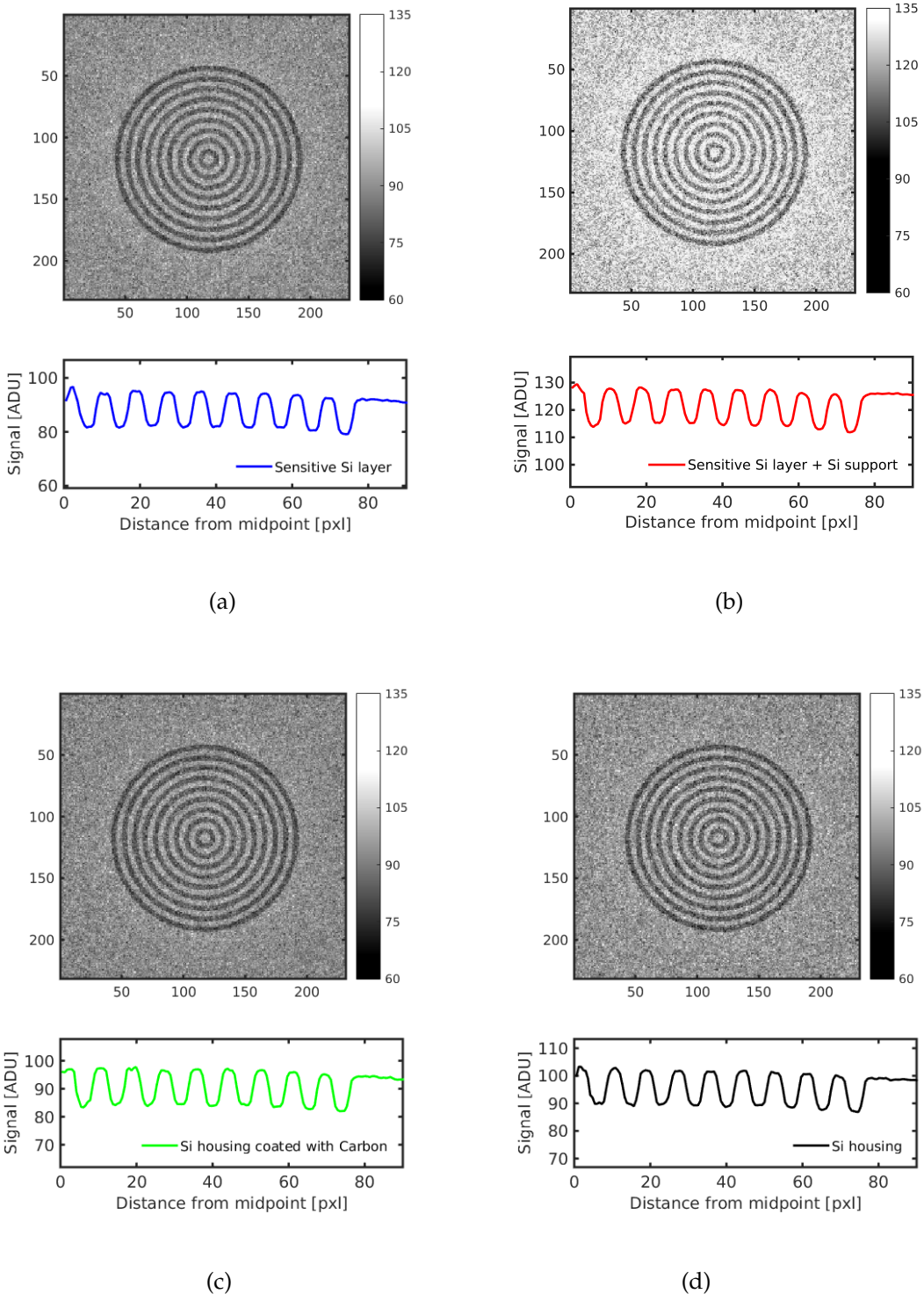

FIGURE 6.11: Digitized images of carbon rings and the resulting radial profiles obtained with four different detector geometries using a DCD gain setting of $k = 0.1$. (a) 50 µm thick silicon sensor (free standing sensor), (b) 50 µm thick silicon sensor supported by a 300 µm thick silicon support, (c) silicon housing coated with 200 µm thick carbon layer and (d) silicon housing.

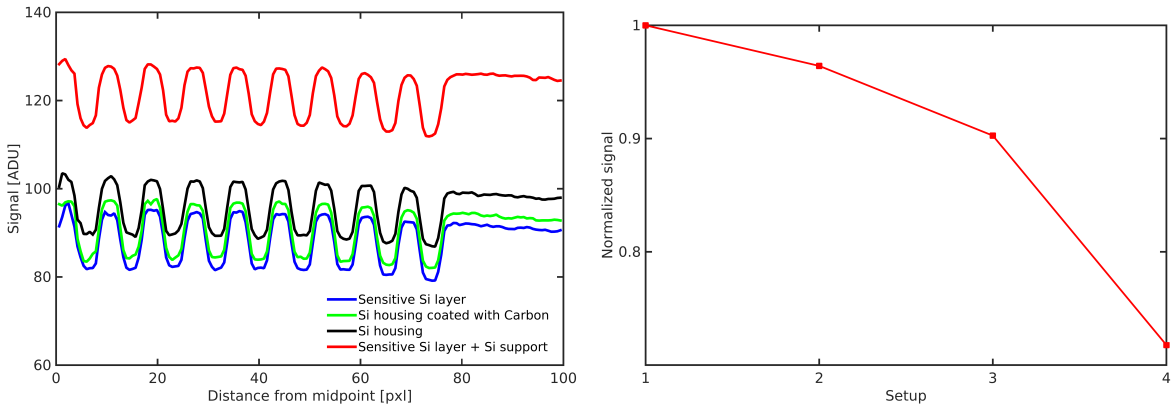

(a) (b)

FIGURE 6.12: Imaging performance of four detector configurations. (a) Digitized radial profiles. (b) Normalized signal obtained from four detector configurations. Setup number 1: 50 µm thick silicon sensor (i.e. free standing sensor), setup number 2: silicon housing coated with carbon, setup number 3: silicon housing and setup number 4: 50 µm thick sensitive silicon layer supported with a 300 µm thick silicon support.

6.4 Charge Sharing Between Pixels of the EDET-80 Detector

Direct electron detectors suffer from the effect of charge sharing between neighboring pixels. This occurs when the charge generated by a primary electron is detected in more than one pixel, leading to a degradation of the detector performance [160, 161, 162]. This effect is caused by different physical processes such as the lateral spread of the electron beam due to the scattering of electrons by sensor atoms. The electrons can thus deviate from their original trajectory and reach adjacent pixels provided that these electrons have sufficient kinetic energy to traverse several pixels. Consequently, charges are also generated in the neighboring pixels. For example, electrons of 300 keV have a mean absorption length of about 450 µm

in silicon. This is usually larger than a typical pixel size, resulting in a charge sharing. The effect of charge sharing becomes a serious issue for a smaller pixel area, a larger pixel thickness and when the electrons hit the sensor in the vicinity of the pixel border [163]. The study of the effect of charge sharing can therefore provide helpful information to design a convenient pixel detector.

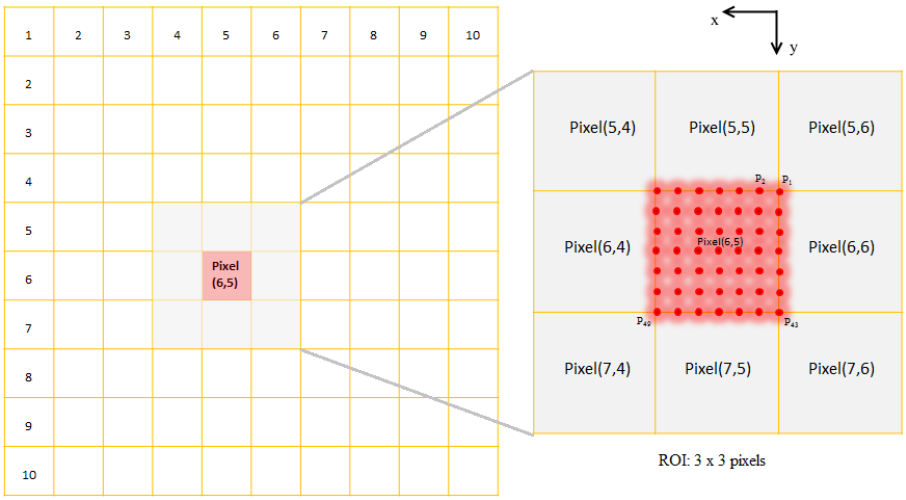

FIGURE 6.13: Schematic illustration of the simulation setup used to study the effect of charge sharing between one center pixel and its neighboring pixels. The center pixel (6,5) is irradiated with a pencil electron beam of 300 keV at different positions. 49 impact positions in pixel (6,5) are simulated starting from P_1(x_1=0, y_1=0) and ending at P_{49}(x_{49}=60 µm, y_{49}=60 µm).

In the simulation study of the effect of charge sharing, we chose a matrix of 10 by 10 pixels to investigate the charge sharing between pixels of 60×60 µm^2. A region of interest (ROI) consisting of 3×3 pixels is shown in Figure 6.13 (right) and the charge sharing is investigated as a function of the position of the impact point of the electron beam. The center pixel (5,6) is irradiated with an electron beam of 300 keV at different positions starting from the upper right corner of the pixel (5,6) corresponding to position P_1 (x_1=0, y_1=0). Then, the impinging electron beam is shifted

7 times in 10 µm steps to the left and 7 times in 10 µm steps to the bottom leading to 7 line scans of 7 positions each, resulting thus in 7×7 = 49 positions, which are highlighted by red spots in the pixel (5,6) as shown in Figure 6.13 (right). For each of the 49 impact positions, we calculated the fraction of signal created in each pixel. The results obtained from this investigation indicate that the mean fraction of the charge in the center pixel obtained from all the impact positions is about 56%. Figure 6.14 shows the fraction of charge shared between pixels at five different impact positions and the resulting mean charge obtained from all the impact positions. Also, the results show that the amount of charge sharing depends on the position of the impinging electron beam, and the closer the beam to the pixel edge, the larger the fraction of charge sharing. In this study, the mean fraction of the charge distributed among pixels is the point spread function of the detector.

In this approach, there are many impact positions (i.e. 24 positions) at the edge of the center pixel. That means that the charge sharing may be overestimated. Therefore, the center pixel is irradiated with one million electrons, hitting it at random impact positions. The obtained results are shown in Figure 6.15 for 300 keV and 200 keV electrons. The fraction of charge recorded in the center pixel is 67% for 300 keV electrons instead of 56%, decreasing to 48% for 200 keV electrons because low energy electrons undergo more elastic scattering than high energy electrons.

The next chapter describes quantitatively the imaging performance of the EDET-80 detector in more detail.

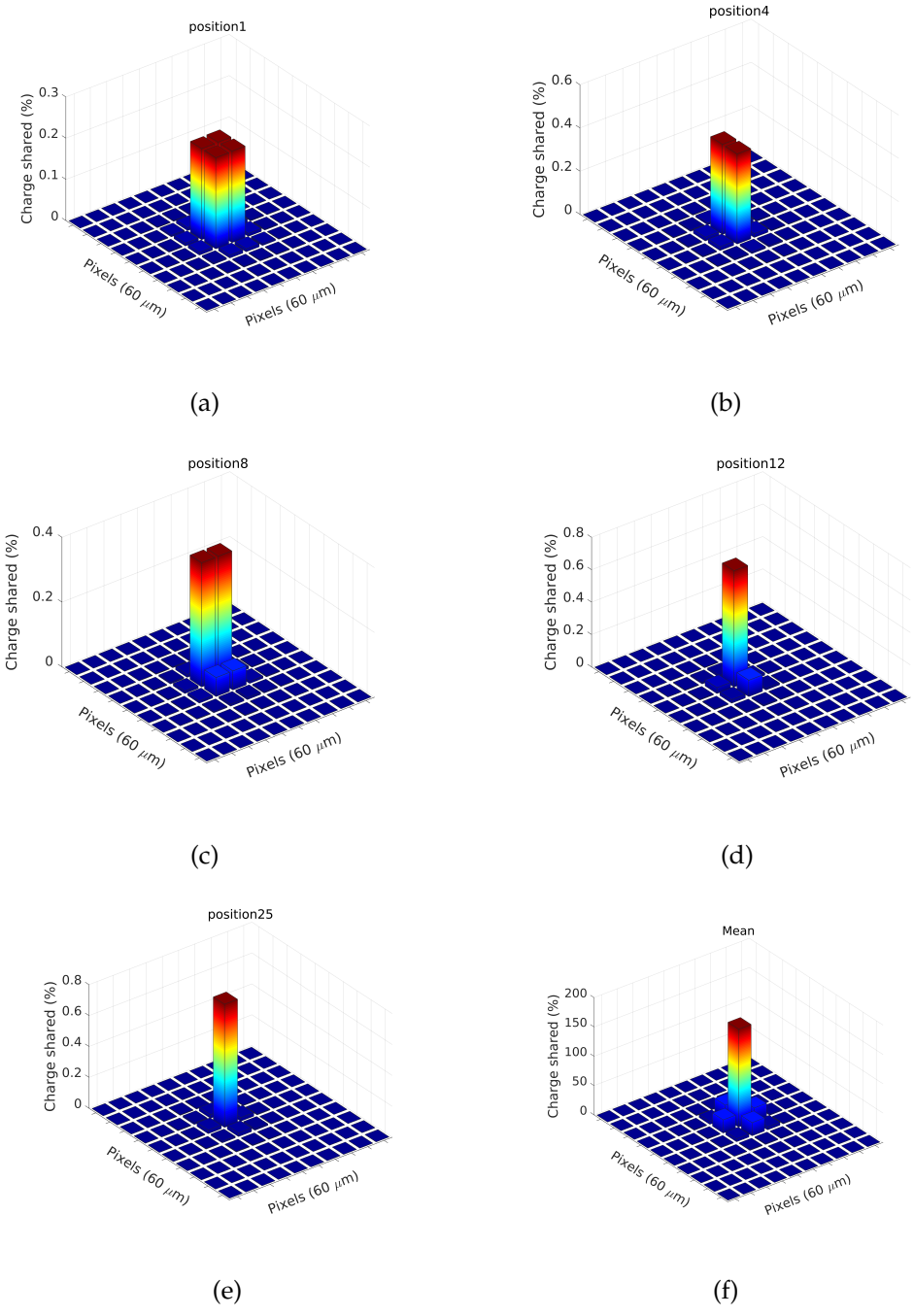

FIGURE 6.14: Fraction of charge collected in each pixel versus impact positions of the impinging electron beam. For the corresponding impact position, please refer to Figure 6.13 (right). (a) Impact point is on position 1 (P_1). (b) Impact point is on position 4 (P_4). (c) Impact point is on position 8 (P_8). (d) Impact point is on position 12 (P_{12}). (e) Impact point is on position 25 (P_{25}) and (f) average fraction of charge collected in each pixel. This average is obtained from all 49 impact positions of the electron beam and it represents the point spread function of the detector.

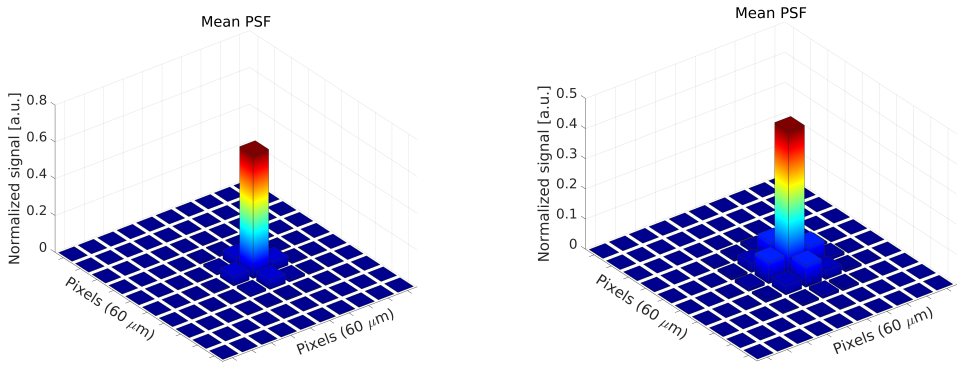

(a) (b)

FIGURE 6.15: Fraction of charge collected in each pixel using 300 keV and 200 keV electrons hitting the center pixel at random impact positions. (a) average fraction of charge collected in each pixel for 300 keV electrons. (b) average fraction of charge collected in each pixel for 200 keV electrons.

Chapter 7

Imaging Performance of the EDET-80 Detector

There are serveral quantities that quantify the imaging capabilities of detectors such as the Signal-to-Noise Ratio (SNR), the Modulation Transfer Function (MTF) and the Detective Quantum Efficiency (DQE). Here, we investigate the imaging capabilities of the EDET-80 detector in terms of these parameters using low and high electron dose. In addition, we compare the imaging performance of the EDET-80 to that of commercially available direct electron detectors.

7.1 Detective Quantum Efficiency

In addition to Poisson noise inherent in the detected electrons, detectors always introduce additional noise during detection and readout of the signal. The detective quantum efficiency is an important figure of merit characterizing the detector performance in terms of added extra noise by the detector to the recorded image, which results in a degradation of the input $\mathrm{SNR}_{\mathrm{in}}$ and the quality of the recorded image, as illustrated in Figure 7.1. It is by definition the square of the SNR at the output of the detector ($\mathrm{SNR}_{\mathrm{out}}$) divided by the square of $\mathrm{SNR}_{\mathrm{in}}$ [164]

$$DQE = \frac{SNR_{out}^2}{SNR_{in}^2} \tag{7.1}$$

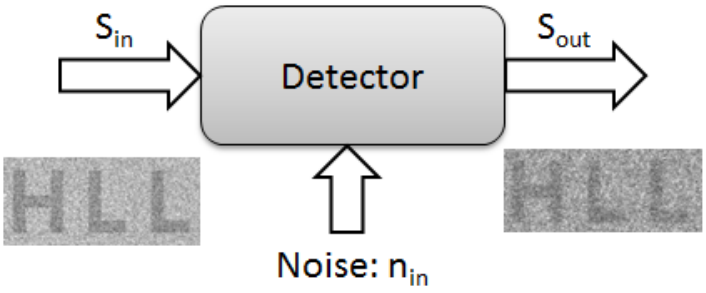

FIGURE 7.1: Additional noise added by the detector to the input signal. S_{in}, n_{in} and S_{out} represent signal at the input of the detector, noise added by the detector and the signal at the output of the detector, respectively. The input signal contains only Poisson noise and the output signal includes, in addition to the Poisson noise, the noise added by the detector.

An example demonstrating the importance of the DQE of a detector is the comparison of images recorded by two detectors of different DQEs. This is presented in the Figure 7.2, which shows images of an object recorded by a detector with 25% DQE (i.e. DQE_1=25%) and an improved detector with 50% DQE (i.e. DQE_2=50%). It is interesting to note that the image recorded by a detector with high DQE is less noisy than that recorded by a detector with low DQE. Hence, it is crucial to have a detector whose DQE is as high as possible.

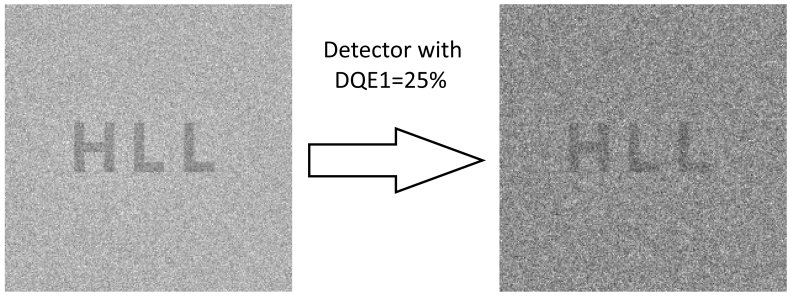

(a)

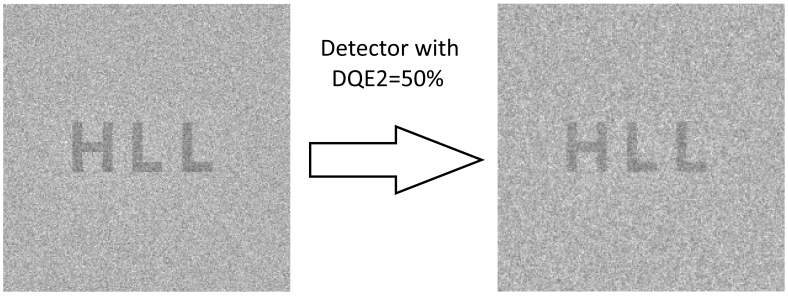

(b)

FIGURE 7.2: Output images of a sample made of carbon letters and recorded by two detectors with DQE_1=25% and DQE_2=50%. (a) Output image recorded by a detector with DQE_1=25% and (b) output image recorded by a detector with DQE_2=50%.

Evidently, an ideal detector would not degrade the $\mathrm{SNR}_{\mathrm{in}}$ (i.e. $\mathrm{SNR}_{\mathrm{in}}$=$\mathrm{SNR}_{\mathrm{out}}$) and would have 100% DQE, which means that all the incoming electrons hitting the detector are detected with the same weight and no further noise is added. However, an ideal detector does not exist, which means that the DQE is always smaller than 100% because of additional noise sources. In low electron-dose imaging applications, it is highly beneficial if images can be recorded with high SNR. For a necessary SNR, this can be achieved by either increasing the intensity of the incident electron beam (i.e. high electron dose) or by increasing the acquisition time. These two options are impractical as radiation damage in beam sensitive specimens

limits the dose on the sample. Therefore, a detector with high DQE is desirable. Figure 7.3 shows the dependence of image quality on the electron dose and the DQE of the detector. Our findings regarding the relationship between the dose and the DQE of the detector highlight that a detector with 50% DQE needs only a half of the electron dose to achieve the same image quality as recorded by a detector with 25% DQE. This is due to the fact that the SNR at the output depends on the DQE as shown in equation 7.1.

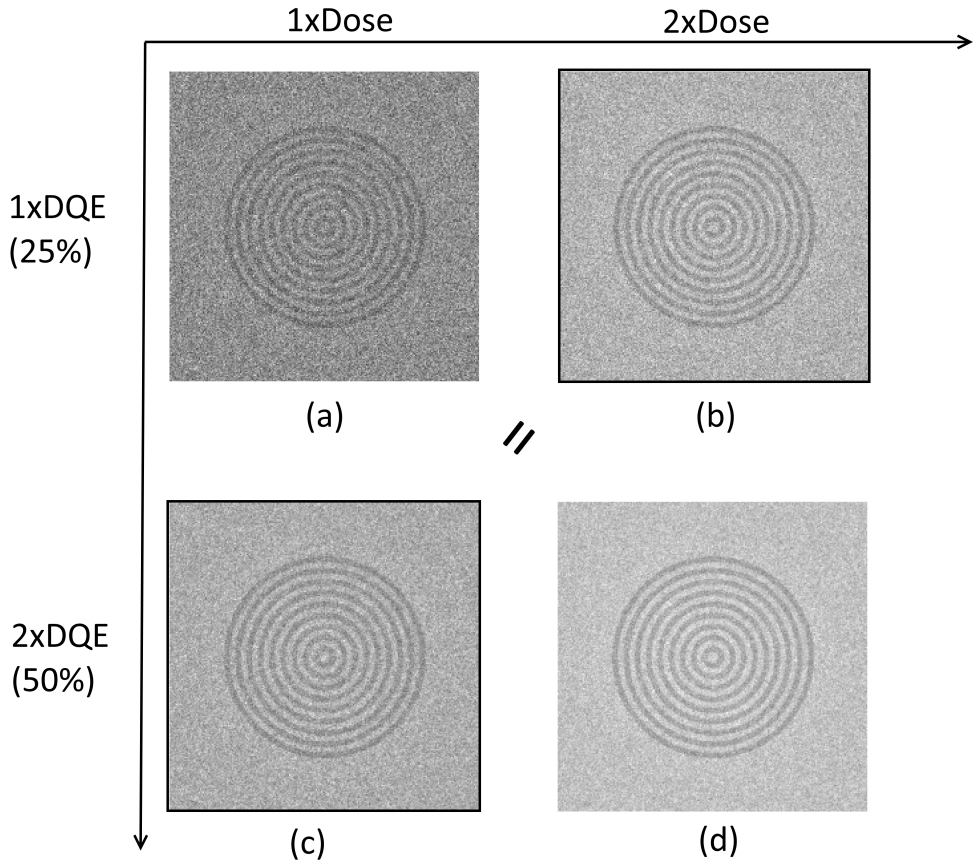

FIGURE 7.3: Dependence of image quality on the electron dose and the DQE of the detector. A detector with 25% DQE would require two times the electron dose to obtain the same image quality as recorded by a detector with 50% DQE. The higher the DQE, the better the image quality at the same electron dose and thus the lower the radiation damage of the sample being imaged.

Here, we calculated the DQE of the EDET-80 detector starting from the generation of primary electrons obeying Poisson statistics, creation of e-h pairs by primary electron interactions with the detector and passing through all the stages of the detector system contributing to the signal formation to get the digitized signal at the output. Hence, the output signal of the detector contains the contribution of various noise components added at each stage. The first source of noise is associated with the electron beam as electrons emitted from a source obey Poisson statistics given by

$$P(x, N) = \frac{N^x}{x!} e^{-N}. \tag{7.2}$$

Where x are events (x=1, 2, . . . , n) and N is the expected number of events (i.e. mean number of electrons). Figure 7.4 shows a Poisson distribution for N=10.

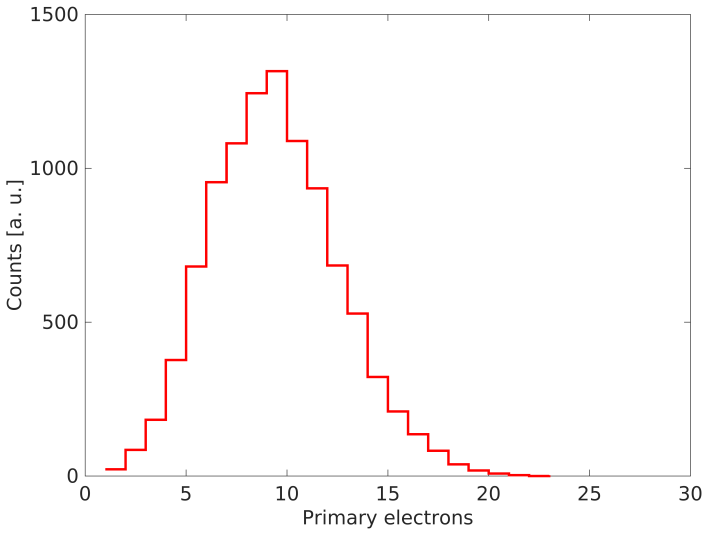

FIGURE 7.4: Example of Poisson distribution with a mean N=10 and a standard deviation $\sigma = \sqrt{10}$.

Poisson noise (i.e. shot noise) is a direct consequence of the Poisson statistics

of electrons emitted from a source and determined by the standard deviation of the Poisson distribution. Therefore, the input signal ($\mathrm{S_{in}}$) has always Poisson noise, which is a major factor limiting the SNR of the recorded image. The mean input signal (i.e. mean number of electrons) and the standard deviation of electrons hitting the detector are $\mathrm{N_{in}} = \overline{\mathrm{S}}_{\mathrm{in}}$ and $\sigma_{\mathrm{in}} = \sqrt{\mathrm{N_{in}}}$, respectively. This means that Poisson noise, $\sigma_{\mathrm{in}} = \sqrt{\mathrm{N_{in}}}$, scales as the square root of the mean number of primary electrons hitting the detector and the $\mathrm{SNR_{in}}$ is thus given by

$$SNR_{in} = \frac{\overline{S}_{in}}{\sigma_{in}} = \frac{N_{in}}{\sqrt{N}_{in}} = \sqrt{N}_{in}. \tag{7.3}$$

For instance, for $\mathrm{N_{in}}$=10 events the $\mathrm{SNR_{in}}$ becomes $\mathrm{SNR_{in}} = \sqrt{10}$.

Statistical fluctuations of the energy deposited by primary electrons passing through a 50 µm thick silicon sensor of the EDET-80 detector results also in statistical fluctuations of the created e-h pairs giving rise to another source of detection noise (i.e. Landau noise). It is worthwhile noting that Poisson noise and Landau noise are inevitable and can not be eliminated. Other sources of noise are, for example, DCD noise of σ_{dcd}=50 nA, DEPFET noise of σ_{d}=9 nA and Fano noise of σ_{Fano}=30 e^- estimated by [78]

$$\sigma_{Fano} = \sqrt{\Delta N_{eh} \times F}. \tag{7.4}$$

Here $\Delta\mathrm{N_{eh}}$ is the mean number of e-h pairs created by a primary electron of 300 keV in the simulated detector, shown in Figure 6.4, and F is the Fano factor (for silicon F=0.1).

At the output of the detector, we obtain the output signal, $\mathrm{S_{out}}$, which includes

the contributions of different noise sources as well as the digitization noise. $\mathrm{S_{out}}$ is expressed in terms of ADUs and can be calculated in terms of detected primary electrons using the plots shown in Figure 6.7(c). Consequently, the calculated average of the total signal at the output, $\overline{\mathrm{S}}_{\mathrm{out}}$, and the output noise given by the standard deviation σ_{out} of the output signal distribution ($\mathrm{S_{out}}$) allow finally for the calculation of $\mathrm{SNR_{out}}$ given by

$$SNR_{out} = \frac{\overline{S}_{out}}{\sigma_{out}}. \tag{7.5}$$

In the following, three quantities describing the detector performance will be investigated, namely the counting capability, the SNR and the DQE based on three scenarios investigating certain aspects of a detector.

- In the first scenario—the infinite pixel approach, the sensor is not pixelated and defined as one large pixel. This has the advantage of eliminating the charge sharing effect and minimizing the noise as in a pixelated detector each pixel adds a given amount of noise to the signal produced in that pixel. This scenario resembles a non-pixelated detector to measure the flux of a beam (like a photo-diode).

- In the cluster scenario, the center of a 10 by 10 pixel subsection of the detector is irradiated with a pencil electron beam at random impact positions. In this scenario we want to investigate the effect of the charge spread over pixels on the imaging performance of the detector.

- In the third scenario, the whole detector is pixelated and exposed to a uniform planar electron beam of a variable flux. The detector performance is then investigated as a function of the electron dose. In the following, we will discuss

these three scenarios in more detail.

7.1.1 DQE Calculation from Infinite Pixel

In this approach, the EDET-80 detector is not pixelated and exposed to a pencil electron beam of 300 keV obeying Poisson statistics and impinging the detector at the center, as illustrated in Figure 7.5. Events ranging from single electrons to multiple electrons (e.g. 300 events) were simulated. Both a model close to the final detector geometry and a free-standing detector (i.e. detector without silicon housing) are investigated as the later one is useful as a benchmark for comparison purposes.

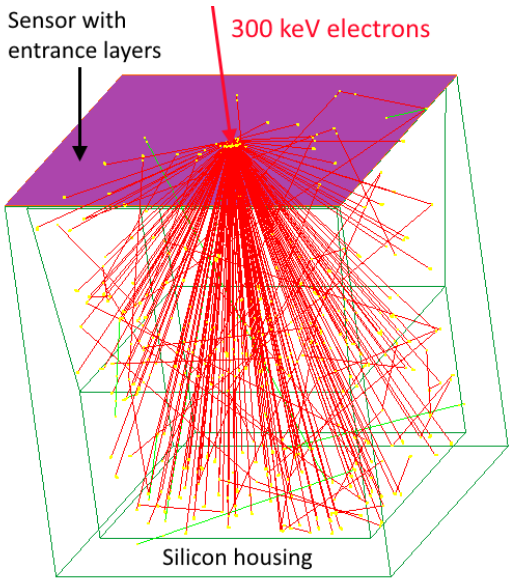

FIGURE 7.5: Simulation setup used to investigate the infinite pixel scenario. An EDET-80 detector with silicon housing including a 35 mm vacuum gap was used. The green trajectories represent the emitted X-rays and the red trajectories represent electron tracks. To simplify the visualization only 200 primary electrons are displayed here.

The $\mathrm{SNR}_{\mathrm{in}}$ and the $\mathrm{SNR}_{\mathrm{out}}$ are calculated from equation 7.3 and equation 7.5, respectively. The output signal contains all noise contributions and it is calculated in terms

of ADU, which are converted into detected primary electrons using the EDET-80 response curves depicted in Figure 6.7(c). The detected primary electrons ($\mathrm{PE_{out}}$) as a function of incident primary electrons ($\mathrm{PE_{in}}$) are shown in Figure 7.6(a), which demonstrates the counting capability of the EDET-80 detector. The shaded areas shown in Figure 7.6(a) represent all noise contributions considered in this calculation and the dashed-dotted lines represent the contribution of Poisson noise. These results highlight that our EDET-80 detector has very small readout noise compared to shot noise, which is the dominant noise source. We calculated the $\mathrm{SNR_{out}}$ at different DCD gain settings as shown in Figure 7.6(b) and Figure 7.6(c), displaying the same data in two different scales, namely the linear scale and the logarithmic scale. The logarithmic scale simplifies the interpretation of the data, especially at a low electron dose. In addition, the comparison between the $\mathrm{SNR_{out}}$ obtained with the EDET-80 detector with silicon housing and the $\mathrm{SNR_{out}}$ of a free-standing EDET-80 detector (see Figure 7.6(d)) confirms the capability of our advanced EDET-80 detector design to detect electrons with high SNR.

Figure 7.6(b,c) show that the $\mathrm{SNR_{out}}$ curves approache the $\mathrm{SNR_{in}}$ curve when using DCD gain settings k=2, k=1 and k=0.667. This overestimation of the $\mathrm{SNR_{out}}$ starts at a given number of primary electrons and can be explained by the fact that the signal saturates and the noise contribution tends to zero, as shown in Figure 7.6(a). In the calculation of the DQE we multiply the DQE by the slope of the curves shown in Figure 7.6(a) to avoid this overestimation. This correction was performed for DCD gain setting of $k \leqslant$0.667 as the slopes of the curves shown in Figure 7.6(a), at these DCD gain values, tend to zero when the signal get saturated.

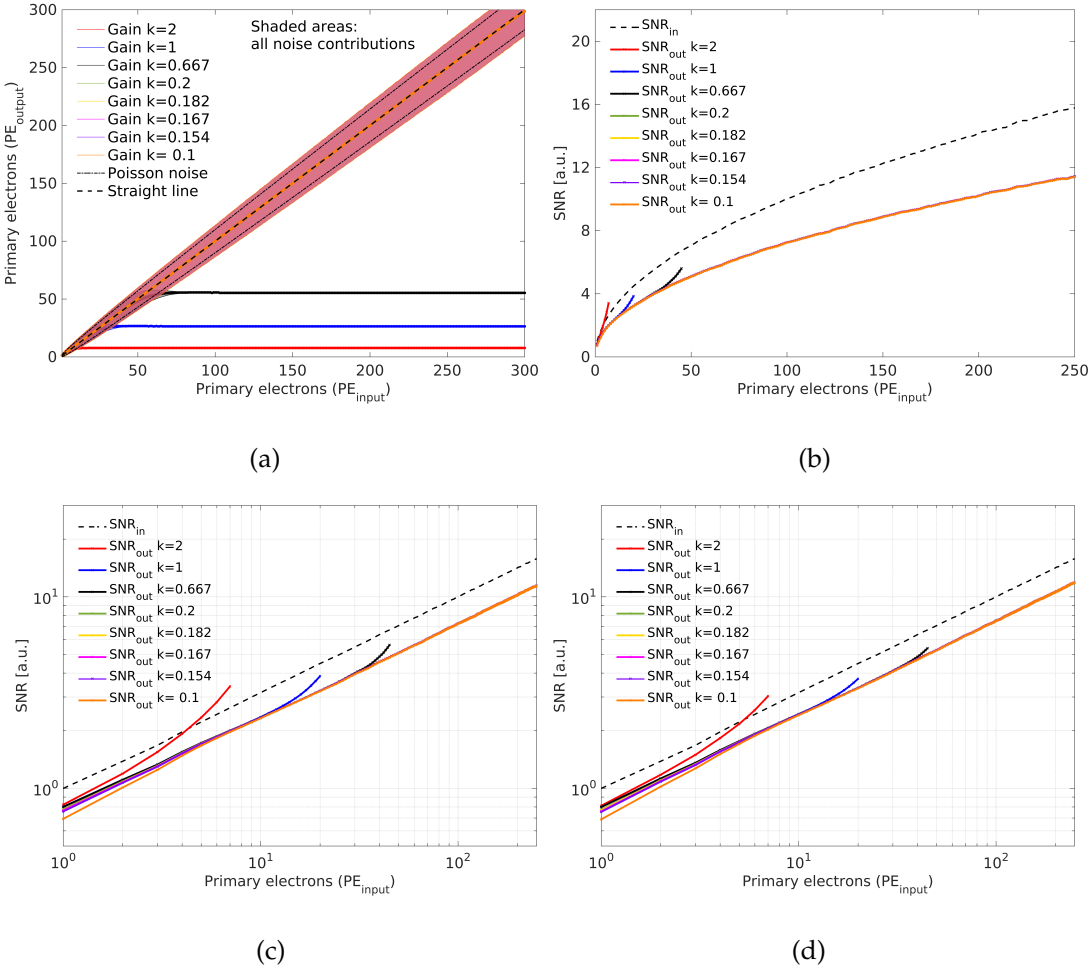

FIGURE 7.6: Detection performance of the EDET-80 detector irradiated with 300 keV electrons and operating at different DCD gain settings. (a) Detected electrons ($\mathrm{PE_{output}}$) as a function of number of primary electrons ($\mathrm{PE_{input}}$), (b) SNR in linear scale at the input and output of the detector at different gain settings, (c) SNR in logarithmic scale at the input and output of the detector at different gain settings. (a), (b) and (c) are obtained from the EDET-80 with silicon housing. (d) SNR in logarithmic scale at the input and output of the EDET-80 without silicon housing.

After having calculated the SNR at the input and output of the detector, we insert them now into equation 7.1 to determine the DQE of the infinite pixel detector. Figure 7.7 shows the resulting DQE of two detector configurations obtained from the infinite pixel approach. These plots of the DQE show that the DCD gain

setting of k=2, k=1 and k=0.667 are suitable for low-dose imaging applications. For example, the DQE at PE_{in}=1 and k=0.667 of EDET-80 detector with silicon housing is ∼64%, which is useful for low dose applications. Other gain settings (i.e. $k \leqslant 0.2$) preserve the full PE_{in} range and the mean DQE is about 52% for the analyzed PE_{in} range. Hence, this virtual single pixel detector needs approximately double the flux compared to a perfect detector to achieve the same statistical significance for a measurement. As the electron dose increases, the readout noise of the detector becomes progressively less significant than the shot noise. Therefore, the DQE for $k \leqslant 0.2$ reaches a plateau and remains almost constant as the electron dose increases, which means that a further increase in the dose does not affect the DQE. The DQE of a free-standing EDET-80 detector is higher than the DQE of the EDET-80 with silicon housing, and this is due to the electrons backscattered from the silicon housing. The fraction of backscattered electrons is largely reduced in the EDET-80 detector design, but it is still affecting the detector performance.

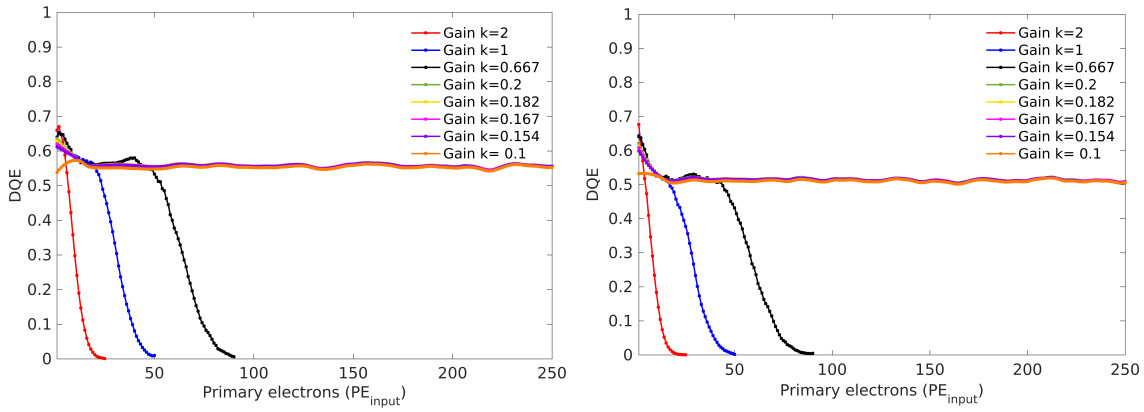

FIGURE 7.7: Detective quantum efficiency of two detector designs obtained from an infinite pixel approach as a function of number of primary electrons of 300 keV. (a) DQE of the EDET-80 without silicon housing and (b) DQE of the EDET-80 with silicon housing.

Decreasing the energy of primary electrons hitting the detector from 300 keV to 200 keV results in a significant increase in the signal and consequently better DQE, as shown in Figure 7.8. However, it may not be possible to operate the EDET-80 with the DCD gain setting of k=2.

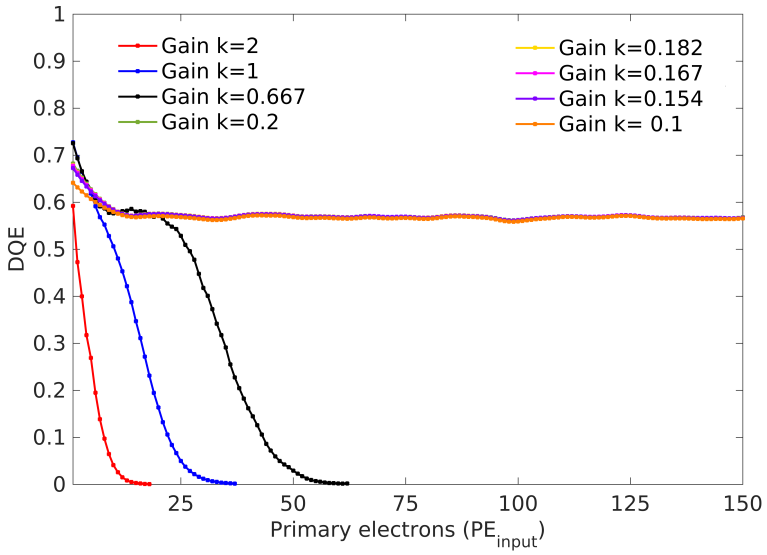

FIGURE 7.8: Detective quantum efficiency of the EDET-80 with silicon housing obtained from an infinite pixel approach as a function of number of primary electrons of 200 keV.

7.1.2 DQE Calculation from Cluster

This approach investigates the effect of the charge spread over pixels on the SNR and the DQE of the detector, which is termed Clustered Detective Quantum Efficiency (CDQE). To evaluate this effect, the same setup shown in Figure 6.13 was used taking into account the Poisson statistics of electrons hitting the detector. We chose a cluster of 10 by 10 pixels and the center pixel of the cluster was irradiated with single primary electrons of 300 keV. Each primary electron hits the center pixel at a random impact position, as shown in Figure 7.9 (right), and creates a given signal. The distribution of the generated signal in the cluster depends on the impact

position of the primary electron, as shown in Figure 6.14.

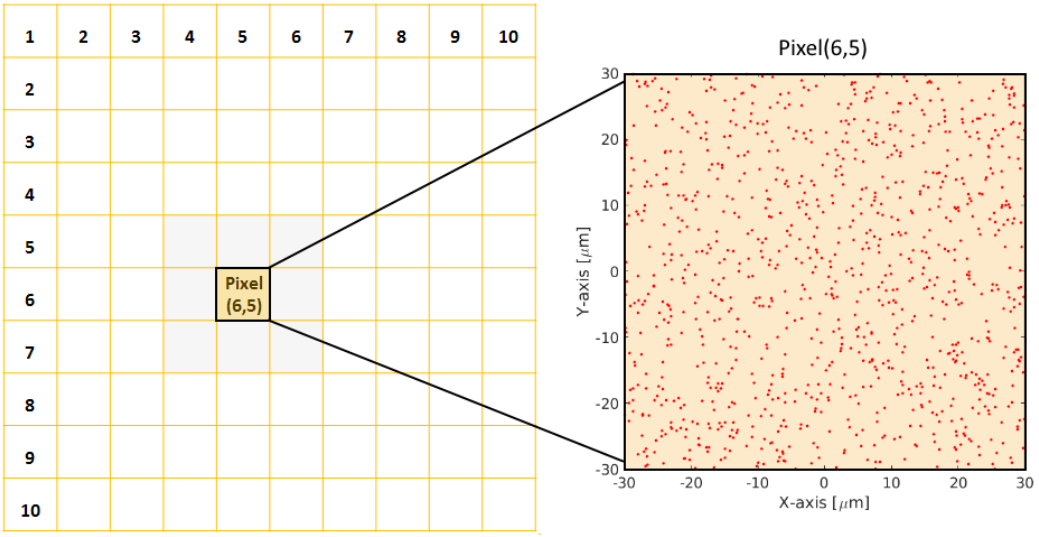

FIGURE 7.9: Example of 1000 random impact positions (right) in the center pixel of a 10 by 10 pixel subsection (left). Red dots highlight the random impact positions.

First, we simulated 1000 dark frames, where a set of frames is captured in the absence of electrons, to calculate the mean count per pixel per dark frame and the standard deviation for different DCD gain settings. The simulation of dark frames is necessary when simulating a pixelated detector exposed to a low electron dose. For instance, the irradiation of a cluster of 10 by 10 pixels with one primary electron (i.e. one primary electron per 100 pixels) may results in a charge sharing between the irradiated pixel and the neighboring pixels, as discussed in section 6.4. However, some pixels may contain only noise such as DCD and DEPFET noise, which are normally distributed with a mean μ=0 and standard deviations of σ_{dcd} and σ_{d}, respectively. Therefore, some pixels can have negative values, which can not be digitized by the DCD. For this reason the signal in each pixel of the dark frames is lifted in both the simulation and actual physical detector by $5\sigma_{\mathrm{dcd}}$, thus solving the problem of the negative pixel values. This means that each pixel of the irradiated

detector contains signal from primary electrons, noise and from the $5\sigma_{\mathrm{dcd}}$ lifting. Hence, the subtraction of the dark frame counts from the cluster frame counts must be performed before calculating the number of detected primary electrons, the SNR and the DQE.

The results obtained from the simulation of dark frames are shown in Table 7.1. The results are almost identical for all DCD gain settings.

TABLE 7.1: Mean ($\mathrm{m_{df}}$) and standard deviation (σ_{df}) of the counts per pixel calculated in ADU from dark frames at different DCD gain settings.

Gain k	2	1	0.667	0.2	0.182	0.167	0.154	0.1
$\mathrm{m_{df}}$	1.492	1.491	1.491	1.491	1.491	1.491	1.491	1.491
σ_{df}	0.541	0.527	0.525	0.524	0.523	0.523	0.523	0.523

In the next step, we simulated the cluster consisting of 10×10 pixels by irradiating the center pixel of the cluster with a pencil electron beam of 300 keV at 100,000 random impact positions. This approach can be divided into several steps:

- Step 1: For example, one primary electron hits the pixel at a random impact position (see Figure 7.9) and produces signal, which is distributed among the pixels of the cluster.

- Step 2: A signal of $5\sigma_{\mathrm{dcd}}$ per pixel is added to lift the generated signal in the cluster and avoid having negative pixel counts. The simulated frame is then digitized taking into account all the DCD gain settings.

- Step 3: The mean count ($\mathrm{m_{df}}$), shown in Table 7.1, is subtracted from the digitized signal in each pixel of the cluster, as calculated in step 2.

- Step 4: A threshold is used and only pixel counts larger than 4 times the standard deviation of dark frames ($4\sigma_{\mathrm{df}}$) are considered as a signal.
- Step 5: The relationship shown in Figure 6.8 is used to convert the signal calculated in terms of ADU into detected electrons.
- Step 6: The integration of the detected electrons in the cluster gives S_1—sum of detected electrons, which should in this example sum to one primary electron.

This simulation is repeated 100,000 times for each event to have significant statistics. As a result, we obtain the mean number of the detected electrons in the cluster and the corresponding standard deviation. Please note that so far we have only simulated single electron events, which are Poisson distributed. The same simulation procedure was performed for multiple electron events (i.e. from 2 to 300 events).

It is important to note that the contribution of backscattered electrons to the total signal generated in the cluster is negligible due the small size of the cluster (i.e. 10 by 10 pixels) and the large angle of the backscattered electrons. Therefore, the plots shown in Figure 6.8 are used to convert the ADUs into primary electrons instead of Figure 6.7(c).

Figure 7.10 shows the detected electrons as a function of primary electrons hitting the detector, the $\mathrm{SNR}_{\mathrm{in}}$, the $\mathrm{SNR}_{\mathrm{out}}$ and the resulting CDQE of the EDET-80 detector. In comparison to the infinite pixel approach, the CDQE degrades slightly and shows a value of $\sim$62% at $\mathrm{PE}_{\mathrm{in}}$=1 using DCD gain setting of k=0.667. For low DCD gain settings (k <0.667), the CDQE becomes smaller than 40% at $\mathrm{PE}_{\mathrm{in}}$=1. This can be explained by the spread of the charge between the cluster pixels and the noise (e.g. readout noise) added in each pixel of the cluster. At high electron dose, the CDQE exceeds $\sim$50% and remains almost constant. This slight increase is due to the negligible contribution of backscattered electrons to the total signal generated in the cluster.

The results we obtained from the cluster approach demonstrate the imaging capabilities of the EDET-80 detector for low dose and large dynamic range applications. For instance, DCD gain settings such as k=2, k=1 and k=0.667 are suitable for low-dose imaging applications as they allow for single electron detection, and lower DCD gain settings are beneficial to operate the detector at larger dynamic range.

It is worth noting that the signal generated in the detector gets smaller when it operates with low DCD gain settings and under low electron dose conditions. Therefore, the contribution of the detector noise to the total signal may become significant and can affect the detector imaging performance (e.g. DQE). To investigate the impact of this noise on the CDQE of the EDET-80 detector, we performed the same calculation by turning off all the noise sources (i.e. DCD noise, DEPFET noise and Fano noise) in the simulation. The obtained results are depicted in Figure 7.11, showing that the CDQE improves significantly when operating the EDET-80 detector with low DCD gain settings.

Using 200 keV instead of 300 keV primary electrons can be regarded as an advantage. A higher signal produced by low energy electrons reduces the relative weight of the detector noise when using low electron dose and low DCD gain settings. We performed the same calculations to investigate the CDQE of the EDET-80 detector irradiated with 200 keV. This results in an improved CDQE and, in particular, for low electron dose. The resulting CDQE shown in Figure 7.12 surpasses that achieved with 300 keV. However, the DCD gain setting of k=2 may not work properly due to the large signal produced by 200 keV electrons. These investigations demonstrate that the EDET-80 detector is capable of operating in various TEM configurations (e.g. TEM operating at 200 keV and 300 keV).

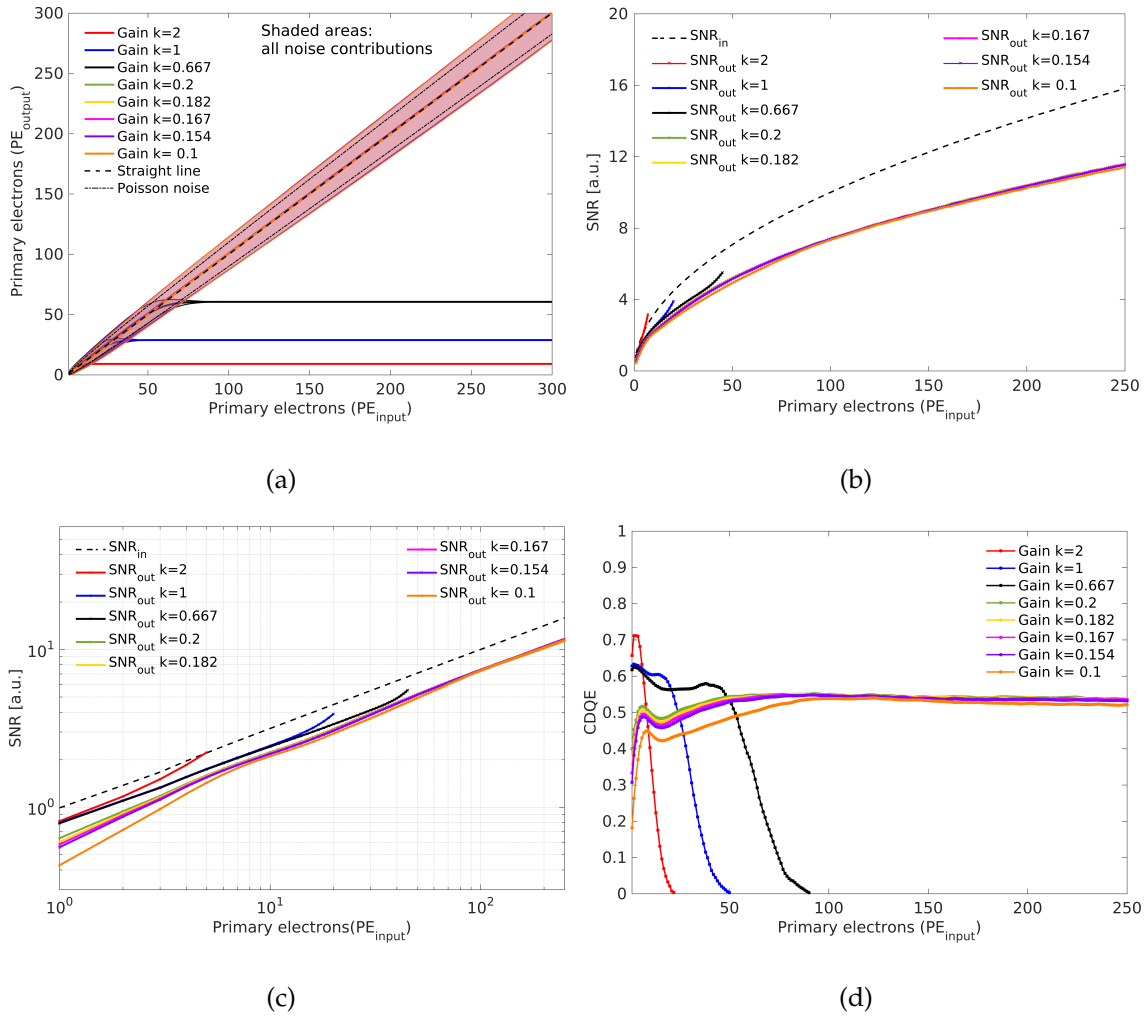

FIGURE 7.10: Detection performance of EDET-80 detector using different DCD gain settings. (a) Detected electrons ($\mathrm{PE_{output}}$) as a function of primary electrons ($\mathrm{PE_{input}}$). (b) SNR in linear scale at the input and output of the detector. (c) SNR in logarithmic scale at the input and output of the detector and (d) clustered detective quantum efficiency.

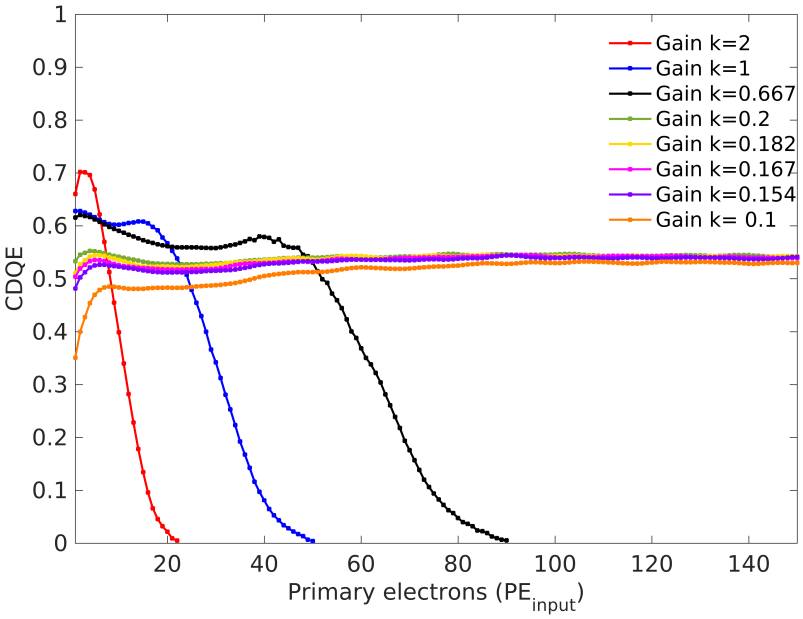

FIGURE 7.11: CDQE of the EDET-80 with silicon housing as a function of number of primary electrons of 300 keV. DCD, DEPFET and Fano noise are excluded.

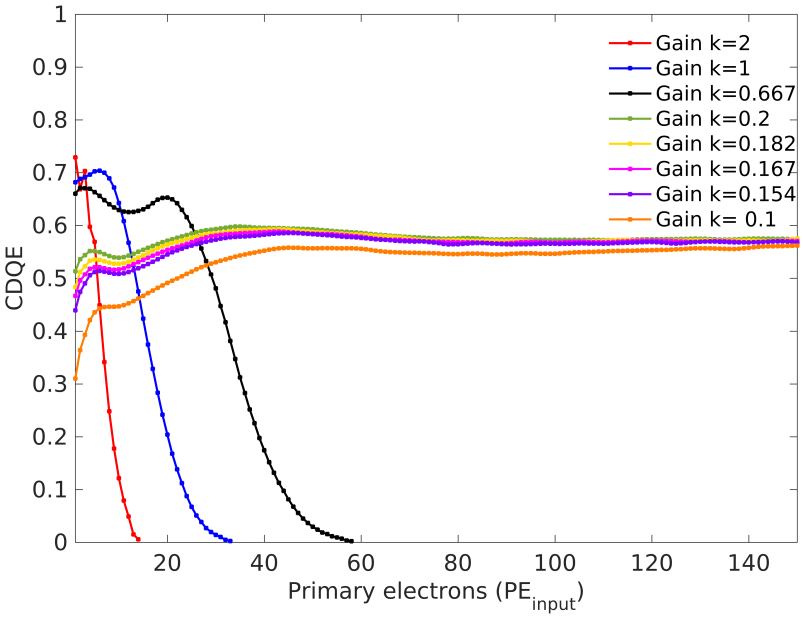

FIGURE 7.12: CDQE of the EDET-80 with silicon housing as a function of number of primary electrons of 200 keV.

7.1.3 DQE as a Function of Electron Dose

The same setup illustrated in Figure 6.4(a) was used to explore the dependence of the DQE of the EDET-80 detector on the electron dose at 300 keV. In this simulation, the EDET-80 quadrant detector is irradiated with a planar electron beam of different flux settings. The flux varies from 0.001 to 20 electrons per pixel per frame (epf): Flux=[0.001, 0.005, 0.01, 0.02, 0.04, 0.07, 0.1, 0.2, 0.3, 0.5, 0.75, 1, 1.5, 2, 3, 4, 5, 10, 15, 20]. For each electron dose, we performed 300 simulations (i.e. 300 frames) to have significant statistics. Each simulated frame has an additional signal of $5\sigma_{\mathrm{dcd}}$ per pixel to avoid producing negative pixel counts, as explained in the cluster approach. It should be mentioned here that the fraction of backscattered electrons increases slightly when a planar beam is used to irradiate the detector instead of a pencil beam. Therefore, the results shown in Figure 6.7(c) were reproduced using a planar beam to take into consideration this small increase in the fraction of backscattered electrons contributing to the total signal.

The simulated frames are digitized and after subtracting the mean counts $\mathrm{m_{df}}$ from the signal obtained in the frames, a threshold is used and only counts larger than 4 times the standard deviation of dark frames ($4\sigma_{\mathrm{df}}$) are considered. Figure 7.13 shows examples of four frames recorded with an electron dose of 10, 5, 1 and 0.1 epf, respectively. Obviously, the intensities per frame decreases with decreasing electron flux. The insets in Figure 7.13(j) and Figure 7.13(k) reveal the capability of the EDET-80 to detect single electron events with significant SNR. Figure 7.14 shows plots of the mean number of detected electrons per frame, the resulting SNR and the DQE as a function of electron dose per frame. It is worth mentioning that the mean DQE of the EDET-80 reaches $\sim$71% at low electron dose (i.e. electron dose from 0.001 to 0.3 epf) when using high DCD gain settings such as k=2. Consequently, the EDET-80 detector would be able to detect efficiently a limited electron dose to

produce images with high SNR.

To facilitate the investigation of the noise performance of the EDET-80 detector, the SNR at the detector output is plotted in logarithmic scale, as shown in Figure 7.14(c). At an electron dose smaller than 10 epf, shot noise decreases and the relative weight of readout noise increases (readout noise remains always constant), which significantly improves the SNR at the output and consequently the DQE of the detector. However, for a significantly high electron dose (i.e. a dose higher than 10 epf), the DQE becomes dose-independent because the relative weight of the readout noise decreases with increasing electron dose and is thus almost negligible compared to the shot noise, which increases proportionally with the electron dose. These findings confirm that the EDET-80 detector is capable of recording low-electron dose frames with high SNR allowing thus detecting single electrons with high probability.

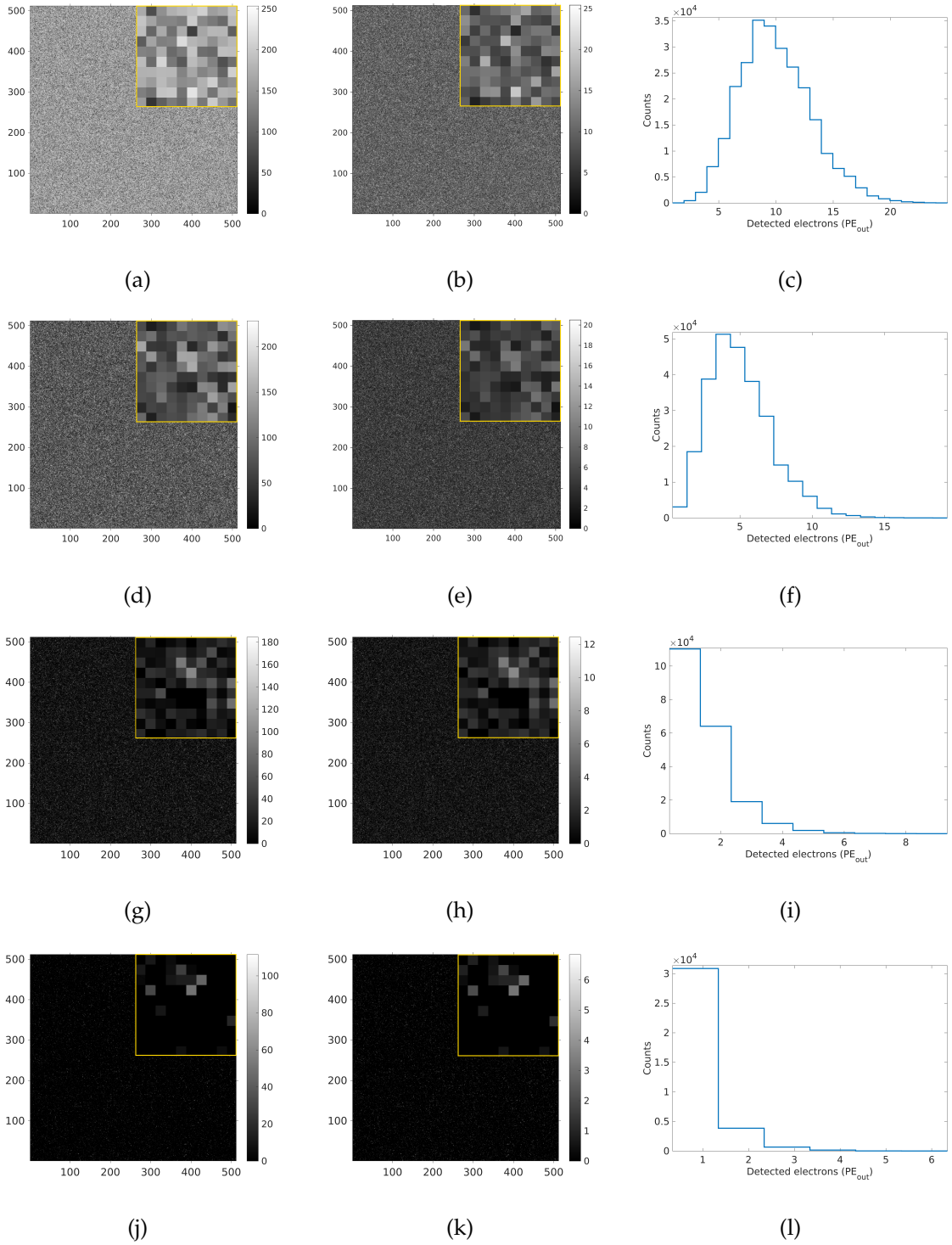

FIGURE 7.13: Examples of single frames recorded with the EDET-80 detector using 300 keV electrons. The insets show enlarged portions of the images. Frames from the top to the bottom are captured using a uniform planar electron beam producing an average flux of 10, 5, 1 and 0.1 electrons per pixel per frame, respectively. The left column shows ADU counts, middle column detected electrons and the right column histograms of detected electrons.

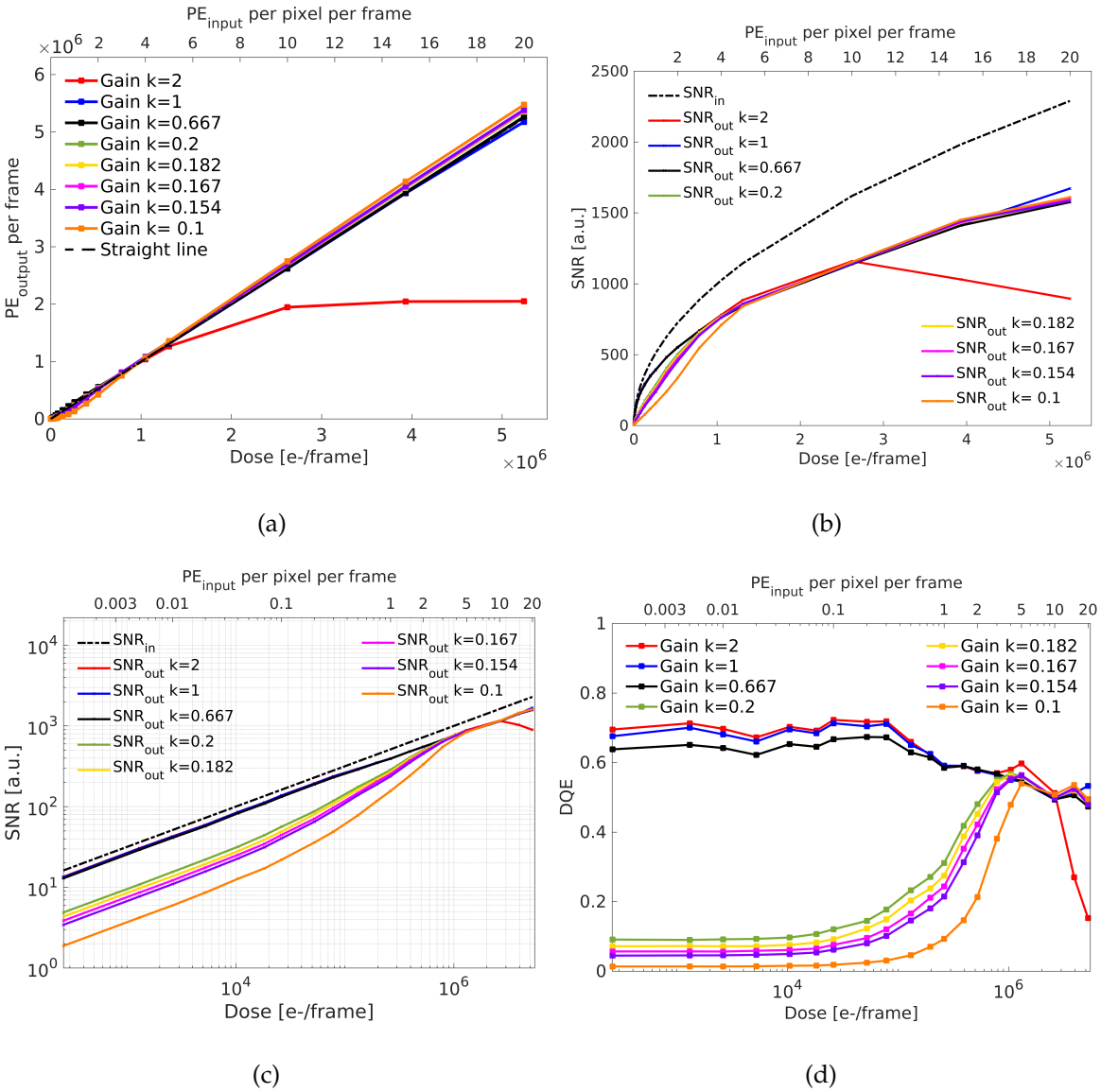

FIGURE 7.14: Detection performance of the EDET-80 detector using different DCD gain settings. (a) Average number of detected electrons (PE_{output}) per frame as a function of number of primary electrons (PE_{input}). (b) SNR_{in} and SNR_{out} in linear scale. (c) SNR_{in} and SNR_{out} in logarithmic scale and (d) DQE of the EDET-80 detector as a function of electron dose.

7.2 Modulation Transfer Function

The Modulation transfer function measures the ability of a detector to transfer the contrast of the object being imaged to the recorded image as a function of spatial frequency. It was explained in more detail in the section 5.4. The theoretical MTF of an ideal pixel detector can be calculated from the response of its square pixel.

7.2.1 MTF Calculation from a Rectangular Function

Since a pixel of the detector can be considered as an individual detector, it is possible to theoretically calculate the MTF of the pixel by assuming that the response of that pixel to the primary electrons is a rectangular function given by [165]

$$f(x) = \begin{cases} 1, & \frac{-a}{2} \leqslant x \leqslant \frac{a}{2}, \\ 0, & \text{elsewhere.} \end{cases} \tag{7.6}$$

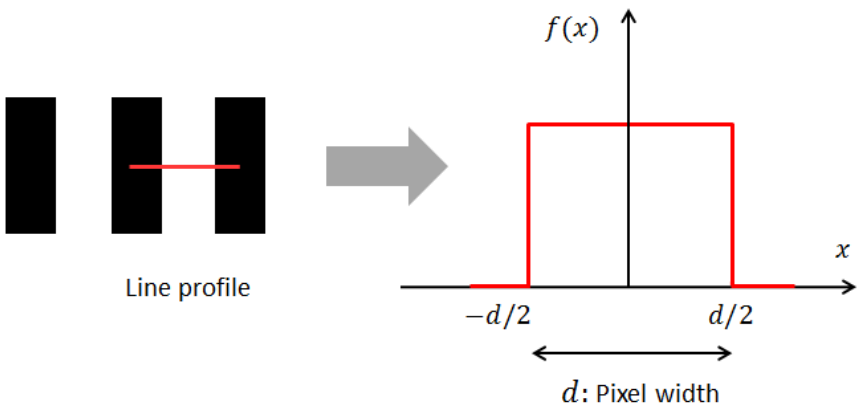

FIGURE 7.15: Rectangular function describing the response of an ideal detector pixel with finite width d.

This equation describes the response of an ideal detector, as shown in Figure 7.15, leaving out any noise contribution, which degrades the signal. The theoretical MTF is the absolute value of the Fourier transformation of the box function given by

$$MTF(\nu) = |\mathcal{F}(f(x))|\,. \tag{7.7}$$

Where ν denotes the spatial frequency expressed in line pairs per millimeter.

$$\begin{aligned} MTF(\nu) &= \left| \int_{-\infty}^{-\infty} f(x)\exp(2\pi i\nu x)\mathrm{d}x \right|, \\ &= \left| \int_{-a/2}^{a/2} \exp(2\pi i\nu x)\mathrm{d}x \right|, \\ &= \left| \frac{1}{2\pi i\nu}\left\{exp(\pi i\nu a) - exp(-\pi i\nu a)\right\} \right|, \\ &= \left| \frac{\sin(\pi\nu a)}{\pi\nu} = a\frac{\sin(\pi\nu a)}{\pi\nu a} \right|. \end{aligned} \tag{7.8}$$

Taking into account the definition of sinc given by

$$\mathrm{sinc}(x) = \frac{\sin(\pi x)}{\pi x}, \tag{7.9}$$

we get

$$MTF(\nu) = a\,|\mathrm{sinc}(\nu a)|\,. \tag{7.10}$$

Figure 7.16 shows the MTFs of three detectors with different pixel sizes (d_1 =40 µm, d_2=50 µm and d_3=60 µm) calculated using equation 7.10. The MTF depends

strongly on the pixel size and the smaller the pixel size, the higher the MTF for a given spatial frequency.

The pixel size determines the maximum spatial frequency that can be captured by the detector which is known as the Nyquist frequency, NF, given by the inverse of two times the pixel size [166]

$$NF = \frac{1}{2 \times d}. \tag{7.11}$$

This means that only spatial frequencies below the NF can be visible in the resulting image. For example, a detector with a pixel size of 60 µm can resolve an image feature of 120 µm.

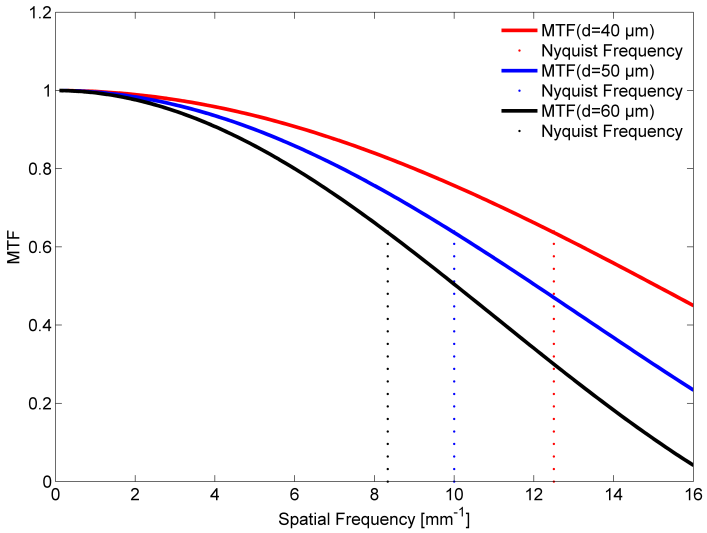

FIGURE 7.16: Theoretical MTFs of detectors with a pixel size of d_1=40 µm, d_2=50 µm and d_3=60 µm. For the corresponding pixel size, these are the best physical MTFs that can be achieved.

7.2.2 MTF of the EDET-80 Detector Operating in Integrating Mode

To determine the MTF of the EDET-80 detector operating in integration mode, we used the slanted edge method, as described in section 5.4. We irradiated the detector with a planar electron beam to record images of the slanted edge, as illustrated in Figure 7.17(a).

The slanted edge consists of a 300 µm thick lead or tungsten layer, absorbing completely primary electrons of 300 keV and producing thus a high-contrast edge image. The signal at the input of the detector can be approximated by a step function, but the output signal might show a relatively blurred edge. We recorded one thousand frames of the tungsten edge with an average flux of 0.1 electrons per pixel per frame—one electron per every 10 pixels in a single frame. Examples of the averaged frames at the input and output of the EDET-80 detector are shown in Figure 7.17(b, c, d, e, f) using two high gain settings (k=2 and k=0.667), which are suitable for low-dose imaging applications and two low gain settings (k=0.154 and k=0.1), which allow for a large dynamic range. The MTF at the input ($\mathrm{MTF_{in}}$) of the detector was also calculated using the slanted edge technique. $\mathrm{MTF_{in}}$ is the highest achievable MTF of the detector because it describes the input spatial frequency of the signal, which has not yet been degraded and includes only Poisson noise.

Figure 7.18 shows the MTFs at the input and output of the EDET-80 detector as a function of spatial frequency, which corresponds to the spatially resolved image detail represented in line pairs per millimeter (lp/mm). The MTF is by convention normalized to unity at zero spatial frequency (0 lp/mm) and decreases with increasing spatial frequency until it reaches zero. A value 1 (i.e. 100%) of the MTF at a spatial frequency ν=0 lp/mm indicates that the contrast is perfectly preserved and a MTF=0 means that the contrast is completely lost and thus the details in the object being imaged can no longer be visualized in the imaging process. Values of

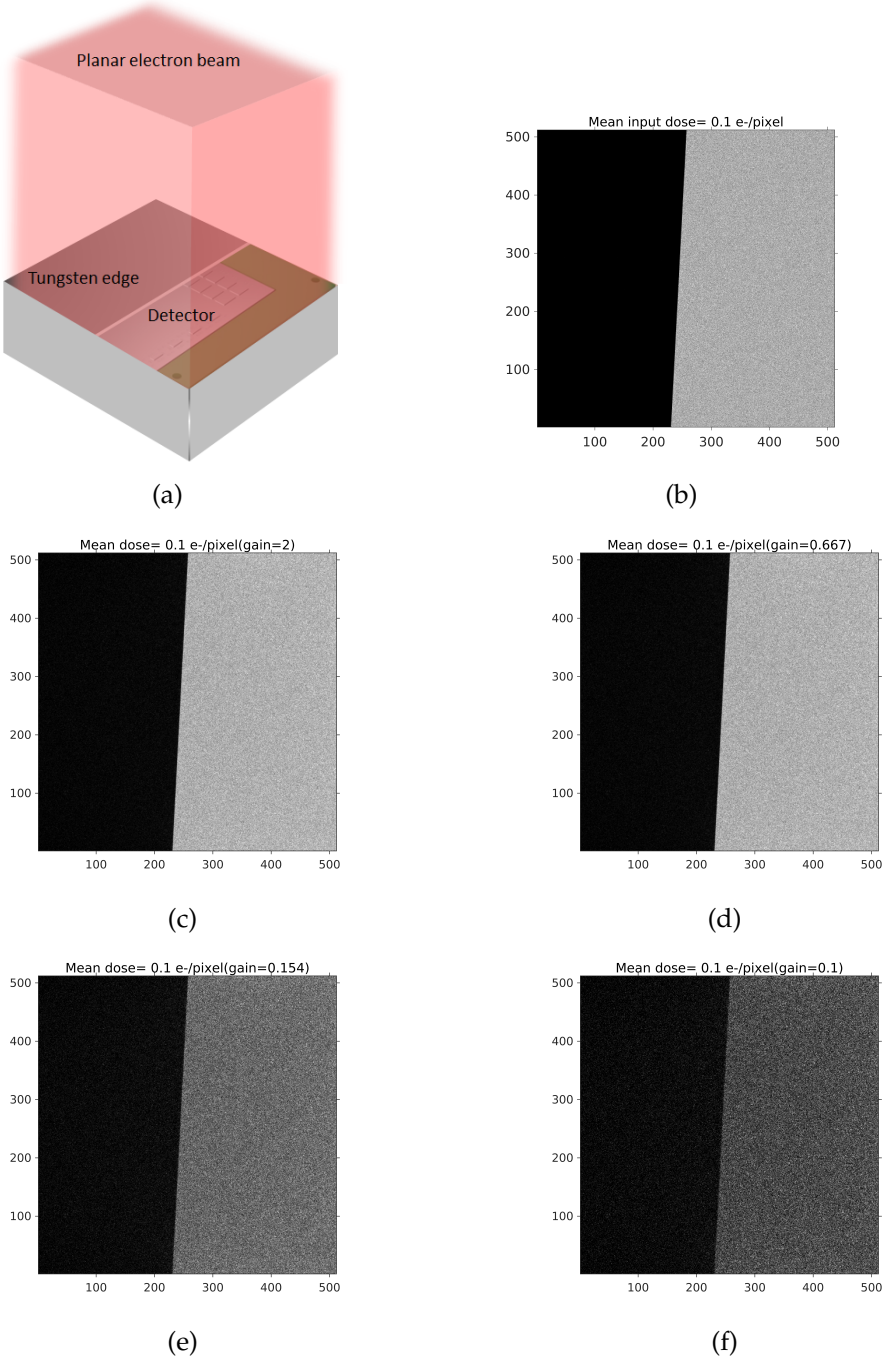

FIGURE 7.17: Slanted edge method to calculate the MTF of the EDET-80 detector. The edge images are obtained by averaging 1000 frames; each frame was obtained with a flux of 0.1 electron per pixel per frame. (a) Schematic illustration of the simulation setup used to calculate the MTF of the EDET-80 detector. (b) Image of the edge at the input of the detector. (c) Image of the edge obtained at a DCD gain setting of k=2. (d) k=0.667. (e) k=0.154 and (f) k=0.1.

the MTF between zero and 1 show the varying degree of contrast preservation relative to the object contrast. In other words, for low spatial frequencies corresponding to large features the contrast is well preserved, whereas higher spatial frequencies corresponding to fine features suffer a loss of contrast. In general, the higher the MTF, the better the preservation of details by the imaging detector and the better the spatial resolution and sharpness of the recorded image.

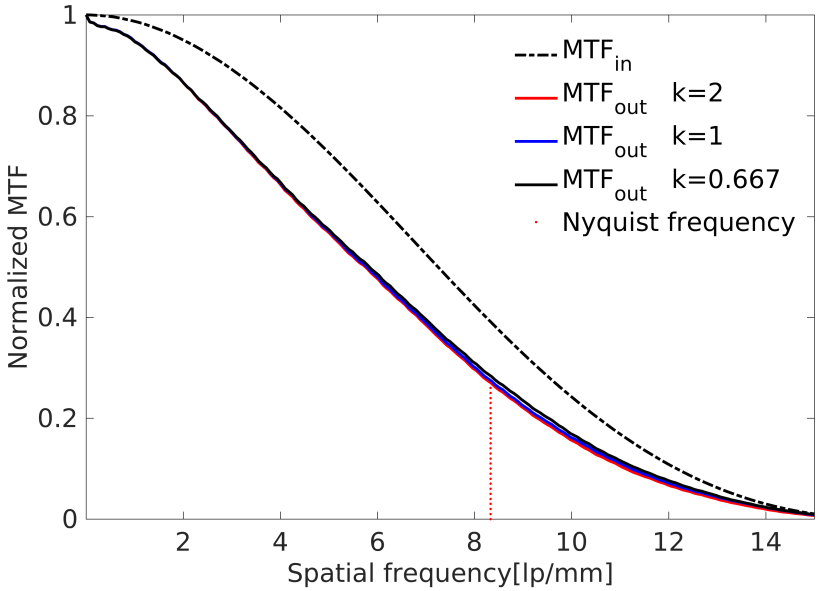

FIGURE 7.18: MTFs at the input and output of the EDET-80 detector operating in integrating mode using high DCD gain settings (k=2, k=1 and k=0.667), which are suitable for low-dose imaging applications.

Higher DCD gain settings (i.e. $k \geqslant 0.667$) can produce high-contrast edge images like the averaged images shown in Figure 7.17(c, d) obtained with low electron dose (0.1 electron per pixel per frame). Therefore, the edge can be well determined and the resulting MTFs are shown in Figure 7.18. These results demonstrate the relevance of the EDET-80 detector in low-electron dose applications (i.e. single electron detection) using high DCD gain settings (i.e. k=2, k=1 and k=0.667).

Instead of recording 1000 frames, each with 0.1 electron per pixel per frame, now the detector is irradiated with 100 electrons per pixel per frame which is similar to a

single-shot experiment. The corresponding MTFs are shown in Figure 7.19. It turns out that low DCD gain settings such as $k \leqslant 0.2$ are suitable for high-electron dose applications (i.e. high dynamic range), but high gain settings fail for high-electron dose applications as the dynamic range of the detector at these gain settings is not suitable to detect all primary electrons. This can clearly be seen in Figure 7.19(a, b).

Figure 7.19(c, d, e, f) demonstrate the suitability of low DCD gain settings, such as $k \leqslant 0.2$, for high-electron dose applications (i.e. high dynamic range). For higher gain settings ($k \geq 0.667$), the recorded edge images shown in Figure 7.19(a, b) are saturated and noisy.

To summarize, the calculation of MTFs demonstrates the capabilities of the EDET-80 detector to carry out low and high-dose imaging experiments by selecting a matching DCD gain setting. For low-electron dose applications with the need of single electron detection only gain settings k=2, k=1 and k=0.667 can be used whereas the gain settings k=0.2, k=0.182, k=0.167, k=0.154 and k=0.1 can be utilized for high-electron dose applications.

The MTF depends on several parameters such as the energy of the primary electrons, exposure time, thickness of the sensor, pixel size and the detector technology (e.g. direct and indirect detection of electrons). Here, the impact of sensor thickness on the detector MTF is investigated. We thinned the silicon sensor of the EDET-80 detector down to 30 µm and irradiated the detector with a low electron dose (i.e. 0.1 electron per pixel per frame) to record frames of a slanted edge, similar to the simulation described in Figure 7.17. Thinning down the silicon sensor of the EDET-80 detector reduces significantly the degrading effect of multiple electron scattering and charge sharing. Consequently, a substantial improvement in the MTF can be achieved, as shown in Figure 7.20.

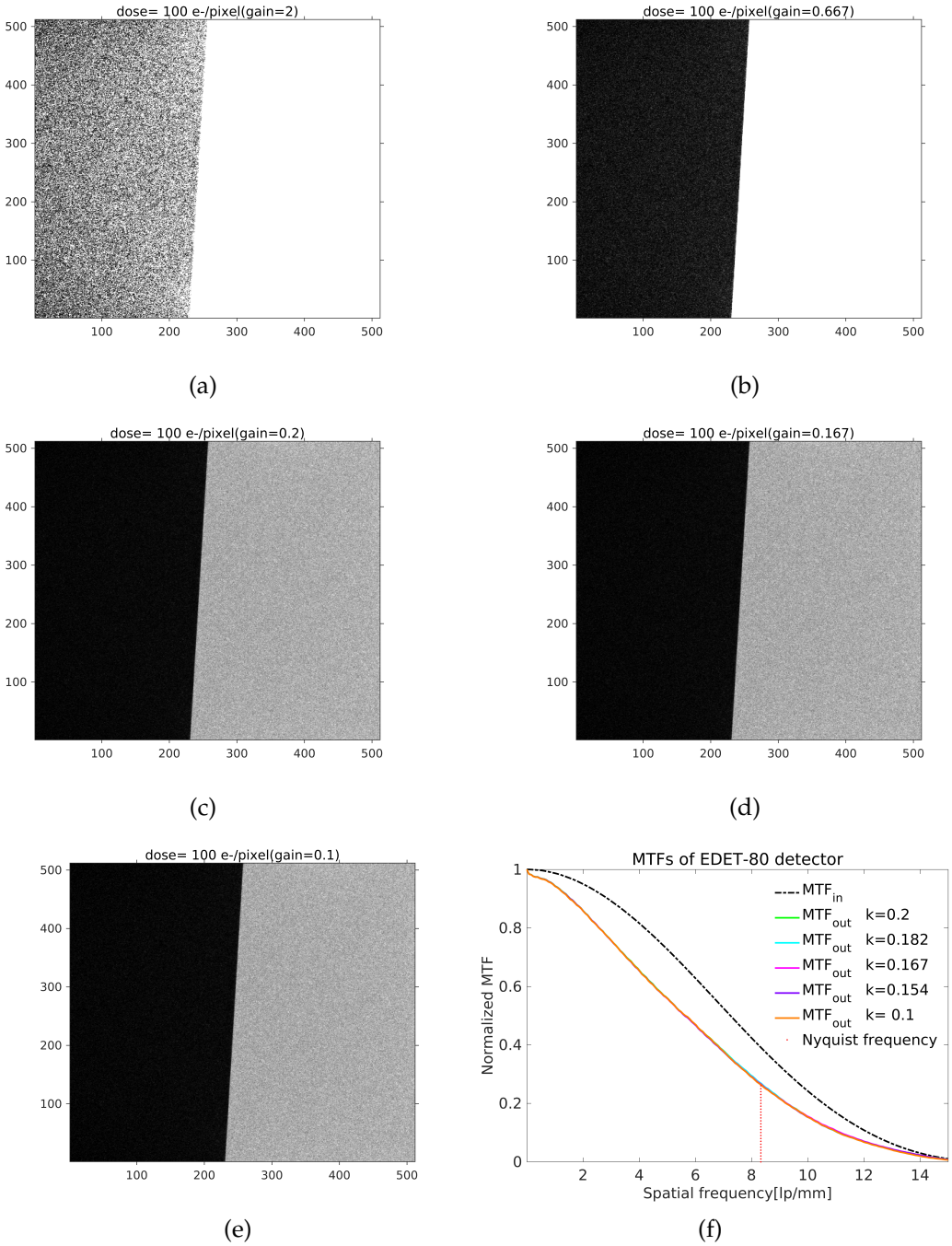

FIGURE 7.19: Output images of the slanted edge at different DCD gain settings and the resulting MTFs. The edge images are obtained with an average flux of 100 electrons per pixel per frame. (a) Image of the edge at gain setting k=2, (b) k=0.667, (c) k=0.2, (d) k=0.167 and (e) k=0.1. (f) MTFs at the input and output of the EDET-80 detector operating in integrating mode with low gain settings ($k \leqslant$0.2).

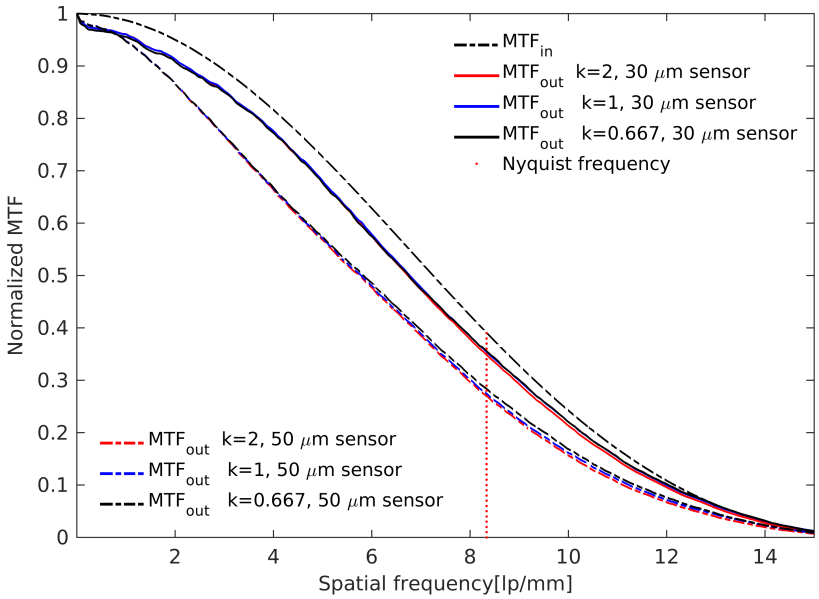

FIGURE 7.20: Comparison of MTFs of two EDET-80 detectors operating in integrating mode with high gain settings (k=2, k=1 and k=0.667). One EDET-80 detector has a 30 µm thick silicon sensor and the second EDET-80 detector has a 50 µm thick silicon sensor.

7.3 DQE of the EDET-80 Detector as a Function of Spatial Frequency

Detective Quantum Efficiency, DQE(f), depends on the spatial frequency and it is therefore directly proportional to the MTF of the detector. DQE(f) is the most widely used quantity for characterizing and comparing the overall imaging performance of detectors because it combines the spatial resolution (i.e. MTF) and the noise performance of the detector, which varies with spatial frequency. Thus, the DQE(f) is more informative than the MTF and can be calculated in the spatial frequency domain by [151, 167]

$$DQE(f) = DQE(0) \times (MTF_{out}(f))^2 . \tag{7.12}$$

This formula assumes that the MTF at the input ($\mathrm{MTF_{in}}$) is equal to 1, meaning that we have an ideal frequency response at the input of the detector. However, for a pixelated detector the $\mathrm{MTF_{in}}$ is not unity for spatial frequencies $\nu > 0$. To take this into account, the $\mathrm{DQE(f)}$ given by equation 7.12 is normalized to the $\mathrm{MTF_{in}}$ by

$$DQE(f) = DQE(0) \times \frac{(MTF_{out}(f))^2}{(MTF_{in}(f))^2}. \tag{7.13}$$

The ratio $(\mathrm{MTF_{out}(f)})^2/(\mathrm{MTF_{in}(f)})^2$ is a function of spatial frequency and thus also the $\mathrm{DQE(f)}$. $\mathrm{DQE}(0)$ is the detective quantum efficiency at zero spatial frequency (i.e. 0 lp/mm) and it describes the fraction of detected electrons contributing to the image. It can be calculated by irradiating the detector with a uniform electron beam to obtain flat field images. The values of $\mathrm{DQE}(0)$ for three scenarios are already calculated in subsections 7.1.1, 7.1.2 and 7.1.3.

The $\mathrm{DQE}(0)$ as a function of the electron dose calculated in subsection 7.1.3 is used in the further calculations that follow as it describes the $\mathrm{DQE}(0)$ of the EDET-80 detector irradiated with very low electron dose and it is calculated from the most practical approach. Inserting $\mathrm{MTF_{in}}$, $\mathrm{MTF_{out}}$ and $\mathrm{DQE}(0)$, which we already calculated, into equation 7.13 gives the DQE as a function of spatial frequency (i.e. $\mathrm{DQE(f)}$). We calculated the $\mathrm{DQE(f)}$ using low and high electron dose and the resulting $\mathrm{DQE(f)}$ are shown in Figure 7.21(a, b) as a function of spatial frequency starting from zero spatial frequency and ending at Nyquist frequency (i.e. $\mathrm{NF} = 1/2\mathrm{d}$). Here, the pixel size is d=60 µm and thus $\mathrm{NF} = 8.333$ lp/mm is the maximum value of the spatial frequency in an image that a detector of 60 µm pixel size can resolve.

The obtained $\mathrm{DQE(f)}$ demonstrates the advanced imaging capabilities of the EDET-80 detector to perform both low and high-dose imaging experiments by selecting a proper DCD gain setting. This finding is consistent with that obtained from

the previous MTF calculation. To compare the $\mathrm{DQE(f)}$ of the EDET-80 detector with film and four commercially available detectors, the spatial frequency was normalized to the Nyquist frequency. Table 7.2 summarizes some features of the EDET-80 detector and three commercially-available direct electron detectors, namely the K2 Summit from Gatan operating in counting mode, the Falcon II from FEI and the DE-20 from Direct Electron both operating in integrating mode. For the comparison in Figure 7.22, a scintillator-based CCD camera, which is an indirect detector was included as well.

The $\mathrm{DQE(f)}$ of these detectors are compared with the $\mathrm{DQE(f)}$ of the EDET-80 detector as presented in Figure 7.22, which shows that all direct electron detectors have a better $\mathrm{DQE(f)}$ than film and CCD camera. It should be noted that the $\mathrm{DQE(f)}$ curve of the K2 Summit is obtained by operating this detector in counting mode resulting thus in an outstanding $\mathrm{DQE(f)}$ but extremely limited frame rate inconsistent with recording fast dynamics, while the $\mathrm{DQE(f)}$ of the EDET-80 detector, the DE-20, the Falcon II and the scintillator-based CCD camera are obtained by operating these detectors in integrating mode, at least for EDET-80 we note that a counting mode is possible, but has not been investigated according to performance yet.

The EDET-80 detector operating in integrating mode offers a higher $\mathrm{DQE(f)}$ than Film, scintillator-based CCD camera and the DE-20 operating over all normalized spatial frequencies. It surpasses the Falcon II operating at fraction of Nyquist frequencies $\nu < 0.31$ and $\nu > 0.82$. The EDET-80 detector outperforms the K2 Summit at fraction of Nyquist frequencies $\nu > 0.73$. In general, the $\mathrm{DQE(f)}$ curves of the EDET-80 highlight the great imaging performance of the EDET-80 detector.

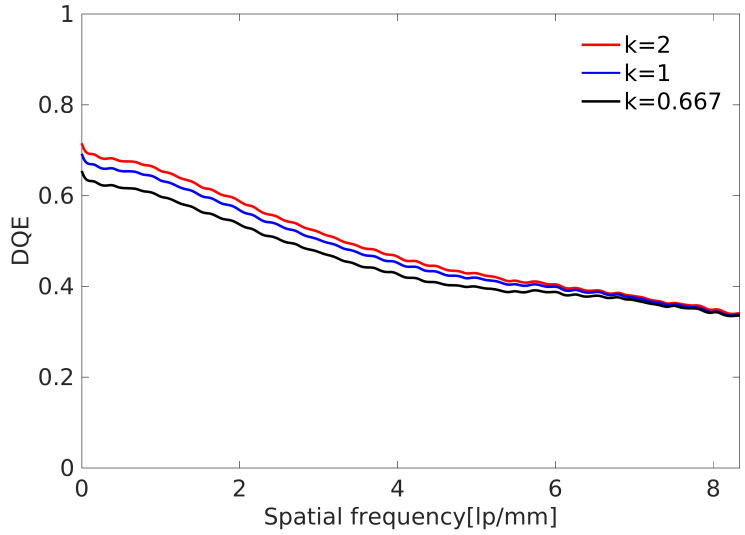

(a)

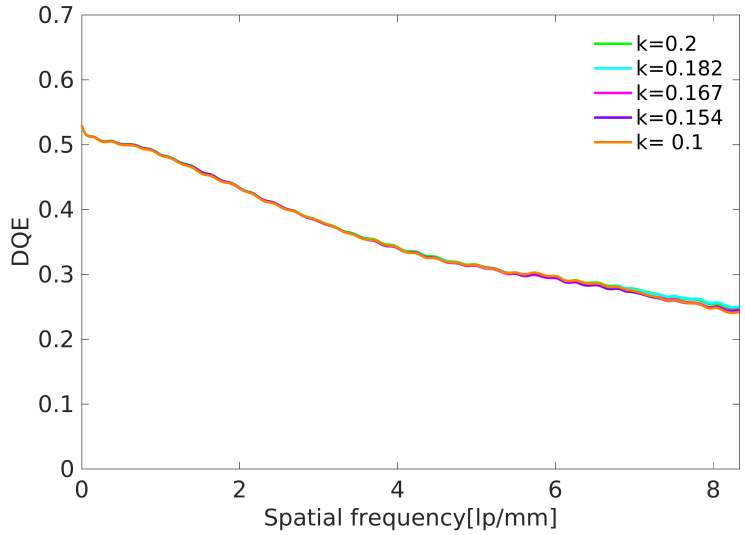

(b)

FIGURE 7.21: DQE(f) as a function of spatial frequency, expressed in lp/mm, of the EDET-80 detector operating in integrating mode. The DQE(f) is plotted from zero to Nyquist frequency. (a) The DQE(f) is obtained by irradiating the EDET-80 detector with a low electron dose (0.1 electron per pixel per frame) and using high DCD gain settings (k=2, k=1 and k=0.667) and (b) the DQE(f) is obtained by irradiating the EDET-80 detector with high electron dose (100 electrons per pixel per frame) and using low gain settings ($k \leqslant$0.2).

TABLE 7.2: Comparison of EDET-80 detector with other three commercial detectors devoted to TEM imaging applications [168]. The object length is the length of the object image on the detector divided by the magnification M. For EDET-80 it is 61.44 mm/50,000 =1.23 µm.

Detector	Falcon II (Integrating mode)	K2 Summit (Counting mode)	DE-20 (Integrating mode)	EDET-80 (Integration mode)
Pixel length (µm)	14	5	6.4	60
Number of pixels	4096×4096	3838×3710	5120×3480	1024×1024
Sensor size (mm)	57.34×57.34	19.19×18.55	32.77×22.27	61.44×61.44
Nyquist resolution (lp/mm)	35.71	100	78.125	8.3333
Å/pixel at M=50,000	2.8	1	1.28	12
Object length (µm) at M=50,000	1.14	0.38	0.65	1.23
Frame rate (fps)	17	400	20-32	80,000

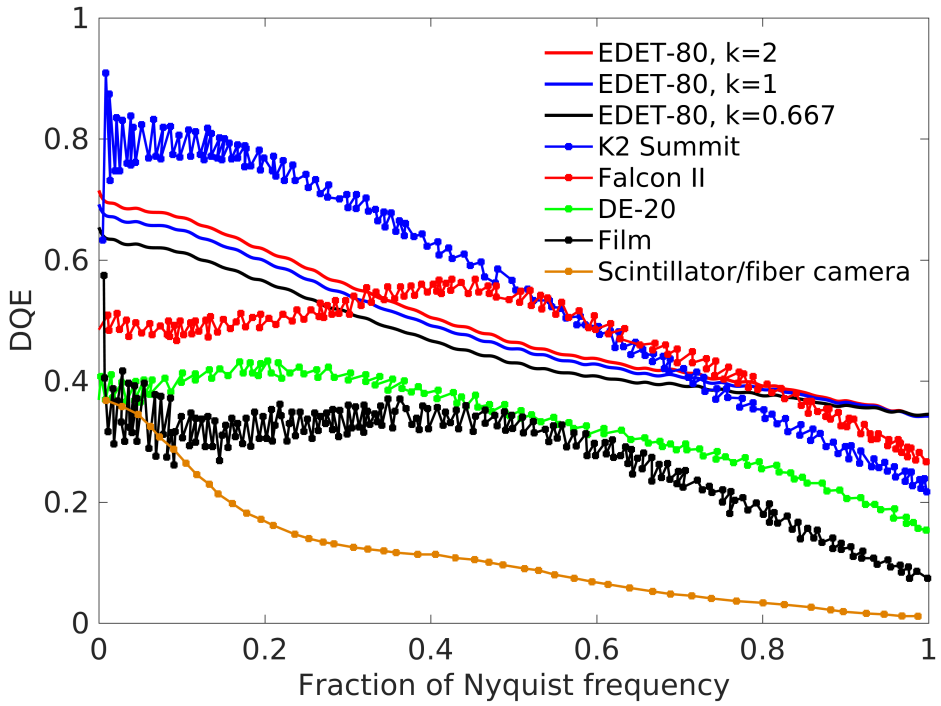

FIGURE 7.22: The DQE(f) curves of the EDET-80 detector operating in integrating mode with DCD gain settings of k=2, k=1 and k=0.667 are compared to the DQE(f) of film, scintillator-based CCD camera and three direct electron detectors (i.e. K2 Summit, Falcon II and DE-20). The DQE(f) values of these detectors are reproduced from [100, 169].

7.4 Spatial Resolution of the EDET-80 in TEM Configuration

The attainable spatial resolution in TEM depends on several factors: These are, for example, TEM objective lens aberrations, properties of the sample (e.g. thickness, materials and dose tolerance), the electron dose applied to this sample as well as detector parameters (e.g. DQE). The spatial resolution is also limited by the TEM imaging mode such as phase contrast or scattering contrast imaging. In order to spatially resolve a sample of a given size, a sufficient amount of scattering events from this sample is needed. Beam-sensitive samples must be imaged with relatively

low electron dose and data recording is limited by the onset of radiation damage. Most biological samples can only tolerate an electron dose of 0.0625–0.625 $e^-/\text{Å}^2$ before significant radiation damage occurs [129].

It is interesting to note that the achievable spatial resolution in TEM liquid samples, especially in biological and organic samples, is mainly limited by the electron dose applied to the sample [59]. Thus, it is beneficial to investigate the dose-limited spatial resolution given by the following formula [133]

$$\delta = SNR(DQE)^{\frac{-1}{2}} C^{-1}(FD)^{\frac{-1}{2}}. \tag{7.14}$$

Where SNR must equal at least 3–5 to distinguish image features, according to the Rose-criterion [170], C is the contrast, D is the electron dose per unit area of the sample and F is the fraction of electrons reaching the detector. δ represents the achievable dose-limited resolution measured at the sample. This equation states that a feature of contrast C can only be detected if its size exceeds δ. In general, the spatial resolution can be improved by increasing the electron dose and imaging high contrast objects with a high DQE detector. Nevertheless, the electron dose needed, at a given frame rate, to reach the desired spatial resolution depends on the available brightness of the electron source. The brightness B is a key electron beam parameter and it is the current density J per solid angle Ω of the electron source. It is determined by the accelerating voltage V and the reduced brightness B_r by the following equation [64]

$$\begin{aligned} B_r &= \frac{B}{V} \\ &= \frac{\mathrm{d}J}{\mathrm{d}\Omega V}. \end{aligned} \tag{7.15}$$

Where $\mathrm{d}J$ is the infinitesimal current density element and $\mathrm{d}\Omega$ is the corresponding solid angle. For very small angles $\mathrm{d}\Omega = 2\pi(1 - \cos\alpha) \simeq \pi\alpha^2$ and α is related to the wavelength and the transverse coherence length of the electrons $L_{c,t}$ as follows [64]

$$L_{c,t} = \frac{\lambda}{2\alpha}. \tag{7.16}$$

Using De Broglie's formula and the reduced Planck's constant, $\hbar = h/2\pi$, we obtain the following non-relativistic wavelength

$$\lambda = \frac{2\pi\hbar}{\sqrt{2meV}}. \tag{7.17}$$

The current I is related to the current density J by the following formula

$$J = \frac{I}{\pi\sigma_s^2}. \tag{7.18}$$

With σ_s is the sample spot size and J depends on the brightness B. From now on we use $L_{c,s}$ instead of $L_{c,t}$ to refer to the sample. Combining the equations 7.15- 7.18 gives the final formula of B_r

$$B_r = \frac{2meJL_{c,s}^2}{\pi^3\hbar^2} \tag{7.19}$$

The reduced brightness B_r is expressed in $\mathrm{A.m^{-2}.Sr^{-1}.V^{-1}}$ and it is clear from this equation that J and $L_{c,s}$ are limited by the brightness B_r.

We have so far demonstrated that the spatial resolution of the detector depends on the electron dose applied to the sample, which is in turn related to the available brightness of the electron source. Now, we move on to quantify the required current to achieve a given electron dose. In order to perform the calculation of the current and consequently the achievable spatial resolution, it is necessary to have realistic values of the brightness of some electron sources. These are listed in Table 7.3 for three different electron sources [63].

TABLE 7.3: Some features of three electron sources used in TEM [63]. B_r is calculated here at an accelerating voltage V =200 kV.

Types of electron source	LaB_6 thermionic	Schottky emission	Cold field emssion
Material	LaB_6	ZrO/W	W
$B(\mathrm{A.m^{-2}.Sr^{-1}})$	$\simeq 10^{10}$	$\simeq 10^{11}$	$\simeq 10^{12}$
$B_r(\mathrm{A.m^{-2}.Sr^{-1}.V^{-1}})$	$\simeq 5\times 10^{7}$	$\simeq 5\times 10^{8}$	$\simeq 5\times 10^{9}$

In the following we estimate the achievable spatial resolution of the EDET-80 versus the electron dose applied to the sample. As an example, let us investigate the dose-limited spatial resolution when irradiating gold nanoparticles within a thin liquid cell with an increasing electron dose. This can be one of the useful experiments, which we can carry out to explore not only the spatial resolution of the EDET-80 as a function of electron dose but also its capability to capture the dynamics of these nanoparticles (e.g. Brownian motion). For objects consisting of high-atomic number materials like gold nanoparticles, we can use high electron dose (e.g. D=100 $e^-/\mathrm{\AA}^2$) [171] and even higher dose has been reported in liquid at

200 keV [171]. Furthermore, we assume a contrast C=0.10 [59], F=0.8 and SNR=3 fulfilling the Rose-criterion [170].

Taking into account the 80 kHz frame rate of EDET-80 detector, the brightness delivered by $\mathrm{LaB_6}$, the values of σ_s and $L_{c,s}$, as shown in Table 7.4, we can estimate the required current I and consequently the dose D using equation 7.18 and equation 7.19. Inserting the values of C, D, SNR, F and DQE of 0.40 at Nyquist spatial frequency in the equation 7.14 gives the achievable spatial resolution δ. It should be noted that the equation 7.14 does not consider the Nyquist sampling theorem. Therefore, for optimal sampling satisfying the Nyquist criterion the achievable resolution becomes $s = 2\delta$. For other sources, Schottky and cold FE, the magnification M must be optimized to deliver the same electron dose per pixel per frame. The obtained results are listed in Table 7.4.

TABLE 7.4: Calculated values of the dose-limited spatial resolution s of the EDET-80 when operating in a 200 keV TEM equipped with different electron sources. D_d is the electron dose per pixel per frame at the detector and D is the electron dose per $\mathrm{\AA}^2$ per frame at the sample. Note that the highest brightness is delivered by the Cold FE source. The brightness values of these three electron sources are taken from [63].

B_r	σ_s	$L_{c,s}$	I	D	D_d	M	s
$(\mathrm{A.m^{-2}.Sr^{-1}.V^{-1}})$	(nm)	(nm)	(nA)	$(\mathrm{e^-/\AA^2})$	$(\mathrm{e^-/pixel})$	$\times 10^4$	(nm)
$\mathrm{LaB_6} : 5 \times 10^7$	100	15	0.83	0.2	81	3	23.5
$\mathrm{Schottky} : 5 \times 10^8$	100	15	8.3	2.0	81	9.5	7.4
$\mathrm{Cold\,FE} : 5 \times 10^9$	100	15	83	20	81	30	2.3

It is clear from these calculations that the larger the brightness value, the higher the dose per frame and thus the better the achievable spatial resolution. However,

a higher electron dose may raise concerns about the charge handling capacity of the detector and the radiation damage of beam-sensitive samples. Fortunately, electron dose may be optimized depending on the intended experiment. For example, in the cryogenic TEM an electron dose of 5 to 20 $e^-/\text{Å}^2$ can be tolerarted by macromolecular complexes [172] and can be increased to 50 and 200 $e^-/\text{Å}^2$ for whole cells depending on the desired spatial resolution [173]. As indicated previously, nanoparticles like gold can withstand high electron dose (e.g. 100 $e^-/\text{Å}^2$). Hence, based on the calculations summarized in Table 7.4 we can make a movie of 50 frames where each frame is recorded with an electron dose of 2 $e^-/\text{Å}^2$ and a spatial resolution of 7.4 nm.

In these calculations, the investigated sample (i.e. gold nanoparticles) can withstand even higher dose than this used here. In addition, the pixels of the EDET-80 detector can handle about 200 primary electrons of 200 keV per pixel per frame, as we have already discussed in section 6.2. Interestingly, these results highlight that the EDET-80 detector can achieve a spatial resolution at nanometer scale even with a LaB_6 thermionic source. We can further improve the resolution by optimizing some instrument parameters. For instance, using a cold FE source, $L_{c,s}$ =5 nm, σ_s =30 nm and $M = 6 \times 10^5$ results in I = 68 nA, D =182 $e^-/\text{Å}^2$, D_d =182 e^- per pixel per frame. These values lead to an enhanced spatial resolution of s =0.78 nm.

As already mentioned, biological samples are very sensitive to relatively small electron doses. For instance, it was found that for pristine biological material the structural damage starts to happen at an electron dose of 1 $e^-/\text{Å}^2$ [174]. As an example, we consider a biological sample with C =0.05 [59] and we use $L_{c,s}$ =5 nm and σ_s =30. Hence, the resulting spatial resolutions at D =1 $e^-/\text{Å}^2$ gets s =21 nm.

Based on these results, we make the following conclusions: The detective quantum efficiency and the electron dose tolerated by the sample being imaged are the

fundamental factors limiting the achievable spatial resolution of detectors. When higher dose is tolerated by the sample, the charge handling capacity of the pixel may limit the spatial resolution. Fortunately, the charge handling capacity of the EDET-80 pixels is large enough to handle a high electron dose, as described in section 6.2. Furthermore, the pixel area of the EDET-80 is sufficient to achieve nanometer resolution and even sub-nanometer resolution can be attainable when imaging samples that can withstand a high electron dose—material science and cryo-EM. Thus, to reach the highest possible spatial resolution, an optimal electron dose must be determined taking into account the experimental conditions.

Chapter 8

Radiation Hardness and Shielding of the EDET-80 Detector

Ionizing radiation damages the oxide (SiO_2) layer covering the silicon sensor, which has direct impact on the operating characteristics of the DEPFET. Thereby reducing the charge collection efficiency and increase the noise in the detector. In addition, radiation damage shortens the lifetime of detectors, especially in direct electron detectors due to the large amount of charge created in the detector layers as a result of inelastic scattering events. It can be classified into two main types, namely non-ionizing radiation damage and ionizing radiation damage.

8.1 Non-ionizing Radiation Damage

Silicon bulk damage in semiconductor detectors is produced by the non-ionizing energy loss (NIEL) interactions of electrons with the silicon atoms. If the energy transferred to the lattice silicon atoms is sufficient to remove them from their original lattice sites, displacement damage takes place. The minimum recoil energy and electron kinetic energy required to produce this displacement are 25 eV [175, 176] and 250-260 keV [177], respectively. If the recoil energy is much larger than the

threshold recoil energy (i.e. 25 eV), an avalanche of displacements of silicon atoms will occur, leading to clusters of defects. However, this requires a minimum kinetic energy of about 8 MeV [176]. Therefore, only silicon bulk damage arising from single displacements of silicon atoms in the EDET-80 detector can be expected as the electron energy used in TEM experiments (i.e. 300 keV) is far below the minimum energy required (i.e. 8 MeV) to produce clusters of defects. It is therefore advisable to operate the detector with electron energies below the 250 keV threshold since the displacement damage can be entirely prevented. The resulting defects in the lattice of silicon bulk can alter the electrical properties of the DEPFET sensor due to additional states created in the band gap of the silicon and change of doping characteristics [178]. According to previous radiation hardness studies for DEPFETs in Belle II, the bulk radiation damage is small compared to that of the silicon dioxide layer of the DEPFETs [179].

8.2 Ionizing Radiation Damage

Incident electrons deposit their energy in the detector layers, ionizing the atoms and thereby creating e-h pairs. This depends on the layer material, thickness and the energy of the interacting electrons. This process is essential in the DEPFET silicon bulk as it leads to the detection of the incident particles, but the e-h pairs generated in the silicon dioxide (SiO_2) insulator layer covering the silicon sensor are responsible for the radiation damage effects encountered in semiconductor detectors.

The EDET-80 detector has a silicon dioxide layer of 100 nm thickness covering a 50 µm thick silicon sensor, as illustrated in Figure 8.1. Electrons and holes created in the SiO_2 layer have a mobility of $\mu_e^{SiO_2}$=20 cm^2/Vs and $\mu_h^{SiO_2}$=$10^{-6}cm^2/Vs$, respectively [180]. Hence, electrons are removed quickly from the SiO_2 layer by a positive voltage applied to the pixel gate during the charge collection whereas

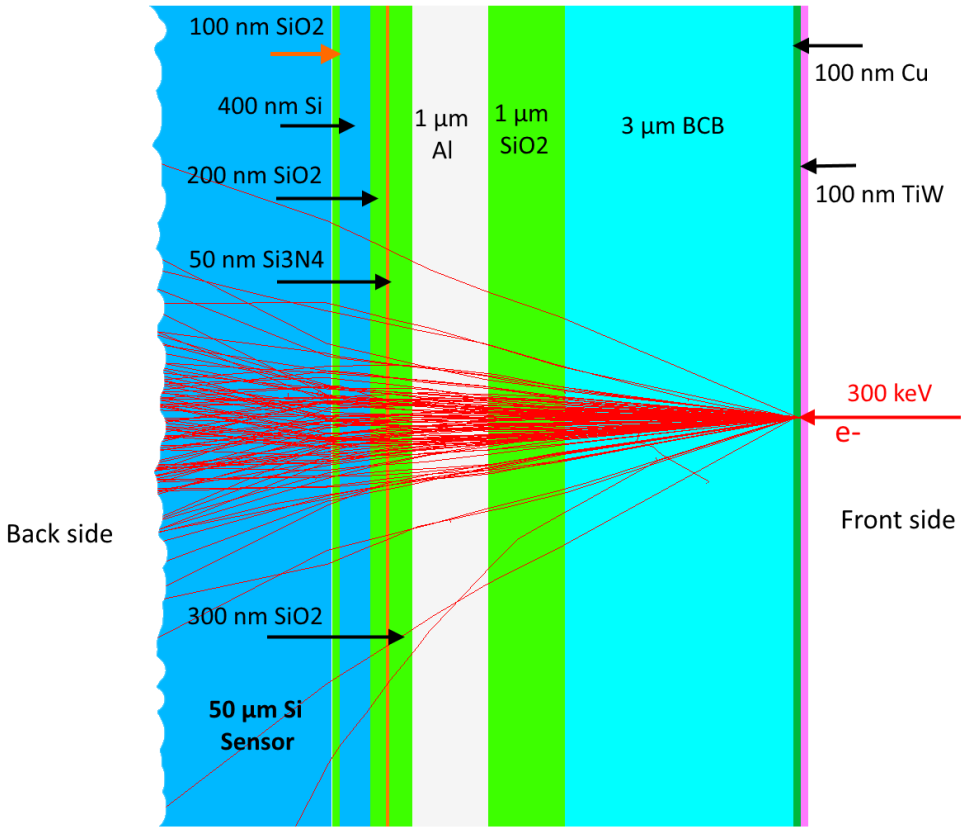

FIGURE 8.1: A schematic view of the entrance layers of the EDET-80 detector irradiated with 100 electrons of 300 keV from the front side.

holes move very slowly toward the SiO_2-Si interface where they recombine with electrons. In addition, a fraction of these holes can be trapped at the SiO_2-Si interface, thus leading to a charge build-up [178]. The trapped positive charge of the holes in the oxide layer shifts the threshold voltage of the DEPFET towards more negative values, which can degrade the charge collection efficiency and thus the detector performance.

We calculated the radiation dose in the entrance layers shown in Figure 8.1 by irradiating the EDET-80 detector with a uniform electron beam of 300 keV from the front side to reduce the effects of radiation damage. The irradiation of the detector with 300 keV electrons from the back side leads first to the energy deposition in the

50 µm thick silicon sensor. After that, these electrons reach the 100 nm thick SiO_2 layer with a mean energy of about 270 keV, as discussed in section 5.3. Thus, more charges inducing radiation damage can be produced in the SiO_2 layer as low energy electrons produces more charges than higher energy electrons (see Figure 5.4).

According to the simulation results shown in 8.2(a), one primary electron of 300 keV creates a radiation dose of 1.108 mrad per pixel per frame in the silicon dioxide layer (SiO_2) of the EDET-80 detector. In the simulation, all layers are pixelated into 512×512 pixels and the pixel size is 60×60 µm^2. Consequently, 10 and 100 electrons per pixel per frame create radiation doses up to 11.08 mrad and 110.8 mrad per pixel per frame, respectively. Taking into account a radiation tolerance of 8 Mrad, the EDET-80 can capture and 72.2 million frames irradiated with 100 electrons per pixel per frame. In other words, the EDET-80 can make 7.22×10^5 movies of 100 frames.

Radiation damage depends on the energy of the electrons. Low energy electrons deposit more energy in the detector than those with higher energy, thus causing more radiation damage. For instance, the irradiation of the detector with 100 keV electrons increases the radiation dose in the 100 nm thick SiO_2 layer by a factor of 3.5 compared to 300 keV electrons, as shown in Figure 8.2(b). Therefore, it is advisable to perform experiments with high energy electrons (e.g. 300 keV).

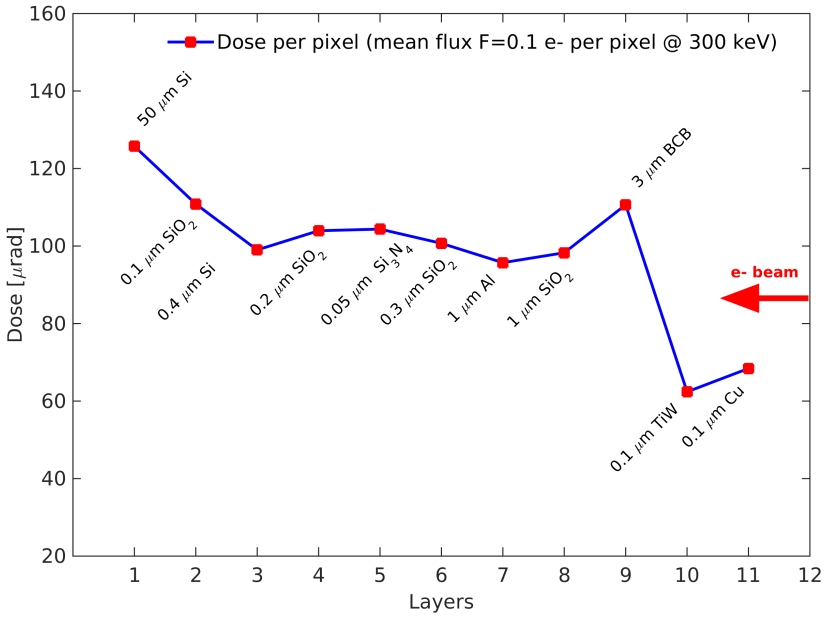

(a)

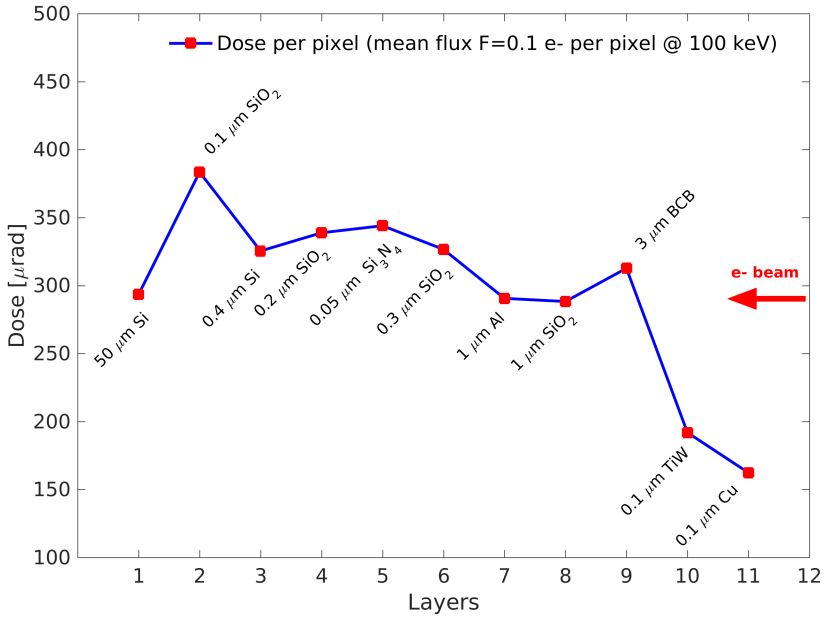

(b)

FIGURE 8.2: Mean ionizing radiation dose per pixel in the different layers of the EDET-80 detector irradiated with a flux of 0.1 electron per pixel. (a) EDET-80 is irradiated with 300 keV electrons and (b) EDET-80 is irradiated with 100 keV electrons.

8.3 EDET-80 Detector Shielding

The readout electronics (e.g. switchers and DCDs) of the EDET-80 detector are integrated close to the sensitive area (see Figure 8.3) and suffer radiation damage when exposed to radiation. Therefore, an efficient shielding has to be designed and optimized to protect the readout electronics of the detector against possible radiation damage from the electron beam. Shielding from the primary electrons can be achieved by placing a material of sufficient thickness in front of the detector readout electronics (ASICs) to completely absorb the incident electrons. However, electrons of several hundred keV interacting with a thick shielding layer produce X-rays, which in turn can damage the ASICs. To investigate the significance of the shielding material, several simulation studies were performed. The simulation setup illustrated in Figure 8.3 shows our approach to investigate the shielding capability of some materials.

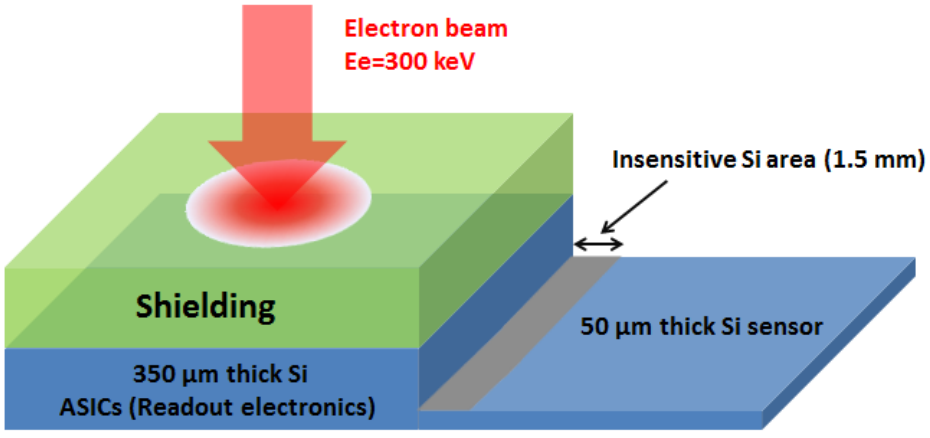

FIGURE 8.3: Illustration of the simulation setup used to investigate the shielding of the readout electronics of the EDET-80 detector.

The setup consists of a 50 µm thick silicon sensor, another 350 µm thick silicon

layer representing the ASICs covered by a shielding material being investigated. In the first step, we shield the readout electronics using materials of low atomic numbers (e.g. Aluminum), high atomic numbers (e.g. Titanium and Tantalum) and a sandwich of low and high-atomic number materials. Then, the detector is exposed to an electron beam of 300 keV to calculate the energy deposition in the ASICs and the spectra of X-rays entering and exciting the ASICs.

Figure 8.4 shows that the optimized shielding would be a sandwich shielding consisting of a 1 mm thick tantalum layer covered by a 0.5 mm aluminum layer. The first aluminum layer acts as an electron absorber as the range of 300 keV electrons in the aluminum is about 402 µm. The generation of X-rays depends on the atomic number of the shielding material. Thus, it is efficient to stop, in the first step, the energetic electrons in the aluminum layer, which has the advantage of generating less X-rays than in high-atomic number materials. In the second step, a 1 mm thick tantalum layer acts as an absorber of the X-rays generated in the aluminum layer and emitted towards the ASICs. As a consequence, the irradiation of the shielded area with 10 million electrons of 300 keV results in an energy deposition of 380 keV in the ASICs, which is equivalent to the energy of 1.26 primary electrons of 300 keV. An alternative to layered materials would be a 1 mm thick tantalum layer which can perform both tasks, namely the absorption of electrons and X-rays. The range of 300 keV electrons in tantalum is 97 µm and it can thus stops almost all the electrons in the first 100 µm depth and the remaining 900 µm thickness acts as an X-ray self-absorber. As a result, the energy deposition in the ASICs is 7886 keV, that is equivalent to about 26 primary electrons of 300 keV.

The energy deposition in the silicon ASICs is due to the interaction of X-rays passing through this layer. The spectra of the X-rays entering and leaving the ASICs layer are shown in Figure 8.5. The obtained spectra demonstrate that most of the

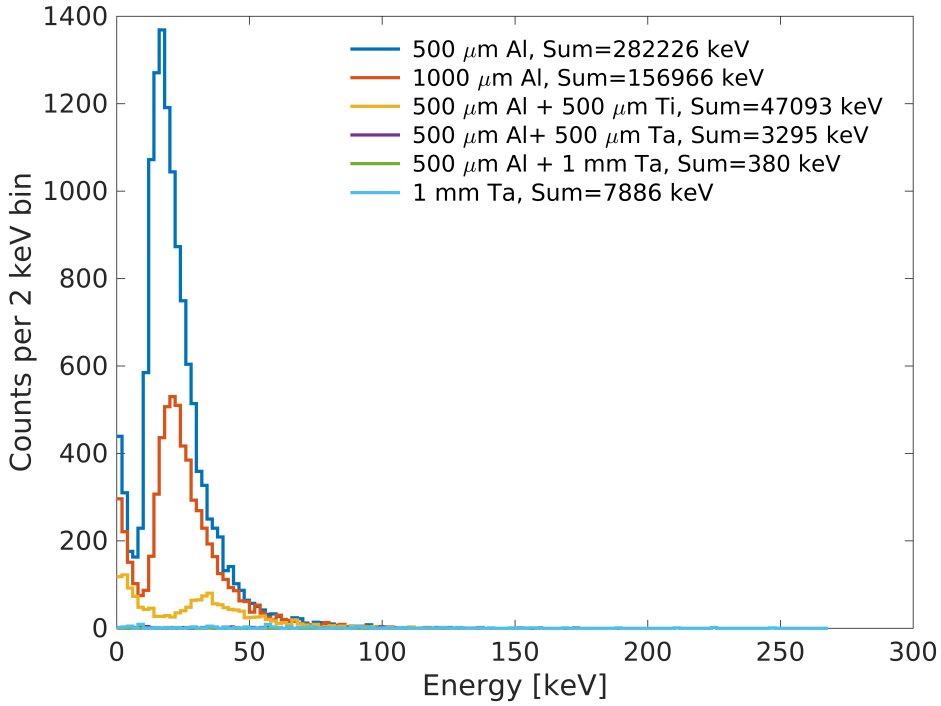

FIGURE 8.4: Spectra of the energy deposition in the readout electronics. Sum is the total energy deposited by 10 million electrons hitting the shielding layers.

X-rays generated in the shielding pass though the ASICs and only a small fraction is absorbed. Basically, a thick shielding can perfectly shield the electronics, but at the expense of the quality of the signal detected in the sensor since a significant fraction of electrons can scatter from the edge of a thick shielding producing thus an additional signal in the detector. This effect is shown in Figure 8.6 and it is similar to the impact of backscattered electrons on the detector performance, which we discussed in chapter 5 and chapter 6. We simulated the impact of the electrons scattered from the shielding edge on the detector performance by irradiating the whole edge area with a planar electron beam. The total edge area is 12 mm$\times$1.85 mm is irradiated with 9.3425 million electrons, which corresponds to 0.42 electron per µm^2. The simulation setup shown in Figure 8.6(a) represents the worst case scenario to investigate the shielding edge effect on the signal created in the sensor.

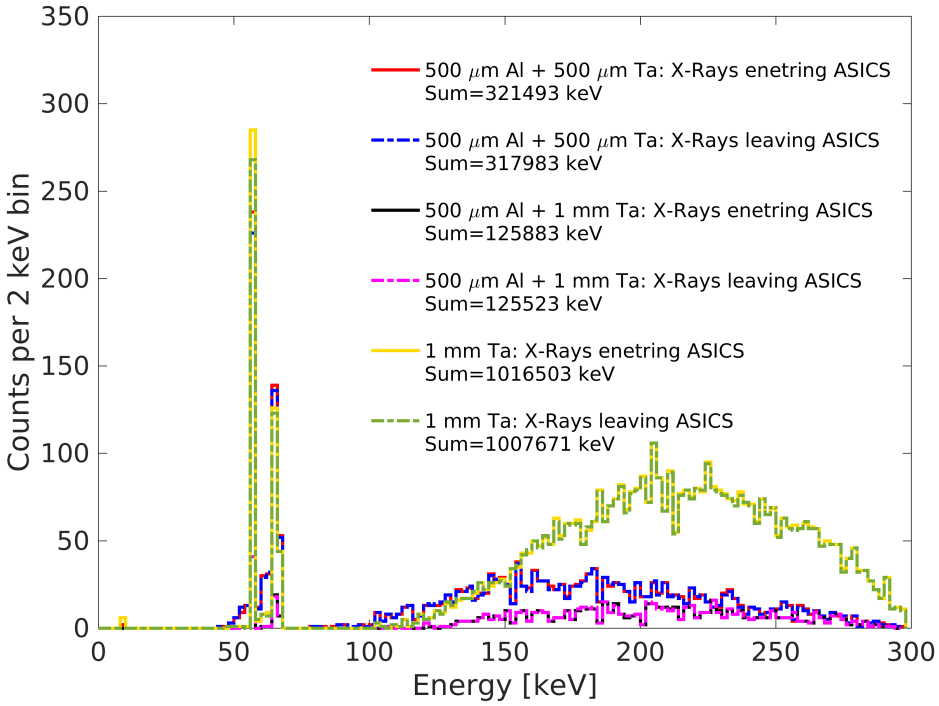

FIGURE 8.5: Spectra of X-rays entering and leaving the ASICs using different shielding configurations.

The mean profile presented in Figure 8.6(c) shows that the shielding adds a significant amount of background (i.e. noise) to the total signal detected in the sensor. The maximum background is detected by the pixels closest to the shielding edge and it is $\sim$34% of the total signal. The investigated shielding design is not optimal due to the background created in the sensor. Furthermore, a possible mechanical damage can be expected as the shielding layer is positioned directly on the top of the layer containing the ASICs. Therefore, a further optimization of the shielding is necessary.

The possible mechanical damage can be avoided by introducing a 1 mm gap between the shielding and the ASICs. To minimize the background, the edge of the shielding is now inclined which has the advantage of reducing the amount of electrons scattered towards the sensor. To investigate the energy deposition as a function of depth in the ASIC layer, the 350 µm thick ASIC layer has been sliced

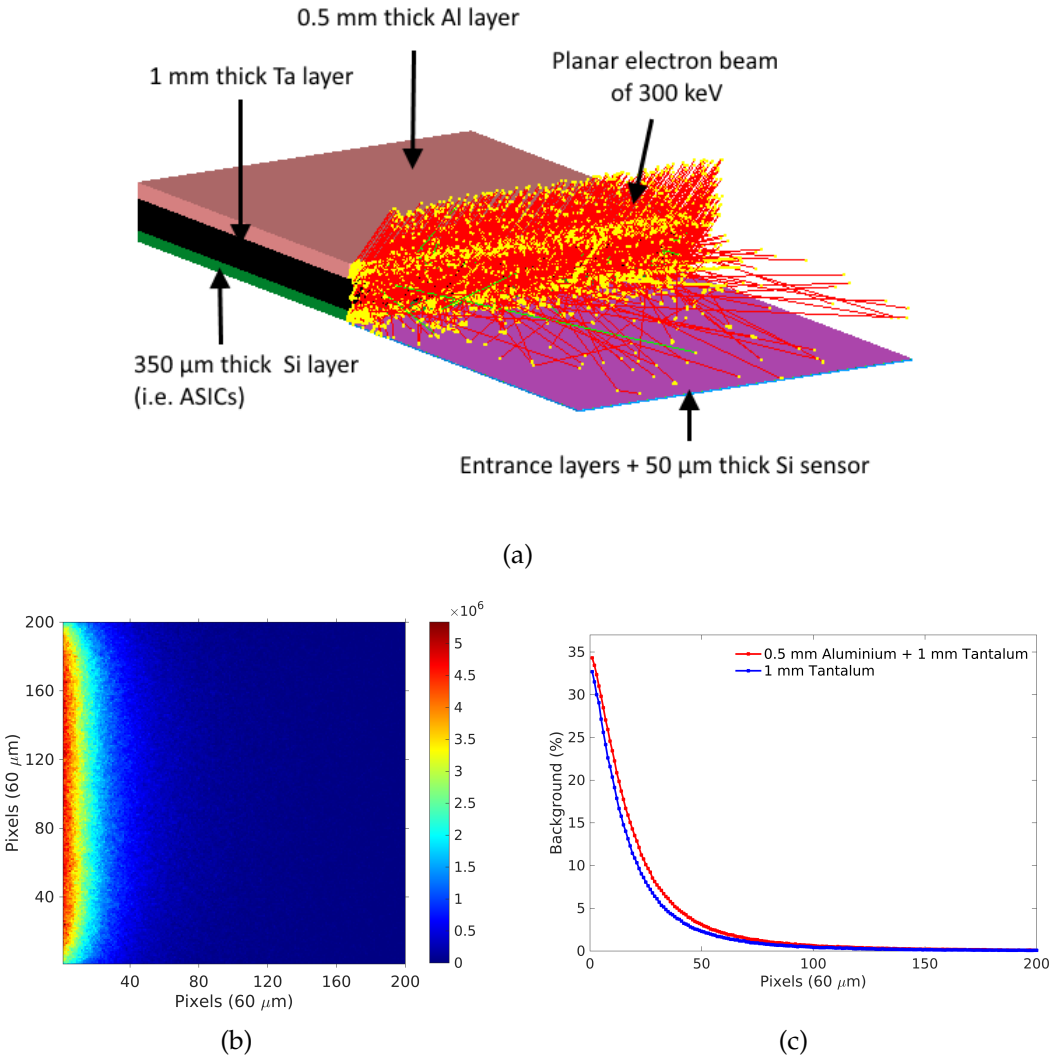

FIGURE 8.6: Simulation of the electrons scattered from the shielding edge towards the sensor. (a) Simulation setup to investigate the effect of electrons scattered from the shielding edge on the signal created in the silicon sensor. The sensitive layer is pixelated into 200 by 200 pixels of 60 µm size and only 1000 events are shown. (b) Distribution of the signal (i.e. e-h pairs) created in the sensor by electrons scattered from the shielding edge and (c) mean profile along the edge direction obtained from (b) and normalized to the signal created by a primary electron of 300 keV hitting directly the sensor.

into three sub-layers, namely a 110 µm thick top layer, a 120 µm thick middle layer and 120 µm thick bottom layer. Now, a 1 mm thick tantalum shielding with an inclined edge is used and the whole simulation setup is irradiated with a uniform cone-shaped electron beam of 300 keV, as shown in Figure 8.7.

The dark strip shown in Figure 8.7(b) is due to the shift of the tantalum layer by 0.5 mm towards the sensor and thus some pixels are also shielded ($\sim$8 pixels). This shift is needed to shield the edge of the silicon layer containing the ASICs. The mean profile along the edge direction depicted in Figure 8.7(c) demonstrates that this shielding design minimizes the fraction of electrons scattered from the shielding edge. However, further investigation is still required—the distribution of the energy deposition as a function of depth in the ASIC layer. This can give useful information about the optimal location for the integration of the readout electronics. From the simulation setup illustrated in Figure 8.7 we obtain the distribution of the energy deposition in each sub-layer of the ASIC, as shown in Figure 8.8. As can be seen from these results, 75.6% of the total energy deposited in the ASIC is absorbed in the top layer, 19.3% in the middle layer and 5.1% in the bottom layer.

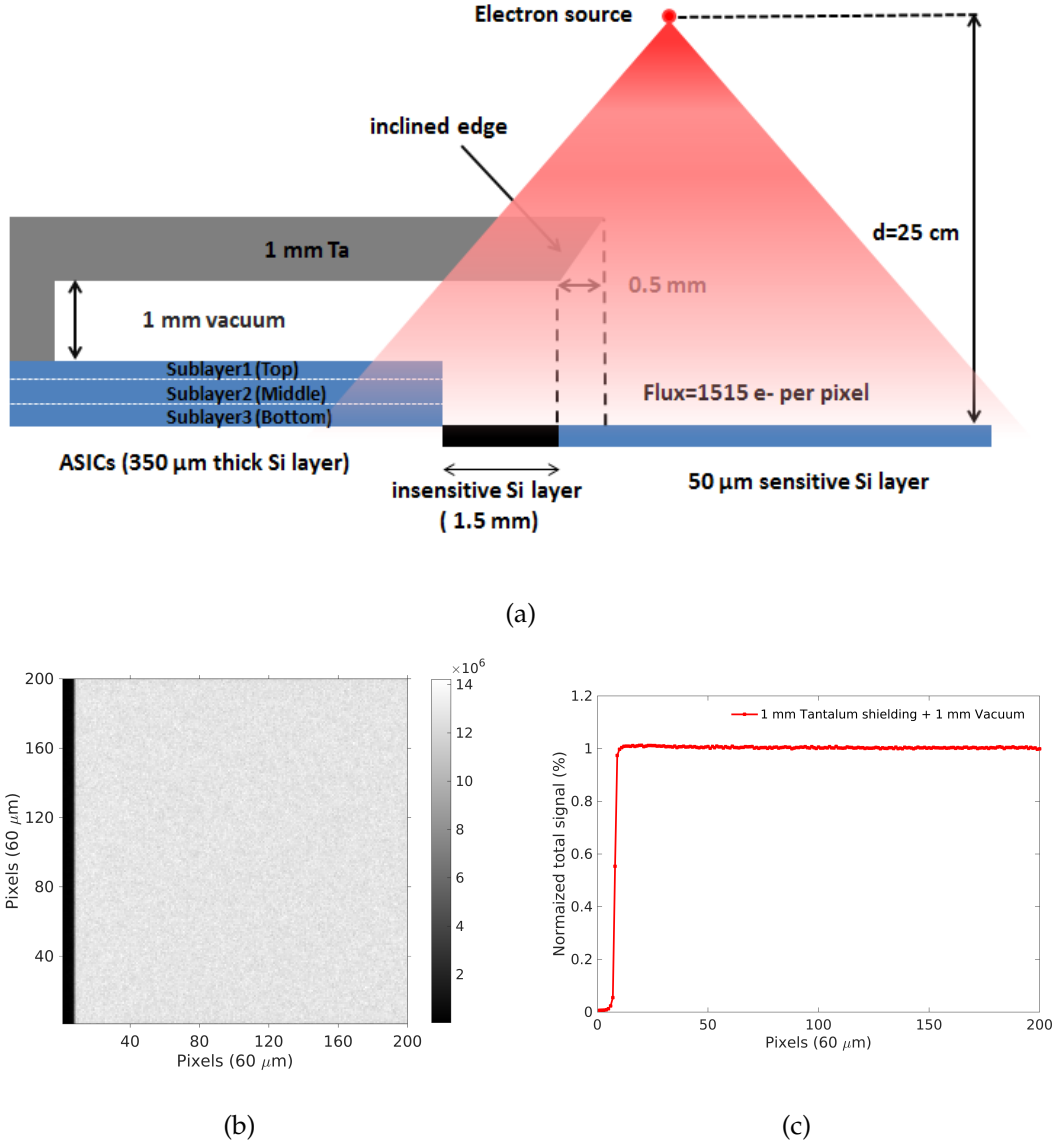

FIGURE 8.7: Illustration of the optimized design to shield the readout electronics of the EDTE-80 detector. (a) Simulation setup used to investigate the effect of electrons scattered from the inclined edge of the shielding layer on the total signal created in the silicon sensor. The dimensions are not to scale. (b) Distribution of the total signal (e-h pairs) created in the sensor by electrons scattered from the shielding edge and electrons hitting directly the sensor. (c) Mean profile obtained from (b) and normalized to the signal created by primary electrons of 300 keV hitting directly the sensor.

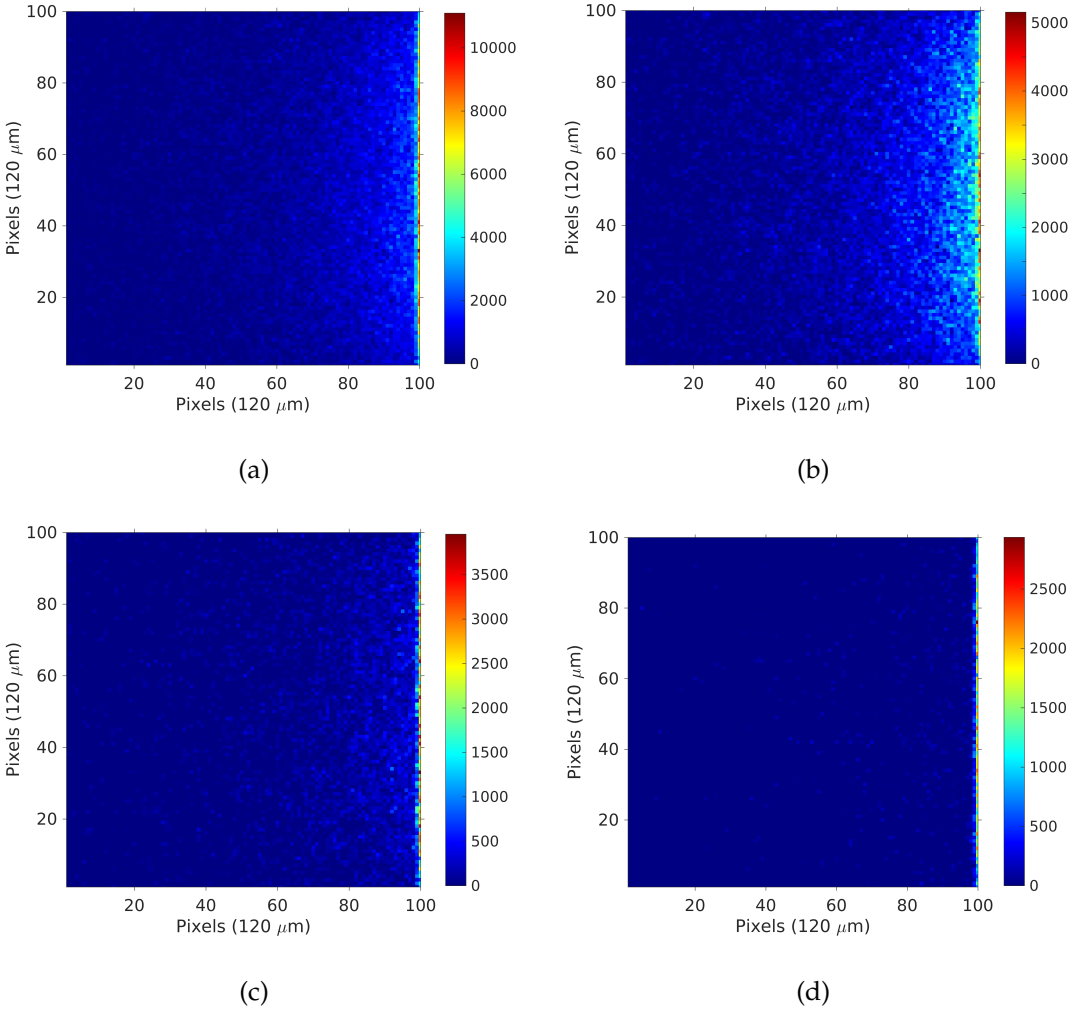

FIGURE 8.8: Distribution of the energy deposition in keV in each sub-layer of the ASIC layer. The sub-layers are pixelated into 100 by 100 pixels and the pixel size is 120×120 µm^2. (a) Distribution of the energy deposition in all layers. The total energy deposition is ΔE_{tot}=4323.461 MeV. (b) Distribution of the energy deposition in the 110 µm thick top sub-layer. The energy deposition is ΔE_{tot}=3267.786 MeV. That means that 75.6% of the total energy is deposited in the top layer. (c) Distribution of the energy deposition in the 120 µm thick middle sub-layer. The energy deposition is ΔE_{tot}=833.536 MeV, which corresponds to 19.3% of the total energy deposition. (d) Distribution of the energy deposition in the 120 µm thick bottom sub-layer. The energy deposition is ΔE_{tot}=222.140 MeV, which corresponds to 5.1% of the total energy deposition.

According to these simulation studies, the shielding of the electronics integrated in the EDET-80 detector system can be achieved utilizing a sandwich structure with inclined edge consisting of low-atomic number materials such as aluminum to stop the electron beam and dense materials like tantalum to absorb the X-rays generated in the aluminum. Another feasible shielding strategy would be a 1 mm thick tantalum layer with inclined edge, which acts as electron and X-ray absorber.

Figure 8.9 shows a top view of the EDET-80 detector with shielding constructed based on the simulation investigations.

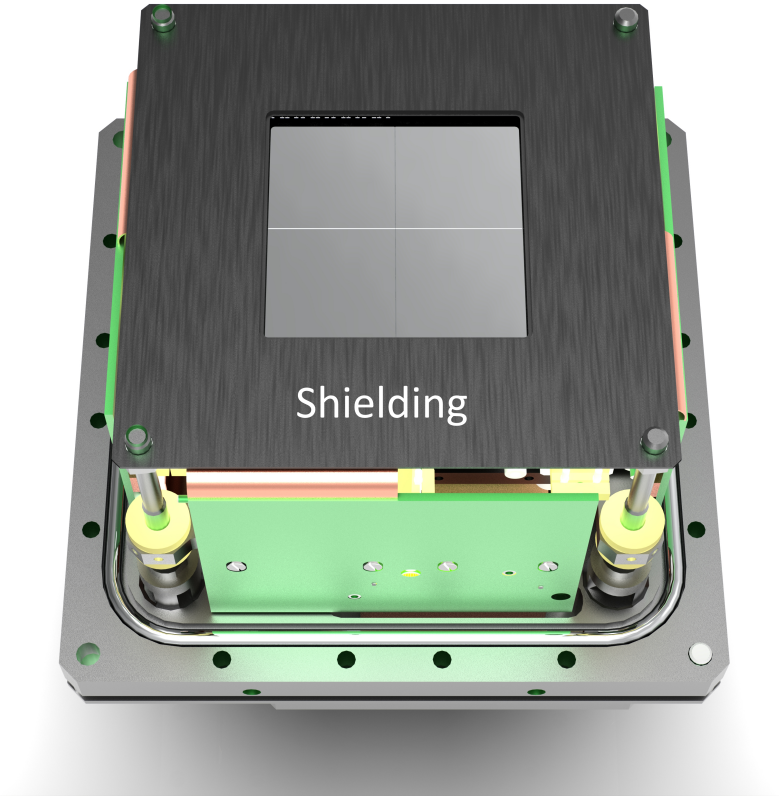

FIGURE 8.9: EDET-80 detector shielded with 1 mm thick tantalum layer.

Chapter 9

Measurements with First EDET-80 Prototype

As a consequence of the combined work by HLL, KIT and MPSD we have developed a prototype of the EDET-80 detector consisting of 128 by 64 pixels and we carried out the first measurements with this prototype using a photon source. The central function of this prototype is to verify the detector performance and find solutions for possible challenges.

To investigate the performance of the EDET-80 detector, we performed measurements at the HLL in Munich with an EDET-80 prototype. We irradiated this detector prototype with Cadmium 109 (Cd-109) radioactive source, which emits X-ray photons of an energy ranging from about 2.6 keV to 25.5 keV with different intensities and gamma radiation of 88.04 keV [181]. Most of the emitted X-rays have an energy between 21.99 keV and 24.94 keV (21.99 keV (29.5%), 22.163 keV (55.7%), 24.912 keV (4.76%) and 24.943 keV (9.2%)) as shown in Table 9.1 and the mean energy of X-rays emitted from Cd-109 source is about 22.7 keV. Thus, the mean number of e-h pairs generated in the EDET-80 detector can be calculated using equation 5.1. As a result, an absorbed photon of mean energy ΔE=22.7 keV produces N_{eh}=6270 e-h pairs.

TABLE 9.1: Radiation emitted during the radioactive decay of Cd-109 [181].

Gammas from $^{109}_{48}\mathrm{Cd}$ (Half life: $T_{1/2}$=462.6 days)		
E_g(keV)	$I_g(\%)$	Decay Mode
88.04	3.61	electron capture (EC)
X-rays from $^{109}_{48}\mathrm{Cd}$		
E(keV)	I(%)	Assignement
2.634-3.750	9.2	X-rays L
21.99-22.163	85.2	X-rays Kα
24.912-25.511	16.814	X-rays Kβ

Taking into account the gain of the DEPFET in the linear region (i.e. gain of the low dynamic range region) calculated in section 6.2, g_q= 210.64 pA/electron, and the DCD gain setting k of the EDET-80, the charge N_{eh} created by a photon of ΔE produces a DEPFET current I_d given by

$$I_d = N_{eh} \times g_q \times k. \tag{9.1}$$

For gain setting $k = 1$, one photon produces on average I_d=6270 e^- × 210.64 pA/electron × 1=1.32 µA and for gain setting $k = 2$ it produces I_d=6270 e^- × 210.64 pA/electron × 2=2.64 µA. Our 8-bit DCD can only digitize a maximum current of 32 µA. Therefore, the digitization of I_d=2.64 µA results in a mean ADU of 21.12 ($\overline{\mathrm{ADU}}$ =21.12).

The experimental setup which we used to perform the measurements is illustrated in Figure 9.1. It shows that the EDET-80 detector prototype is irradiated from

the back side with radiation emitted from the Cd-109 radioactive source. This radiation is collimated using a tungsten collimator. We recorded 300 million frames; each was acquired in t=128 ns $\times$ (128/4)=4.096 µs and thus most of the captured frames are either empty or show a single hit due to the fast frame rate of the EDET-80 prototype and the low flux of the Cd-109 source. By processing these 300 million frames, we obtained the image and the energy spectrum of X-rays emitted from the Cd-109 radioactive source. To analyze the measured results, we performed additional simulations of the setup for comparison.

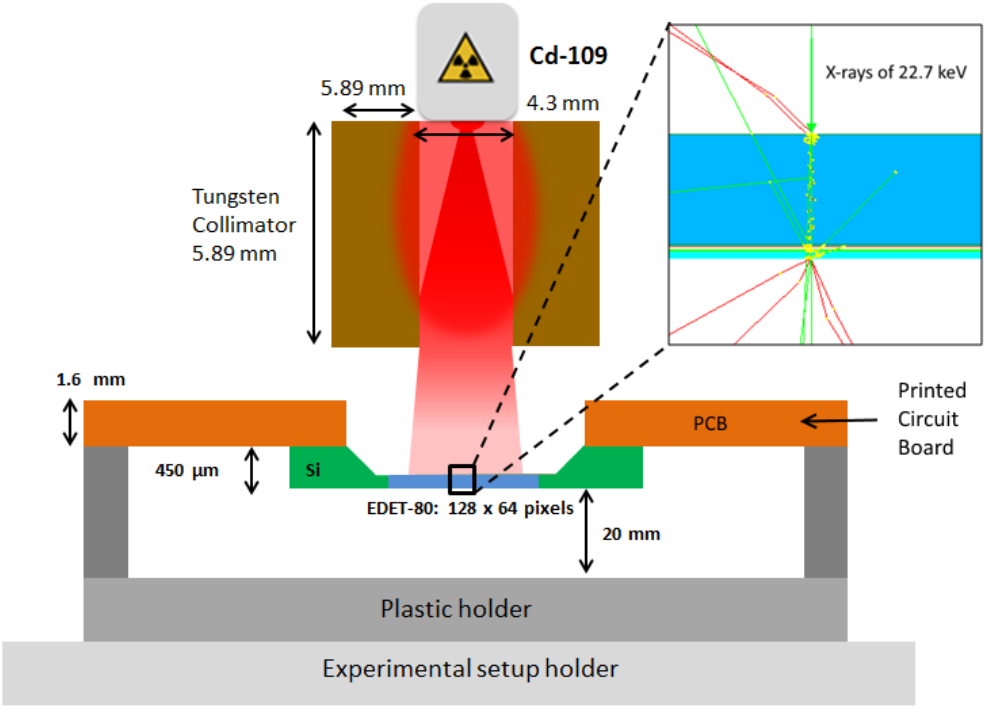

FIGURE 9.1: Illustration of the setup used to perform measurements and simulation with the EDET-80 prototype. The inset shows simulation of 1000 photons of 22.7 keV hitting the EDET-80 prototype. The green and red trajectories represent photons and electrons, respectively.

We simulated the same experimental setup as illustrated in Figure 9.1 to compare the measured and the simulated results obtained with the EDET-80 detector prototype. We recorded 30,000 simulated frames with the EDET-80 detector and Figure 9.2 shows examples of some simulated frames. The simulated and measured images of the Cd-109 radioactive source in terms of counts are presented in Figure 9.3.

The measured Cd-109 image shows that there are some pixels in the EDET-80 detector prototype, which do not detect any radiation, as can be seen in Figure 9.3. This surprising finding may raise questions about the hardware capabilities but it is confirmed that it is a software-related issue. The measured and simulated energy spectra of photons emitted from the Cd-109 radioactive source are illustrated in Figure 9.4. In this figure, each spectrum is normalized to its area and both results show a peak at 22 keV, but the 24 keV peak appearing in the simulated spectrum is not resolved in the measurement. The measured spectrum was recorded taking into account the gain calibration of each pixel, but it is still broader than that obtained from the simulation. This may be attributed to the contributions of additional noise such as leakage current and uncomplete clearing of the matrix, or the gain calibration of pixels is not accurate. These possible noise sources are not included in the simulation. Therefore, increasing the noise in the simulation by just 1 ADU results in the energy spectrum shown in Figure 9.5, which is in a very good agreement with the measured energy spectrum.

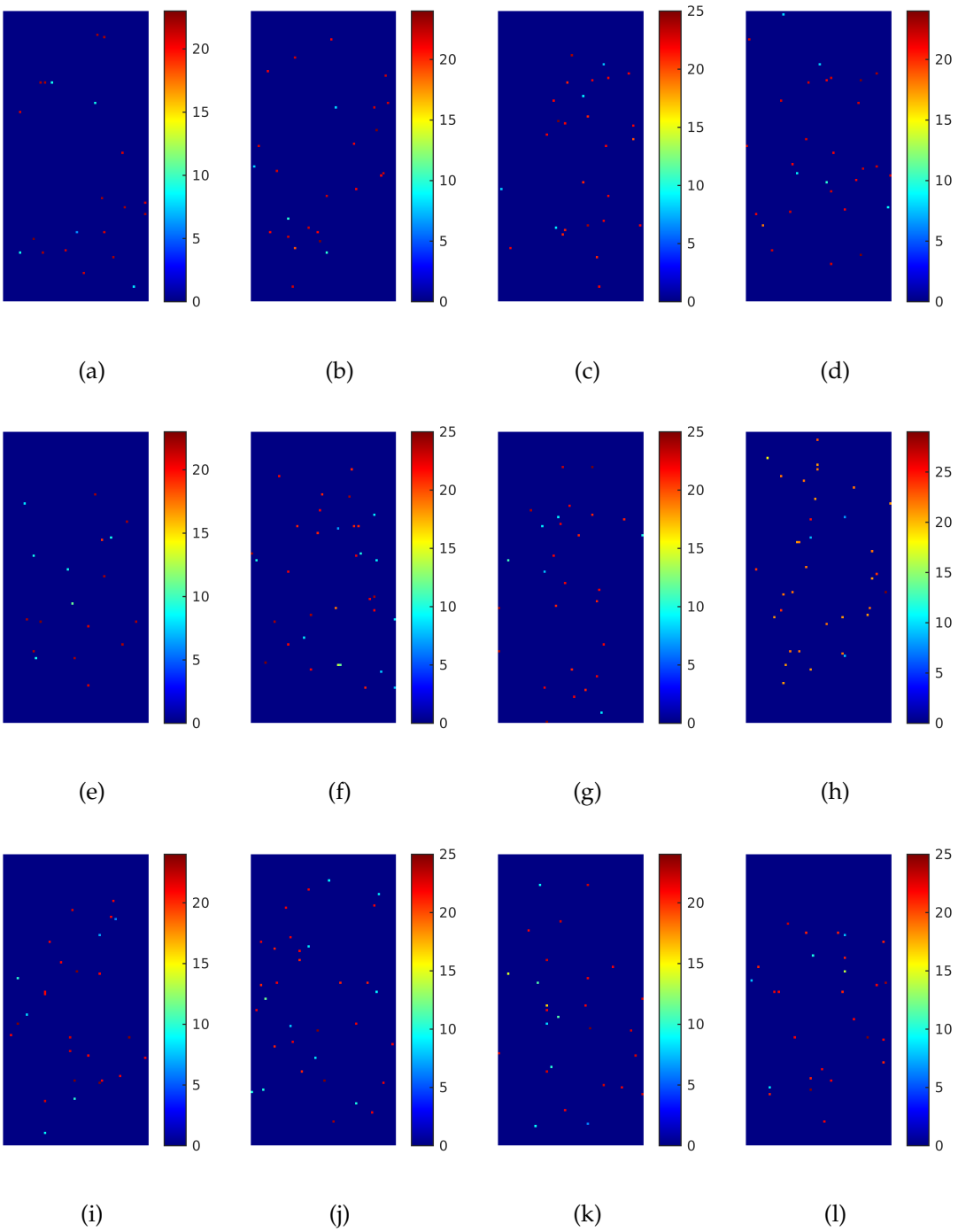

FIGURE 9.2: Example of simulated frames. The hits are in ADU.

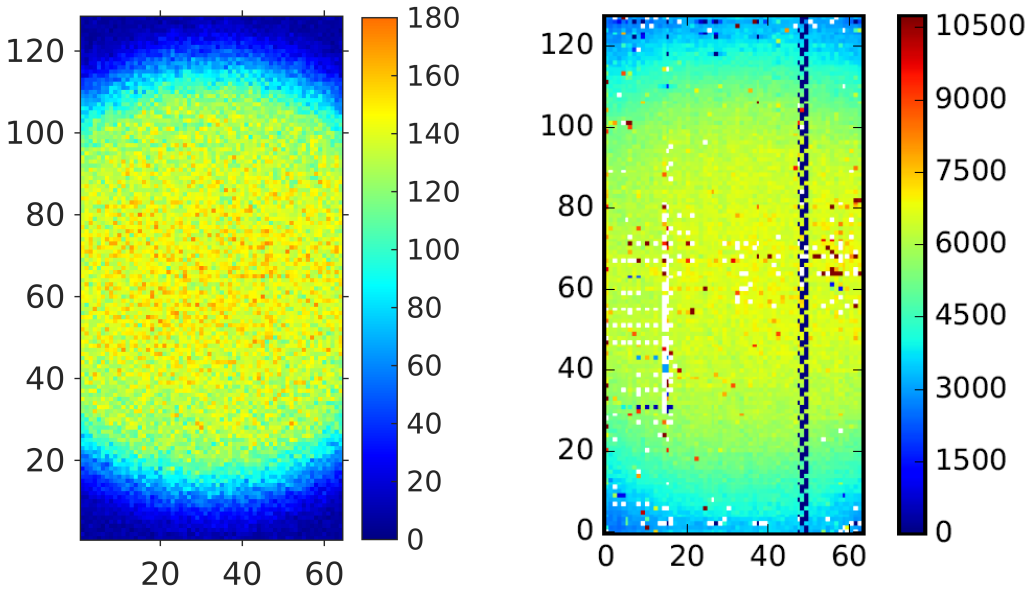

(a) (b)

FIGURE 9.3: (a) Simulation: Distribution of hits in the EDET-80 produced by photons emitted from the Cd-109 radioactive source. The simulated image is obtained from 30,000 frames, (b) Measurement: Distribution of hits in the EDET-80 produced by photons emitted from Cd-109 radioactive source. The measured image is obtained by summing up 3×10^8 frames.

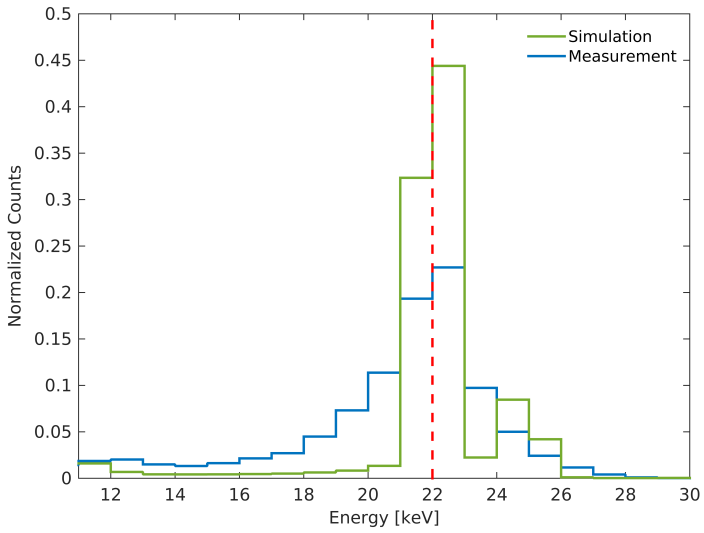

FIGURE 9.4: Simulated and measured energy spectrum of photons emitted from the Cd-109 radioactive source. Each spectrum is normalized to its area.

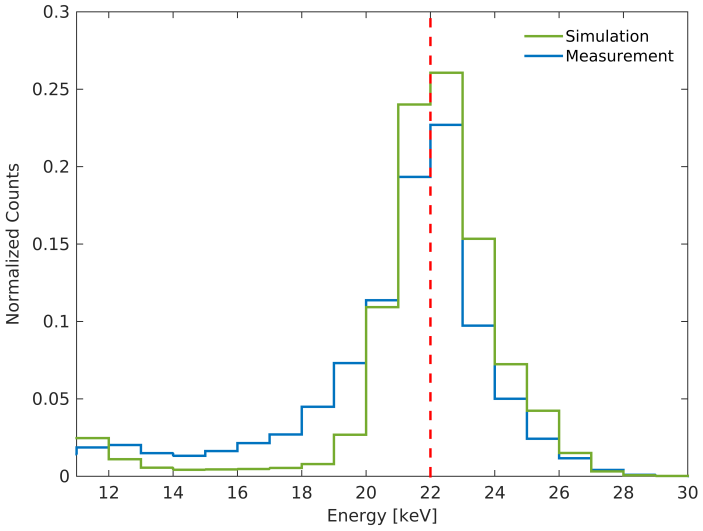

FIGURE 9.5: Simulated and measured energy spectrum of photons emitted from Cd-109 radioactive source. The noise in the simulation is increased by 1 ADU.

In the next section we will simulate and discuss the liquid cells employed in transmission electron microscopy to maintain the samples in their native hydrated environment using GEANT4 simulation toolkit.

Chapter 10

Liquid Cell Transmission Electron Microscopy

Water is one of the most important compounds indispensable to the existence of all living beings as it is the environment where the life takes place. Biological systems (e.g. living cells) consist of up to 80% water. The observation of the fast dynamic processes, such as dynamics of large proteins occurring in a hydrated environment requires not only fast direct electron detectors but also nanofluidic devices to maintain samples being investigated in near-native conditions. In recent years there has been growing interest in liquid cell electron microscopy, which has been applied in research fields such as chemistry, material science, biology, and physics. In addition, the rapid progress in their design and fabrication has enabled nanoscale resolution to be achieved [182, 183, 184, 185, 186], thus providing a promising pathway to explore dynamic events with impressive detail [187, 188, 189, 190, 191].

However, the most important limitation to liquid cell TEM resolution results from the fact that most liquid cells are still thick, up to several hundreds of nanometers of liquid. In addition, the encapsulating membranes typically consist of 50 nm thick silicon nitride Si_2N_3 [60, 61]. Thicker layers broaden the electron beam due to

the inelastic and elastic scattering events that degrade the SNR for biological specimens consisting of low-atomic number materials. Furthermore, inelastic scattering events lead to the energy spread of electrons exciting the sample, giving thus rise to the chromatic aberration of the objective lens. Studies have demonstrated that these issues are serious impediments to the attainable spatial resolution in liquid samples [58, 59], and hence thin liquid cells are of great interest. It is advantageous to have a liquid cell whose water layer and window thicknesses are less than the mean free path of electrons in these media. Such a thin sample makes it possible to perform phase-contrast imaging experiments [82], which require a partially coherent electron beam.

10.1 Top-Bottom Effect in Thick Liquid Cell TEM

It is essential to understand the factors restricting the liquid cell TEM spatial resolution such as the thickness of the water layer, the vertical position of objects inside the liquid cell and the thickness of silicon nitride membranes. Optimizing these parameters enables capturing liquid cell TEM images with better spatial resolution, which can enrich our understanding of the phenomena being investigated. Furthermore, new research areas can be explored such as the direct observation of biological processes in their native environments [192]. Figure 10.1 shows a liquid cell TEM to perform TEM imaging experiments in a hydrated state.

Here, we carried out Monte Carlo simulations to investigate the effect of using different materials and the thickness of the liquid cell on the TEM image quality. The same simulation toolkit described in chapter 5 was used. It should be noted that the simulation results presented here are obtained from the scattering contrast of the object being imaged and no phase effects are considered. One of the main physical processes degrading the image quality in thick liquid cells is the scattering

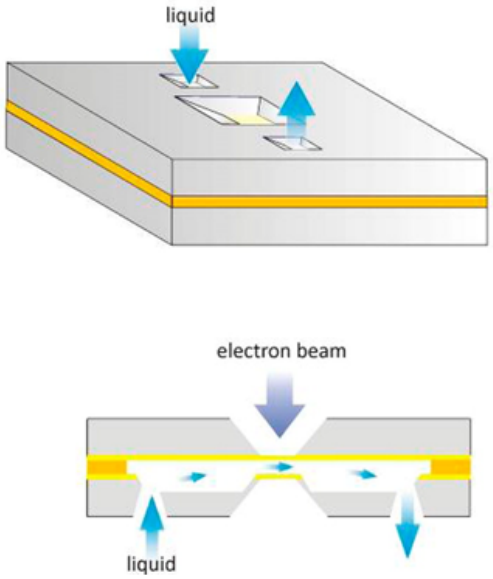

FIGURE 10.1: Liquid cell TEM and its cross-sectional view. Yellow color represents the silicon nitride windows and the orange color represents the liquid layer thickness [1].

of electrons [193, 171]. This effect sets a limit on the attainable image resolution especially for features positioned closer to the top window (i.e. at the electron-beam entrance side) in thick water cells. Consequently, the highest resolution can be achieved when the objects being imaged are positioned at the bottom window (i.e. at the electron-beam exit side) of the liquid cell and the resolution degrades as the object positions get closer to the top window [59]. This effect is called top-bottom effect which has been observed previously in TEM [62] as well as in STEM [194, 195, 196, 62, 197, 198].

We investigated the top-bottom effect in a liquid cell TEM composed of two silicon nitride membranes encapsulating a water layer and isolating it from the vacuum in a TEM. The thickness of the water layer and the silicon nitride membranes are 800 nm and 20 nm, respectively. An illustration of the simulation setup used to investigate the TEM images of gold nanoparticles within the liquid cell is shown in Figure 10.2.

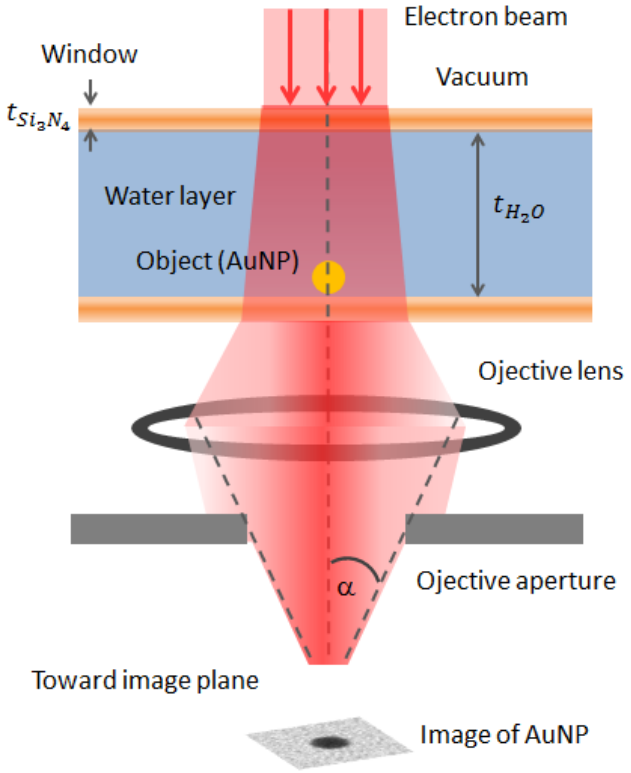

FIGURE 10.2: Illustration of the simulation setup used to investigate the images of nanoscale objects (e.g. AuNP) within a liquid water layer encapsulated between two silicon nitride windows. The gold nanoparticle is a perfect sphere, positioned at the bottom to obtain the highest spatial resolution and has a diameter of 20 nm. The thickness of water layer and silicon nitride windows are $t_{\mathrm{H_2O}}$=800 nm and $t_{\mathrm{Si_2N_3}}$=20 nm, respectively. Dimensions not to scale.

We positioned a spherical gold nanoparticle (AuNP) of 20 nm diameter at the top and then at the bottom of the cell, as shown in Figure 10.3. To capture the images of the AuNP within the liquid cell, we irradiated the liquid cell with an electron beam of 200 keV whose flux is 3 electrons per $\mathrm{\AA}^2$, which is still below the electron dose inducing radiation damage in beam-sensitive specimens [199, 200, 6]. Both elastic and inelastic scattering events were considered in the simulation. As a result, we obtained the energy E, positions (x, y, z) and the directions (u_x, u_y, u_z) of electrons exciting the liquid cell. We filtered electrons exiting the liquid cell depending on

their scattering angles by introducing an objective aperture and thus electrons with angles larger than 20 mrad were excluded. Here, the scattering contrast is simulated, the effects of chromatic and spherical aberration are neglected, which means that we operate an aberration corrected TEM providing the highest spatial resolution.

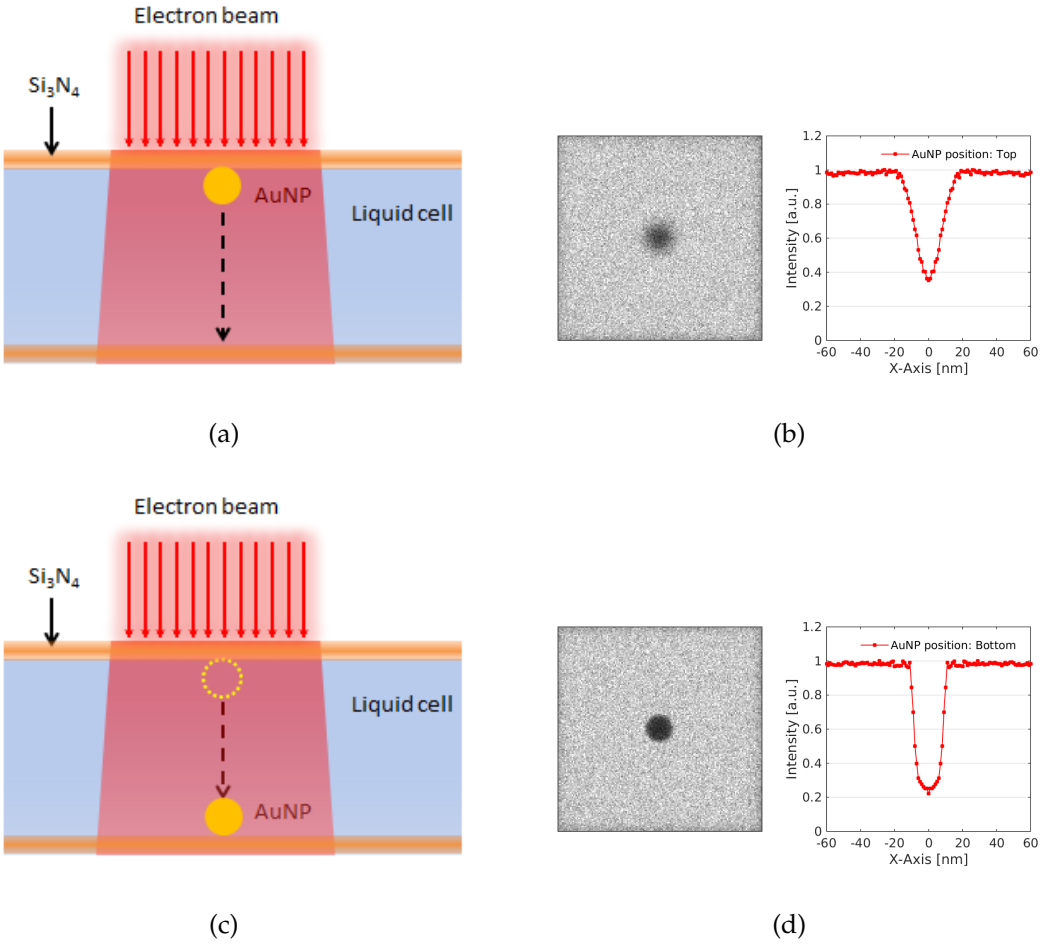

FIGURE 10.3: Illustration of a 20 nm-diameter AuNP at the top and bottom of a liquid cell consisting of 800 nm water layer and 20 nm Si_2N_3 windows. (a) AuNP is at the top and (b) the corresponding contrast image and mean radial profile. (c) AuNP is at the bottom and (d) the corresponding contrast image and mean radial profile. Dimensions not to scale in (a) and (c).

In the next step, we shifted the AuNP, located at the top, stepwise vertically down by a step size of 8 nm to explore the effect of the depth of AuNP within the liquid cell on the spatial resolution. As a result, 97 vertical positions of AuNP were simulated leading thus to "movie" of AuNP moving vertically from the top to the bottom of the liquid cell TEM. Figure 10.4 shows exemplary images and the corresponding radial profiles of AuNP positioned at different depths within the liquid cell.

Spatial resolution is defined here as the width of the signal distribution when it rises from 25% to 75% of the maximal signal ($x_{25\%} - x_{75\%}$) [82], as highlighted in Figure 10.5. A Gaussian distribution is fitted to the simulation data to find the peak, then $x_{25\%}$ and $x_{75\%}$ are determined from the interpolated simulation data. Our simulation results confirm the so-called top-bottom effect in liquid cell TEM and show that we obtained a better spatial resolution of the gold nanoparticle situated on the bottom (i.e. 2.04 nm) compared to that of the gold nanoparticle positioned at the top (i.e. 5.63 nm).

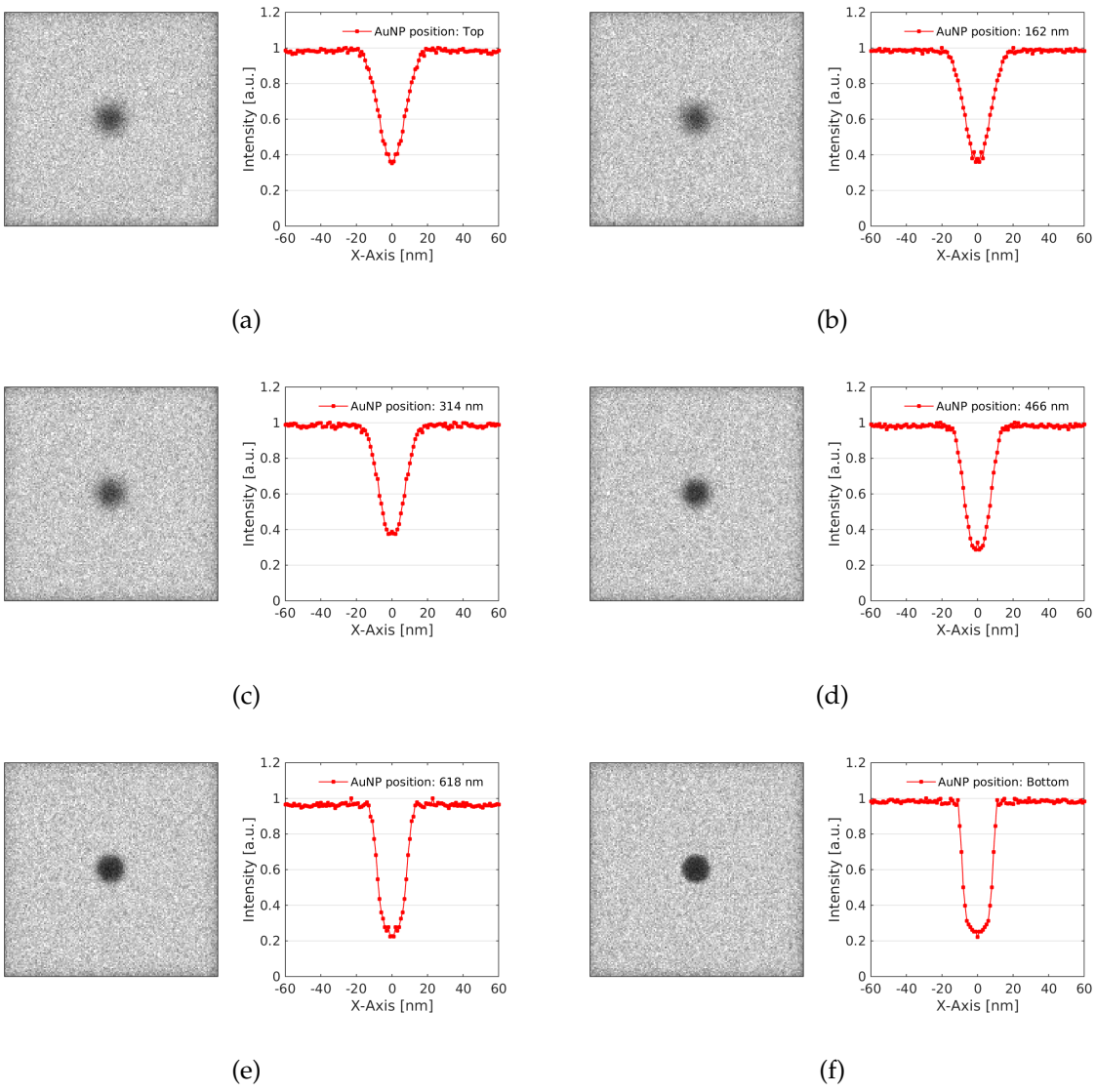

FIGURE 10.4: Top-bottom effect in the liquid cell TEM. Contrast images and normalized radial profiles of a 20 nm-diameter AuNP placed at different positions inside a liquid cell with regard to the electron beam entrance window. The liquid cell consists of 800 nm water layer and two 20 nm thick Si_2N_3 windows. (a) AuNP is placed at the top, (b) AuNP is placed at 152 nm, (c) AuNP is placed at 304 nm, (d) AuNP is placed at 456 nm, (e) AuNP is placed at 608 nm and (f) AuNP is placed at the bottom.

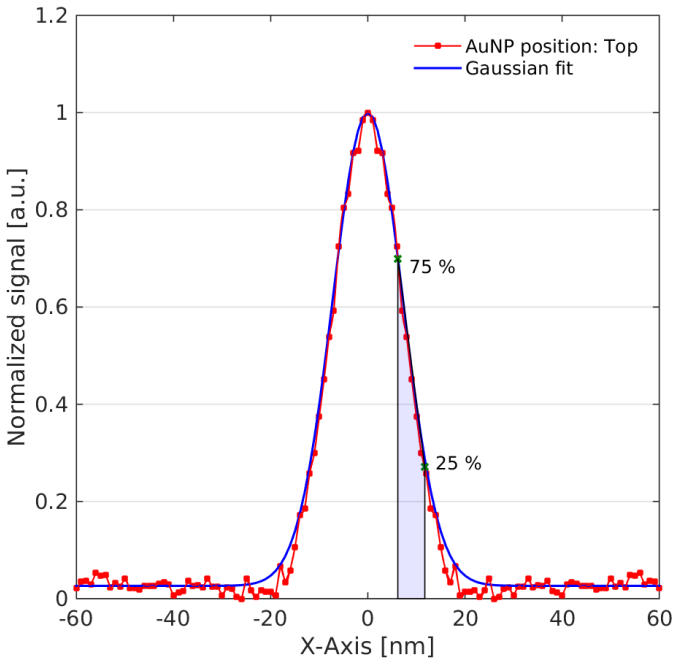

FIGURE 10.5: Calculation of the spatial resolution in a liquid cell TEM. The width of the shaded bar (i.e. $w = x_{25\%}$ - $x_{75\%}$) gives the achieved spatial resolution.

We compared the spatial resolution, which we obtained from simulation when the AuNP is placed at the top within the liquid cell with the theoretical spatial resolution given by [82]

$$x_0 = 1.05 \times 10^5 \sqrt{\frac{\rho}{A}} \frac{Z}{E} \frac{1 + \frac{E}{E_0}}{1 + \frac{E}{2E_0}} t^{1.5}. \tag{10.1}$$

Where

A: Atomic weight (for water A=18.01528 g.mol^{-1}, for Si_2N_3 A=20 g.mol^{-1}).

Z: Mean atomic number (for water Z=4.7 [171], for Si_2N_3 Z=10.6 [201]).

ρ: Density of liquid cell (for water ρ=1.0 g.cm^{-3}, for Si_2N_3 ρ=3.44 g.cm^{-3}).

E: Energy of incident electrons in eV.

E_0: Rest energy of electrons (E_0=511 keV).

t: Thickness of liquid cell in cm.

This equation takes into account relativistic effect, assumes a Gaussian broadening profile of the electron beam and considers only the elastic scattering events. It should be noted that it shows strong dependence of the spatial resolution on the liquid cell thickness. The theoretical spatial resolutions obtained from equation 10.1 for liquid cell investigated here (i.e. 800 nm water + 20 nm $\mathrm{Si_2N_3}$ windows) is given by

$$x_0^2 = x_0^2(\mathrm{H_2O}) + x_0^2(\mathrm{Si_3N_4}). \tag{10.2}$$

Using equation 10.1 and equation 10.2 we can theoretically calculate the achievable spatial resolution for different liquid cells and 200 keV electrons. The calculated and simulated spatial resolution for the AuNP placed at the top of the liquid cell consisting of an 800 nm thick water layer and 20 nm thick $\mathrm{Si_2N_3}$ windows are 4.84 nm and 5.63 nm, respectively. This slight discrepancy between simulation and theory could be attributed to the inelastic scattering events, which are not considered in the equation 10.1. In general, shifting the AuNP from the top to the bottom within a liquid cell results in an enhanced spatial resolution as can be seen in Figure 10.6 highlighting the variation of the spatial resolution as a function of the AuNP depth within the liquid cell. Interestingly, the spatial resolution at the top of the liquid cell is $\sim$5.63 nm and decreases to $\sim$2.04 nm when the AuNP is located at the bottom of the liquid cell. In other words, the spatial resolution improves by a factor of 2.76.

In the following, we will investigate the impact of the thickness and window materials of the liquid cell on the spatial resolution.

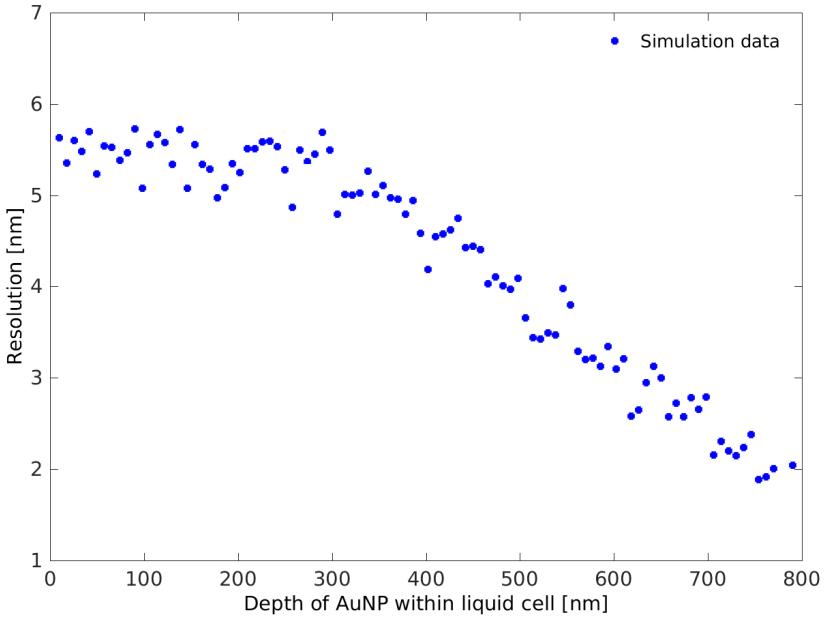

FIGURE 10.6: Spatial resolution as a function of vertical position of a 20 nm diameter AuNP within the liquid cell with respect to the top. The liquid cell consists of an 800 nm thick water layer and two 20 nm thick silicon nitride windows.

10.2 Graphene Liquid Cell for TEM

Window materials and the thickness of the liquid cell are very important parameters of liquid cell TEM experiments as thicker cells can not preserve reasonable image resolution. Commercially available liquid cells are still several hundreds of nanometers thick and consist of several tens of nanometers thick Si_2N_3 membrane [60, 61], which may restrict their capabilities to achieve atomic-scale resolution and perform spectroscopic experiments. However, an additional gain in the spatial resolution of liquid cell TEM experiments can be obtained by replacing the silicon nitride windows used in the conventional liquid cells by windows composed of low-atomic number materials such as graphene [202, 203, 204, 205]. Due to the exceptional impermeability and mechanical properties of graphene [206], graphene windows can be made thinner than silicon nitride windows. Thinner graphene

windows have the advantage of being more transparent to the electron beam, thus delivering significantly better spatial resolution than the conventional liquid cells made of thick silicon nitride windows. Therefore, graphene liquid cells offer exciting opportunities to explore a wide range of samples in biology, chemistry, and physics. For example, graphene liquid cells offer brilliant promises to study real time dynamics of biological systems (e.g. DNA dynamics) [207], dynamic behavior of nanoscale liquids [208] and nanocrystal growth [209] with excellent resolution. Graphene liquid cells are also suitable for exploring beam sensitive samples and allow for atomic-resolution imaging experiments [210]. Despite these advantages of graphene liquid cells, graphene is fragile and it is very difficult to manufacture liquid cells with graphene windows.

Here we simulated liquid cells with carbon windows instead of graphene, which is available in terms of number of layers. We repeated the same simulations we carried out for a liquid cell with silicon nitride windows replacing the 20 nm thick Si_2N_3 windows by carbon windows. In the first step, a 10 nm thick carbon window was chosen to study the impact of window material on the achievable spatial resolution in a relatively thick liquid cell (e.g. 800 nm thick water layer). The spatial resolution as a function of depth of the AuNP within the investigated liquid cell are calculated from the results shown in Figure 10.7. The obtained spatial resolutions are summarized in Table 10.1 and compared with the theoretical spatial resolution calculated from equation 10.1.

Replacing the 20 nm thick Si_2N_3 windows with 10 nm thick carbon windows in a liquid cell of 800 nm thick water layer improves only the spatial resolution if the gold nanoparticle is positioned closer to the top or bottom of the cell. In these positions, the material of the liquid cell windows matters. For other positions inside the cell, especially near the middle, there are almost no improvements in the

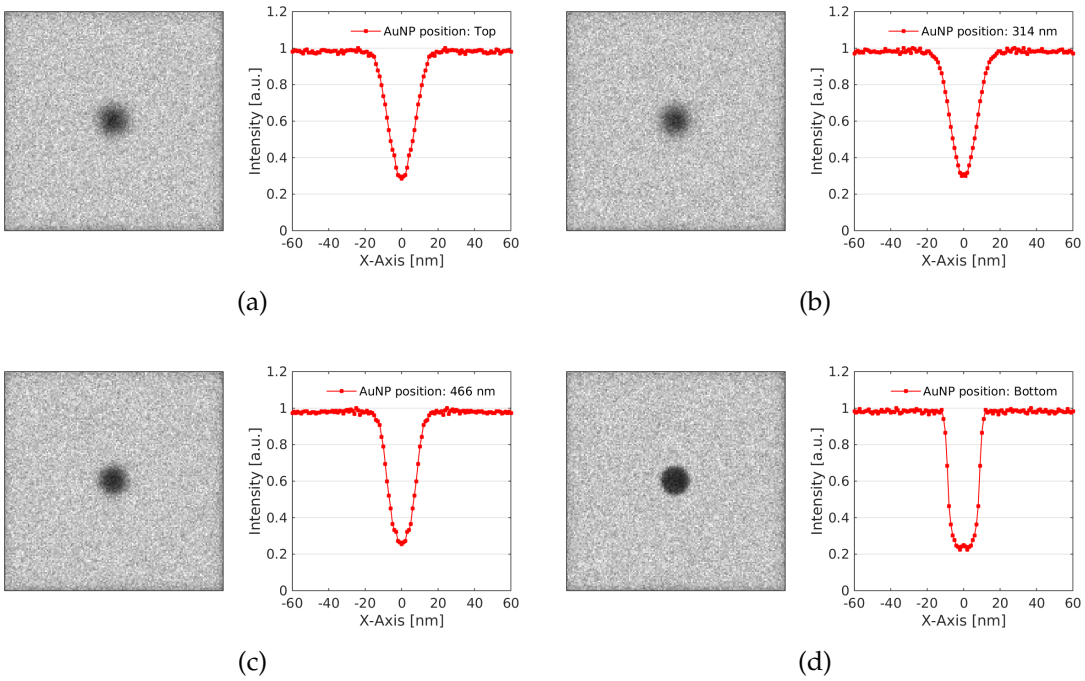

FIGURE 10.7: Top-bottom effect in liquid cell TEM. Contrast images and normalized radial profiles of a 20 nm diameter AuNP placed at different positions inside a liquid cell with regard to the electron beam entrance window. The liquid cell consists of 800 nm water layer and 10 nm carbon windows. (a) AuNP is placed at the top, (b) AuNP is placed at 314 nm, (c) AuNP is placed at 466 nm and (d) AuNP is placed at the bottom.

TABLE 10.1: Achievable spatial resolution (in nm) in an 800 nm thick liquid cell with Si_2N_3 and carbon windows.

AuNP position / LC TEM	Top_{theory}	Top_{sim}	314 nm	466 nm	Bottom
LC with 20 nm Si_2N_3	4.84	5.63	5.01	4.03	2.13
LC with 10 nm carbon	4.84	5.10	4.98	3.80	1.64

spatial resolution, and thus the window material is not a limiting factor for spatial resolution. This is due to the fact that the 800 nm thickness of the water layer is thick enough to be the dominant factor degrading the spatial resolution in liquid cell. Further improvements in the spatial resolution can be realized by reducing the liquid layer thickness from 800 nm to 400 nm, as can be seen in Figure 10.8 and Table 10.2. As a result, the resolution improves by a factor of 2.94 and 1.15 at the top and bottom, respectively. Importantly, the highest gain in spatial resolution goes to the AuNP located at the top.

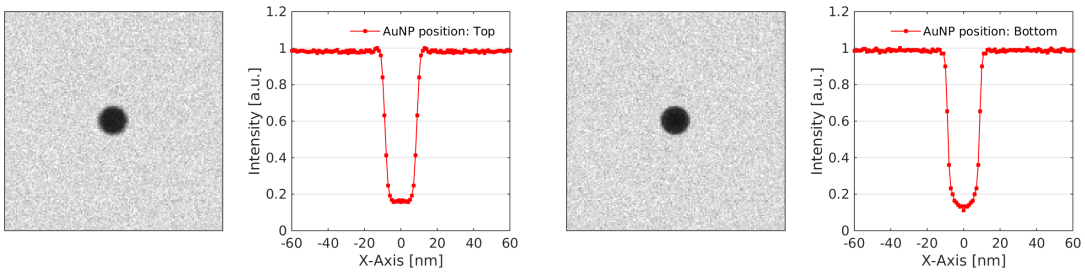

(a) (b)

FIGURE 10.8: Contrast images and normalized radial profiles of a 20 nm-diameter AuNP placed at the top and bottom of a liquid cell. The liquid cell consists of 400 nm water layer and 10 nm carbon windows. (a) AuNP is placed at the top and (b) AuNP is placed at the bottom of the liquid cell.

TABLE 10.2: Achievable spatial resolution (in nm) in a thin liquid cell with 10 nm carbon windows.

LC TEM \ AuNP position	Top_{theory}	Top_{sim}	Bottom
400 nm water layer + 10 nm carbon	1.71	1.73	1.43

For graphene liquid cells, the graphene windows and the liquid layer are very thin—thinner than those previously discussed. Thus, in the further investigation we thinned down the liquid layer and carbon window to 200 nm and 2 nm, respectively. The obtained results are shown in Figure 10.9 and Table 10.3. From these results, it is clear that thin liquid cell with carbon windows deliver better results than a thick liquid cell. Interestingly, the top-bottom effect does not exist in such a thin liquid cell and the same spatial resolution (about 1 nm) is achieved regardless of the vertical position of the AuNP within the liquid cell. This can be explained by the fact that the liquid cell thickness is comparable to the total mean free path of 200 keV electrons in water, which is about 200 nm [211]. This in an interesting finding revealing the boundary of the top-bottom effect in liquid cell TEM.

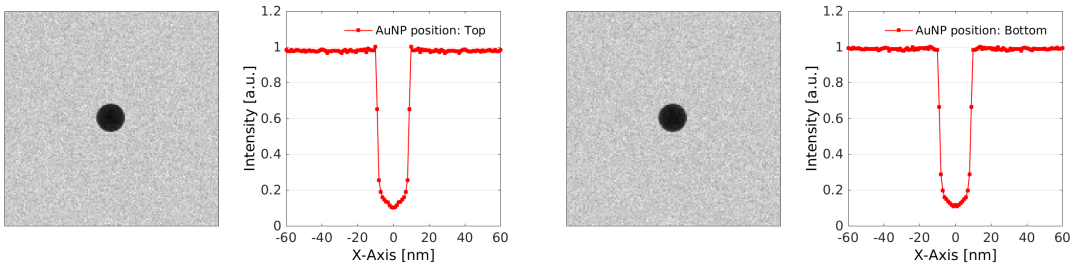

(a) (b)

FIGURE 10.9: Contrast images and normalized radial profiles of a 20 nm-diameter AuNP placed at the top and bottom of a liquid cell. The liquid cell consists of 200 nm water layer and 2 nm carbon windows. (a) AuNP is placed at the top and (b) AuNP is placed at the bottomof the liquid cell.

TABLE 10.3: Achievable spatial resolution (in nm) in a thin liquid cell with 2 nm carbon windows.

AuNP position / LC TEM	Top_{theory}	Top_{sim}	Bottom
200 nm water layer + 2 nm carbon	0.60	1.0	1.0

Chapter 11

Conclusions and Outlook

A new detector technology can play a key role in addressing the challenges related to the direct observation of fast dynamics occurring in biological systems by means of transmission electron microscopy. Therefore, the EDET-80 has been developed with the aim to pave the way for accessing the "hitherto" inaccessible "terra incognita". EDET-80 is a megapixel direct electron detector operating with a maximum frame rate of ∼80 kHz. Such a frame rate enables the EDET-80 to capture movies of fast biological or other processes resolvable by an 80 kHz frame rate or 12.5 µs frame time using transmission electron microscope. To develop this detector, we utilized an innovative DEPFET technology capable of compressing signal at the sensor level—DEPFET with non-linear response. After its successful use in high energy physics and astrophysics detectors, the DEPFET technology is about to be introduced for the first time in the EDET-80 detector devoted to fast TEM imaging applications. This novel technology enables the user of the EDET-80 to perform low-electron dose imaging experiments ensuring single electron resolution. In addition, its enhanced charge handling capacity (i.e. large dynamic range) allows for capturing high contrast images with less readout noise and, most importantly, in four dimensions—real-space and -time TEM imaging applications.

The most important feature of the EDET-80 is its capability to read out the full

frame in approximately 12.5 µs (exactly 12.8 µs), which is a major achievement. This unprecedented speed enables the EDET-80 to capture a wide range of dynamical phenomena and is sufficient to record even protein folding dynamics, thereby opening up new imaging possibilities relevant for investigating biological systems in their natural environments with nanometer-scale spatial resolution.

Simulation studies were very beneficial during the development process of the EDET-80 as they improved its imaging capabilities, facilitated and reduced the fabrication cycles. In this work, Monte Carlo simulation studies led to an optimized detector model realizing significant improvements in all aspects of the imaging performance. We achieved an advanced detector design minimizing the background signal created in the sensor by electron scattering events (e.g. backscattered electrons). This background signal is a serious issue in direct electron detectors as it degrades the spatial resolution, the detection efficiency of the detector and causes additional radiation damage in the detector. Moreover, the simulation results presented here provide useful information for detector developers and can be readily adapted to advance the performance of other direct electron detectors.

One concern arises when imaging biological samples—radiation damage. This is of particular interest in TEM experiments as it is a fundamental limitation to the spatial resolution of beam-sensitive specimens such as biological systems and soft matter. EDET-80 directly detects electrons with excellent detection efficiency and fast frame rate, which may outrun the onset of the radiation damage effects. The simulation results demonstrate that the EDET-80 detector offers significant SNR, good MTF and high DQE at all spatial frequency. These quantities reveal the enhanced imaging performance of this detector. The calculation of DQE proved that the EDET-80 detector can carry out both low and high-dose imaging experiments with a significant SNR using an appropriate DCD gain setting. For example, at

DCD gain settings of k=2, k=1 and k=0.667, the mean DQE of EDET-80 operating in integrating mode reaches about 71$\%$ at low electron dose (i.e. $0.001-0.3$ electron per pixel per frame at 300 keV). This excellent DQE of EDET-80 operating in integrating mode is very useful not only for efficiently using the low electron dose to capture high quality images of biological specimens in their native hydrated environment utilizing nanofluidic devices, but also for making it possible to capture the images of beam-sensitive specimens with reduced radiation hardness. The comparison of the DQE of the EDET-80, as a function of fraction of Nyquist spatial frequency, to the DQE of current state-of-the-art detectors used in transmission electron microscopy reveals that we are on the way to achieve a competitive direct electron detector, but at much higher temporal resolution. EDET-80 is based on the DEPFET technology and susceptible to radiation damage. This issue becomes even more serious if the EDET-80 is exposed to an inhomogeneous radiation, which is fortunately not the case in the TEM imaging experiments. Experimental and simulation investigations regrading this issue are still on-going. Primary electrons may also damage the readout electronics of the detector. Therefore, an efficient shielding was designed and optimized to protect the readout electronics of the detector against possible radiation damage from the electron beam.

So far, we have produced the first prototype of the EDET-80 consisting of 128 by 64 pixels. The central function of this prototype is to test the detector performance and find solutions for possible challenges. The initial experimental results delivered by the EDET-80 prototype prove the capability of this detector to capture frames with $\sim$80 kHz. One concern about this prototype is the DEPFET Movie Chip (DMC), which is a fully customized ASIC chip needed to store temporary the recorded frames. This chip is still under review after a production run, which was not successful.

The investigation of biological samples exhibiting dynamic behaviors requires not only fast detectors, but also an appropriate liquid cell TEM to maintain samples being investigated in their native hydrated environment. We simulated different liquid cells exposed to the electron beam of 200 keV. The obtained results demonstrate the top-bottom effect observed in liquid cell TEM and reveal the boundary of this effect. The highest spatial resolution was attained when the object being imaged is located at the bottom of liquid cell or the thickness of liquid cell is comparable to the mean free path of 200 keV electrons.

It is worth mentioning that the EDET-80 may deliver much better results when operating in a counting mode as this mode can potentially increase the DQE close to 100%. This can be achieved by minimizing the noise contribution to the total detected signal, thus pushing the information per scattering event to its theoretical limit. The potential of the counting mode has not been investigated in this work as it is not useful for fast dynamics.

Further work foreseen also includes the full assembly of the four EDET-80 quadrants and the integration of a novel laser annealing technique in the detector system. This technique is a part of the EDET-80 project and has been developed at MPSD to mitigate the possible radiation damage of the EDET-80 detector and consequently increase the sensor lifetime by an order of magnitude. After adapting the EDET-80 detector to the TEM environment, we would like to carry out one of the great experiments in science—the direct observation of dynamic processes occurring in biological systems in real-space and -time.

Acknowledgements

It is challenging to pursue a PhD in detector development for transmission electron microscopy applications, especially when one starts almost from scratch. Therefore, these accomplishments would not have been possible without the collaborative efforts of the Halbleiterlabor (HLL) of the Max Planck Society in Munich and the ASIC- and Detector Laboratory Group of the Institute for Data Processing and Electronics (IPE) in Karlsruhe Institute of Technology (KIT). These challenges enabled me to enrich my knowledge, gain extensive experience and skills. The pleasure of scientific research is related to the challenges we face. I see challenges as a source of motivation, empowerment, and inspiration. They also give a value to our results and without challenges the life becomes boring.

To my mentors and defense committee

Foremost, I would like to express my deep and respectful gratitude to my supervisor Prof. R. J. Dwayne Miller for giving me the opportunity to join his group as a PhD candidate, for his continuous support, excellent guidance and immense knowledge. He was always available for discussion and support even in weekends. I have had the pleasure to be one of his PhD students.

I would also like to sincerely thank Prof. Günter Huber for co-supervising me, for the constructive discussions, suggestions and useful meetings during my PhD.

I am also very thankful to the group leader Dr. Sascha Epp for the fruitful discussions, valuable hints and suggestions. He was very helpful, cooperative and

always available for discussion whenever I asked him.

Besides my advisors, I am deeply grateful for Prof. Dr. Daniela Pfannkuche, Prof. Dr. Nils Huse and Prof. Dr. Arwen Pearson for serving as memebers of my defense committee.

To my colleagues

It was a great advantage to have a person like Dr. Fabian Westermeier, who was my officemate and also involved in this research project. I would like to cordially thank him for the time we spent together and for his enthusiasm, his availability, and productive discussions.

My appreciations go also to the engineer Djodje Gitaric for constructing CAD designs of the EDET-80 detector. He was always ready and happy to help. I highly appreciate his contributions to this research project.

I would like to thank Dr. Günther Kassier for the constructive discussions about liquid cell TEM.

Furthermore, my sincere thanks go to all past and present group members of Prof. Dwayne Miller, the administrative staff and all people working at the Max Planck Institute for the Structure and Dynamics of Matter (MPSD), Center for Free Electron Laser (CFEL) and DESY including scientist and non-scientist staffs. I wish also to extend my thanks to the university of Hamburg and MPSD for offering me the resources to complete this thesis. I would like to acknowledge the valuable MTF software tool developed by RAI labs.

I would like to gratefully acknowledge our collaborators at IPE in Karlsruhe Institute of Technology (KIT), Prof. Ivan Peric the head of ASIC- and Detector Laboratory, and all the members of the Halbleiterlabor in Munich for their wonderful

collaboration. I owe my deepest gratitude to you for your great support, excellent cooperation and for the opportunities you have given me to perform measurements at your laboratory in Munich. Special thanks go to Dr. Eduard Prinker for his support and help during the measurements at HLL. Without his support, the experimental part of this thesis would be impossible.

I would like to sincerely thank our coordinators Dr. Sonja Utermann, Dr. Julia Quante, and Dr. Neda Lotfiomran and all the members of IMPRS-UFAST and PIER graduate school for supporting me and for the useful scientific and social events they offered.

To my family

My special thanks go to my family, which is the central source of my strength and motivation. Therefore, I would like to take this opportunity to express my deepest gratitude to my parents for their infinite love, continual support and encouragement and for making me the person that I am today. I thank you and love you with all my heart.

I wish I could find the proper words to thank my loving and supportive wife and my two beloved daughters. They faithfully supported me with love, encouraged me, were always by my side in all of my pursuits, inspired me and motivated me to follow my dreams. Due to the far distance between us, I could only see my wife and my two daughters at the weekend during my PhD study. Therefore, I have to kindly thank my family for being patient until I completed my Ph.D. I love you all and I appreciate your patience and your support! Words can not express how grateful I am to you.

To my friends

Last, but not least, there are also my friends and roommates, who supported me during my PhD, offered me advice and provided me happy opportunities to refresh my mind outside the research. I hope I can find the proper words to thank them. I want to close up by thanking you all for the excellent support and the great time we had.

To those I forgot to thank and acknowledge. I hope I can find proper words to say sorry and also thank you. A huge thank you to you all.

Bibliography

[1] C. Mueller, M. Harb, J. R. Dwyer, R. J. D. Miller, *The Journal of Physical Chemistry Letters* **4**, 2339 (2013).

[2] N. J. Zaluzec, *Ultramicroscopy* **151**, 240 (2015).

[3] P. Tiemeijer, M. Bischoff, B. Freitag, C. Kisielowski, *Ultramicroscopy* **114**, 72 (2012).

[4] S. Pennycook, M. Varela, C. Hetherington, A. Kirkland, *MRS Bulletin* **31**, 36 (2006).

[5] M. Linck, *et al.*, *Physical Review Letters* **117**, 076101 (2016).

[6] U. M. Mirsaidov, H. Zheng, Y. Casana, P. Matsudaira, *Biophysical Journal* **102**, L15 (2012).

[7] M. Marini, *et al.*, *Nanoscale* **9**, 2768 (2017).

[8] P. Roingeard, P.-I. Raynal, S. Eymieux, E. Blanchard, *Reviews in Medical Virology* **29**, e2019 (2018).

[9] F. Vale, A. Correia, B. Matos, J. F. Moura Nunes, A. Matos, *Microscopy: Science, Technology, Applications and Education* (2010).

[10] N. d. Jonge, D. B. Peckys, G. J. Kremers, D. W. Piston, *Proceedings of the National Academy of Sciences* **106**, 2159 (2009).

[11] A. Al-Amoudi, *et al.*, *The EMBO Journal* **23**, 3583 (2004).

[12] A. Merk, *et al.*, *Cell* **165**, 1698 (2016).

[13] B.-R. Zhou, *et al.*, *Nature Communications* **10**, 2301 (2019).

[14] Y. Liu, S. Gonen, T. Gonen, T. O. Yeates, *Proceedings of the National Academy of Sciences* **115**, 3362 (2018).

[15] J. Mak, A. de Marco, *Retrovirology* **15**, 23 (2018).

[16] P. Goldberg-Oppenheimer, O. Regev, *Small* **3**, 1894 (2007).

[17] J. E. Evans, N. D. Browning, *Microscopy* **62**, 147 (2013).

[18] P. Chien, L. M. Gierasch, *Molecular Biology of the Cell* **25**, 3474 (2014).

[19] B. Jin, M. L. Sushko, Z. Liu, C. Jin, R. Tang, *Nano Letters* **18**, 6551 (2018).

[20] N. D. Browning, J. E. Evans, *Liquid Cell Electron Microscopy* (Cambridge University Press, Cambridge, 2016), pp. 456–475.

[21] E. Nakamura, *Angewandte Chemie International Edition* **52**, 236 (2012).

[22] E. A. Stach, *Materials Today* **11**, 50 (2008).

[23] E. Stach, *et al.*, *Microscopy and Microanalysis* **19**, 392 (2013).

[24] B. Schuler, H. Hofmann, *Current Opinion in Structural Biology* **23**, 36 (2013).

[25] D. M. Dias, A. Ciulli, *Progress in Biophysics and Molecular Biology* **116**, 101 (2014).

[26] I. R. Kleckner, M. P. Foster, *Biochimica et Biophysica Acta (BBA) - Proteins and Proteomics* **1814**, 942 (2011).

[27] W. E. King, *et al.*, *Journal of Applied Physics* **97**, 111101 (2005).

[28] A. Faruqi, R. Henderson, *Current Opinion in Structural Biology* **17**, 549 (2007).

[29] A. R. Faruqi, S. Subramaniam, *Quarterly Reviews of Biophysics* **33**, 1 (2000).

[30] J. C. H. Spence, J. M. Zuo, *Review of Scientific Instruments* **59**, 2102 (1988).

[31] J. M. Zuo, *Microscopy Research and Technique* **49**, 245 (2000).

[32] L. Jin, *et al.*, *Journal of Structural Biology* **161**, 352 (2008).

[33] J. L. Hart, *et al.*, *Scientific Reports* **7** (2017).

[34] Falcon 3EC Direct Detection Detector, Next-generation Falcon with Electron Counting | Upgrades and Accessories | Thermo Fisher Scientific, https://www.fei.com/accessories/falcon-3ec-direct-electron-detector/ (Accessed: 09.2019).

[35] Contact | Gatan, Inc., http://www.gatan.com/contact (Accessed: 09.2019).

[36] DE-64–Direct Electron, https://www.directelectron.com/products/de-64/ (Accessed: 09.2019).

[37] Advanced Microscopy Techniques, http://www.amtimaging.com/www11/english/product_e.html (Accessed: 10.2019).

[38] M. Krajnak, D. McGrouther, D. Maneuski, V. O. Shea, S. McVitie, *Ultramicroscopy* **165**, 42 (2016).

[39] J. Schmidt, *et al.*, *Journal of Instrumentation* **9**, P10008 (2014).

[40] TVIPS - Octalab, http://www.octalab.com/?cat=8 (Accessed: 10.2019).

[41] N. Kimmel, *et al.*, *Advances in X-ray Free-Electron Lasers: Radiation Schemes, X-ray Optics, and Instrumentation*, T. Tschentscher, D. Cocco, eds. (SPIE, Prague, Czech Republic, 2011).

[42] Clarkvision: Digital Camera Review and Sensor Performance Summary, https://clarkvision.com/imagedetail/digital.sensor.performance.summary/ (Accessed: 09.2019).

[43] T. Abe, *et al.*, Belle II technical design report (2010). ArXiv:1011.0352 [physics.ins-det].

[44] T. Abe, *et al.*, *Progress of Theoretical and Experimental Physics* **2013**, 3A001 (2013).

[45] H. Sahoo, Measurements of CP Violation in B Meson decays at Belle (2011). ArXiv:1410.5093 [hep-ex].

[46] M. Kobayashi, T. Maskawa, *Progress of Theoretical Physics* **49**, 652 (1973).

[47] K. Kanazawa, *Nuclear and Particle Physics Proceedings* **273-275**, 204 (2016).

[48] C. Marinas, *Journal of Instrumentation* **7**, C02029 (2012).

[49] S. Furletov, *Journal of Instrumentation* **7**, C01014 (2012).

[50] M. Lemarenko, *The Belle II DEPFET Pixel Vertex Detector: Development of a Full-Scale Module Prototype*, Ph.D. thesis, University of Bonn (2013).

[51] C. Lacasta, *Proceedings of 22nd International Workshop on Vertex Detectors — PoS(Vertex2013)* (Sissa Medialab, 2014).

[52] F. Lütticke, *Journal of Instrumentation* **8**, C02006 (2013).

[53] J. Kemmer, G. Lutz, *Nuclear Instruments and Methods in Physics Research Section A: Accelerators, Spectrometers, Detectors and Associated Equipment* **253**, 365 (1987).

[54] H.-G. Moser, *Nuclear Instruments and Methods in Physics Research Section A: Accelerators, Spectrometers, Detectors and Associated Equipment* **831**, 85 (2016).

[55] M. Porro, *et al.*, *IEEE Transactions on Nuclear Science* **59**, 3339 (2012).

[56] S. Agostinelli, *et al.*, *Nuclear Instruments and Methods in Physics Research Section A: Accelerators, Spectrometers, Detectors and Associated Equipment* **506**, 250 (2003).

[57] J. Allison, *et al.*, *IEEE Transactions on Nuclear Science* **53**, 270 (2006).

[58] N. de Jonge, N. D. Browning, J. E. Evans, S. W. Chee, F. M. Ross, *Liquid Cell Electron Microscopy* (Cambridge University Press, Cambridge, 2016), pp. 164–188.

[59] N. de Jonge, L. Houben, R. E. Dunin-Borkowski, F. M. Ross, *Nature Reviews Materials* **4**, 61 (2018).

[60] E. A. Ring, D. B. Peckys, M. J. Dukes, J. P. Baudoin, N. de Jonge, *Journal of Microscopy* **243**, 273 (2011).

[61] N. de Jonge, M. Pfaff, D. B. Peckys, *Advances in Imaging and Electron Physics* (Elsevier, 2014), pp. 1–37.

[62] L. Reimer, M. Ross-Messemer, *Ultramicroscopy* **21**, 385 (1987).

[63] R. F. Egerton, *Physical Principles of Electron Microscopy : An Introduction to TEM, SEM, and AEM* (Springer, Switzerland, 2016).

[64] D. Williams, *Transmission Electron Microscopy : A Textbook for Materials Science* (Springer, New York, 2009).

[65] L. Reimer, *Energy-Filtering Transmission Electron Microscopy* (Springer, Berlin & New York, 1995).

[66] D. Andrews, *Comprehensive Nanoscience and Technology* (Boston Elsevier, Amsterdam, 2010).

[67] X. Zou, S. Hovmoller, P. Oleynikov, *Electron Crystallography: Electron Microscopy and Electron Diffraction (International Union of Crystallography Texts on Crystallography)* (Oxford University Press, Oxford & New York, 2011).

[68] P. J. Brown, A. G. Fox, E. N. Maslen, M. A. O'Keefe, B. T. M. Willis, *International Tables for Crystallography* (International Union of Crystallography, 2006), pp. 554–595.

[69] F. M. Ross, *Liquid Cell Electron Microscopy* (Cambridge University Press, New York, 2017).

[70] R. L. Zhigang, *Industrial applications of electron microscopy* (Marcel Dekker, New York, 2003).

[71] T. Jevremovic, *Nuclear principles in engineering* (Springer, New York & London, 2009).

[72] H. Bethe, *Annalen der Physik* **397**, 325 (1930).

[73] F. Bloch, *Annalen der Physik* **408**, 285 (1933).

[74] W. Leo, *Techniques for Nuclear and Particle Physics Experiments : a How-to Approach* (Springer Berlin Heidelberg, Berlin & Heidelberg, 1994).

[75] O. Pooth, *CMS Silicon Strip Tracker* (Vieweg+Teubner, Wiesbaden, 2010).

[76] L. Landau, *J. Phy.(USSR)* **8**, 201 (1944).

[77] T. Ferbel, *Experimental Techniques in High-Energy Nuclear and Particle Physics* (World Scientific, New Jersey, 1991).

[78] S. N. Ahmed, *Physics and Engineering of Radiation Detection; 2nd ed.* (Elsevier, Amsterdam, 2014).

[79] M. Knoll, E. Ruska, *Zeitschrift für Physik* **78**, 318 (1932).

[80] P. J. Mohr, D. B. Newell, B. N. Taylor, *Journal of Physical and Chemical Reference Data* **45**, 043102 (2016).

[81] L. D. Broglie, *Annales de Physique* **10**, 22 (1925).

[82] L. Reimer, H. Kohl, *Transmission Electron Microscopy* (Springer, New York, 2008).

[83] W. Zhou, R. Apkarian, Z. L. Wang, D. Joy, *Scanning Microscopy for Nanotechnology* (Springer New York, 2006), pp. 1–40.

[84] J. M. Zuo, J. C. Spence, *Advanced Transmission Electron Microscopy : Imaging and Diffraction in Nanoscience* (Springer, New York, 2017).

[85] G. McMullan, S. Chen, R. Henderson, A. Faruqi, *Ultramicroscopy* **109**, 1126 (2009).

[86] A. R. Faruqi, G. McMullan, *Quarterly Reviews of Biophysics* **44**, 357 (2011).

[87] H. Ayato, N. Mori, J. Miyahara, T. Oikawa, *Journal of Electron Microscopy* **39**, 444 (1990).

[88] T. Martin, A. Koch, *Journal of Synchrotron Radiation* **13**, 180 (2006).

[89] G. Y. Fan, M. H. Ellisman, *Journal of Microscopy* **200**, 1 (2000).

[90] A. Faruqi, H. Andrews, *Nuclear Instruments and Methods in Physics Research Section A: Accelerators, Spectrometers, Detectors and Associated Equipment* **392**, 233 (1997).

[91] A. Faruqi, H. Andrews, R. Henderson, *Nuclear Instruments and Methods in Physics Research Section A: Accelerators, Spectrometers, Detectors and Associated Equipment* **367**, 408 (1995).

[92] T. Gomi, K. Koshida, T. Miyati, J. Miyagawa, H. Hirano, *Journal of Digital Imaging* **19**, 362 (2006).

[93] R. R. Meyer, A. Kirkland, *Ultramicroscopy* **75**, 23 (1998).

[94] E. Samei, M. J. Flynn, *Medical Physics* **30**, 608 (2003).

[95] R. N. Clough, G. Moldovan, A. I. Kirkland, *Journal of Physics: Conference Series* **522**, 012046 (2014).

[96] T. Hansen, *Controlled Atmosphere Transmission Electron Microscopy : Principles and Practice* (Springer International Publishing, New York, 2016).

[97] S. Simon, *Methods in Chemosensory Research* (CRC Press, Boca Raton, 2002).

[98] J. Janesick, G. Putnam, *Annual Review of Nuclear and Particle Science* **53**, 263 (2003).

[99] D. Contarato, P. Denes, D. Doering, J. Joseph, B. Krieger, *Physics Procedia* **37**, 1504 (2012).

[100] G. McMullan, A. Faruqi, D. Clare, R. Henderson, *Ultramicroscopy* **147**, 156 (2014).

[101] B. E. Bammes, R. H. Rochat, J. Jakana, D.-H. Chen, W. Chiu, *Journal of Structural Biology* **177**, 589 (2012).

[102] N. Grigorieff, *eLife* **2**, e00573 (2013).

[103] R. S. Ruskin, Z. Yu, N. Grigorieff, *Journal of Structural Biology* **184**, 385 (2013).

[104] V. Migunov, *et al.*, *Scientific Reports* **5** (2015).

[105] P. Roberts, J. Chapman, A. MacLeod, *Ultramicroscopy* **8**, 385 (1982).

[106] A. Faruqi, R. Henderson, M. Pryddetch, P. Allport, A. Evans, *Nuclear Instruments and Methods in Physics Research Section A: Accelerators, Spectrometers, Detectors and Associated Equipment* **546**, 170 (2005).

[107] J. Ulrici, *et al.*, *Nuclear Instruments and Methods in Physics Research Section A: Accelerators, Spectrometers, Detectors and Associated Equipment* **465**, 247 (2001).

[108] P. Klein, *et al.*, *Nuclear Instruments and Methods in Physics Research Section A: Accelerators, Spectrometers, Detectors and Associated Equipment* **454**, 152 (2000).

[109] E. Gatti, P. Rehak, *Nuclear Instruments and Methods in Physics Research* **225**, 608 (1984).

[110] H.-G. Moser, L. Andricek, R. H. Richter, G. Liemann, *PoS* **VERTEX2007**, 013 (2007).

[111] O. Alonso, *et al.*, *IEEE Transactions on Nuclear Science* **60**, 1457 (2013).

[112] L. Andricek, G. Lutz, M. Reiche, R. Richter, *IEEE Nuclear Science Symposium. Conference Record (IEEE Cat. No.03CH37515)* (IEEE, 2003).

[113] S. Rummel, *Nuclear Instruments and Methods in Physics Research Section A: Accelerators, Spectrometers, Detectors and Associated Equipment* **699**, 51 (2013).

[114] S. Rummel, L. Andricek, H. G. Moser, R. Richter, *Journal of Instrumentation* **4**, P03003 (2009).

[115] C. Marinas, *Nuclear Instruments and Methods in Physics Research Section A: Accelerators, Spectrometers, Detectors and Associated Equipment* **731**, 31 (2013).

[116] S. Wolfel, *et al.*, *IEEE Transactions on Nuclear Science* **54**, 1311 (2007).

[117] G. Lutz, M. Porro, S. Aschauer, S. Wölfel, L. Strüder, *Sensors* **16**, 608 (2016).

[118] M. Trimpl, *Design of a Current Based Readout Chip and Development of DEPFET Pixel Prototype System for the ILC Vertex Detector*, Ph.D. thesis, University of Bonn (2005).

[119] J. Ulrici, *et al.*, *Nuclear Instruments and Methods in Physics Research Section A: Accelerators, Spectrometers, Detectors and Associated Equipment* **547**, 424 (2005).

[120] L. Strüder, *Nuclear Instruments and Methods in Physics Research Section A: Accelerators, Spectrometers, Detectors and Associated Equipment* **436**, 53 (1999).

[121] J. Treis, *et al.*, *High Energy, Optical, and Infrared Detectors for Astronomy III*, D. A. Dorn, A. D. Holland, eds. (SPIE, 2008).

[122] J. Velthuis, *et al.*, *Nuclear Instruments and Methods in Physics Research Section A: Accelerators, Spectrometers, Detectors and Associated Equipment* **579**, 685 (2007).

[123] L. Andricek, *et al.*, *IEEE Nuclear Science Symposium Conference Record* (IEEE, 2005).

[124] P. Lechner, *et al.*, *IEEE Nuclear Science Symposium Conference Record* (IEEE, 2011).

[125] J. G. K.Gärtner, T. Koprucki, *User Documentation Oskar3* (Wias-Berlin, March, 2011).

[126] A. Ritter, *et al.*, *Nuclear Instruments and Methods in Physics Research Section A: Accelerators, Spectrometers, Detectors and Associated Equipment* **730**, 79 (2013).

[127] K. Henzler-Wildman, D. Kern, *Nature* **450**, 964 (2007).

[128] L. A. Baker, J. L. Rubinstein, *Methods in Enzymology* (Elsevier, San Diego, 2010), pp. 371–388.

[129] V. E. Cosslett, *Journal of Microscopy* **113**, 113 (1978).

[130] R. M. Glaeser, *Journal of Ultrastructure Research* **36**, 466 (1971).

[131] R. M. Glaeser, K. A. Taylor, *Journal of Microscopy* **112**, 127 (1978).

[132] M. Karuppasamy, F. K. Nejadasl, M. Vulovic, A. J. Koster, R. B. G. Ravelli, *Journal of Synchrotron Radiation* **18**, 398 (2011).

[133] R. Egerton, *Ultramicroscopy* **127**, 100 (2013).

[134] http://geant4.web.cern.ch/ (Accessed: 03.07.2019).

[135] Geant4 Collaboration, *Physics Reference Manual Documentation, Release 10.3* (2017).

[136] S. Incerti, *et al.*, The Geant4-DNA project (2009). ArXiv:0910.5684 [physics.bio-ph].

[137] Geant4 Collaboration, *Geant4 User's Guide for Application Developers, Version Geant4.10.3* (2016).

[138] C. Thiam, *Dosimétrie en Radiothérapie et Curiethérapie par Simulation Monte-Carlo GATE sur Grille Informatique*, Ph.D. thesis, Université Blaise Pascal-Clermont-Ferrand II (2007).

[139] B. Schmidt, *Ion Beams in Materials Processing and Analysis* (Springer, Vienna & New York, 2013).

[140] S. Meroli, www.cern.ch/meroli.

[141] P. Grob, *et al.*, *Ultramicroscopy* **133**, 1 (2013).

[142] G. McMullan, *et al.*, *Ultramicroscopy* **109**, 1144 (2009).

[143] A.-C. Milazzo, *et al.*, *Ultramicroscopy* **104**, 152 (2005).

[144] A.-C. Milazzo, *et al.*, *Ultramicroscopy* **110**, 741 (2010).

[145] G. Moldovan, X. Li, P. Wilshaw, A. I. Kirkland, *EMC 2008 14th European Microscopy Congress 1–5 September 2008, Aachen, Germany* (Springer Berlin & Heidelberg), pp. 85–86.

[146] M. Kuijper, *et al.*, *Journal of Structural Biology* **192**, 179 (2015).

[147] C. Frujinoiu, R. R. Brey, *Radiation Protection Dosimetry* **97**, 223 (2001).

[148] S. Horiguchi, M. Suzuki, T. Kobayashi, H. Yoshino, Y. Sakakibara, *Applied Physics Letters* **39**, 512 (1981).

[149] J. Beletic, *Scientific detectors for astronomy 2005 : Explorers of the Photon Odyssey* (Springer, Dordrecht, 2006).

[150] S. W. Smith, The Scientist and Engineer's Guide to Digital Signal Processing, http://www.dspguide.com/copyrite.htm (Accessed: 18.02.2019).

[151] J. L. Lancaster, B. Hasegawa, *Fundamental Mathematics and Physics of Medical Imaging* (CRC Press, Taylor & Francis Group, Boca Raton, 2016).

[152] S. E. Reichenbach, *Optical Engineering* **30**, 170 (1991).

[153] M. Estribeau, P. Magnan, *Detectors and Associated Signal Processing*, J.-P. Chatard, P. N. J. Dennis, eds. (SPIE, 2004).

[154] A. Walter, S. Lashansky, *Sensors, Cameras, and Systems for Scientific/Industrial Applications VII*, M. M. Blouke, ed. (SPIE, 2006).

[155] S. N. Lashansky, S. Mansbach, M. J. Berger, T. Karasik, M. Bin-Nun, *Infrared Imaging Systems: Design, Analysis, Modeling, and Testing XIX*, G. C. Holst, ed. (SPIE, 2008).

[156] E. Samei, M. J. Flynn, D. A. Reimann, *Medical Physics* **25**, 102 (1998).

[157] P. F. Judy, *Medical Physics* **3**, 233 (1976).

[158] Y.-H. Kao, M. Albert, A.-K. Carton, H. Bosmans, A. D. A. Maidment, *Medical Imaging 2005: Physics of Medical Imaging*, M. J. Flynn, ed. (SPIE, 2005).

[159] Carl E Ravin Advanced Imaging Laboratories, `http://deckard.duhs.duke.edu/railabs/index.html` (Accessed: 21.08.2019).

[160] M. Veale, *et al.*, *Nuclear Instruments and Methods in Physics Research Section A: Accelerators, Spectrometers, Detectors and Associated Equipment* **767**, 218 (2014).

[161] C. Allwork, *et al.*, *IEEE Transactions on Nuclear Science* **59**, 1563 (2012).

[162] H. Zeller, *et al.*, *24th International Conference Image and Vision Computing New Zealand* (IEEE, 2009).

[163] G. Pellegrini, *et al.*, *IEEE Transactions on Nuclear Science* **53**, 361 (2006).

[164] G. Zanella, R. Zannoni, *Nuclear Instruments and Methods in Physics Research Section A: Accelerators, Spectrometers, Detectors and Associated Equipment* **359**, 474 (1995).

[165] D. N. Sitter, J. S. Goddard, R. K. Ferrell, *Applied Optics* **34**, 746 (1995).

[166] J. Janesick, *Scientific Charge-Coupled Devices* (SPIE Press, Bellingham & Wash, 2001).

[167] M. Lachaine, B. G. Fallone, *Medical Physics* **25**, 1186 (1998).

[168] G. McMullan, A. Faruqi, R. Henderson, *Methods in Enzymology* (Elsevier, 2016), pp. 1–17.

[169] M. Pan, *European Microscopy Congress 2016: Proceedings* (2016).

[170] A. Rose, *Advances in Electronics and Electron Physics Volume 1* (Elsevier, 1948), pp. 131–166.

[171] N. de Jonge, N. Poirier-Demers, H. Demers, D. B. Peckys, D. Drouin, *Ultramicroscopy* **110**, 1114 (2010).

[172] B. E. Bammes, J. Jakana, M. F. Schmid, W. Chiu, *Journal of Structural Biology* **169**, 331 (2010).

[173] G. P. Henderson, L. Gan, G. J. Jensen, *PLoS ONE* **2**, e749 (2007).

[174] S. W. Hui, D. F. Parsons, *Science* **184**, 77 (1974).

[175] V. A. J. V. Lint, *Mechanisms of Radiation Effects in Electronic Materials* (Wiley, 1980).

[176] F. Hartmann, *Evolution of silicon sensor technology in particle physics* (Springer, Berlin, 2009).

[177] C. Leroy, *Principles of radiation interaction in matter and detection* (World Scientific, Singapore Hackensack, NJ, 2012).

[178] H. Spieler, *Semiconductor Detector Systems* (Oxford University Press, Oxford New & York, 2005).

[179] A. Ritter, *Radiation Hardness Studies for DEPFETs in Belle II*, Ph.D. thesis, Technical University of Munich (2013).

[180] E. Sirtl, *Advanced Materials* **2**, 109 (1990).

[181] L. E. S.Y.F. Chu, R. Firestone, Lund/lbnl decay data search, version 2.0, http://nucleardata.nuclear.lu.se/toi/ (1999 (Accessed: 13.02.2019)).

[182] G. Guzzinati, *et al.*, *Materials* **11**, 1304 (2018).

[183] G. Zhu, *et al.*, *Chemical Communications* **49**, 10944 (2013).

[184] E. Sutter, *et al.*, *Nature Communications* **5** (2014).

[185] D. J. Kelly, *et al.*, *Nano Letters* **18**, 1168 (2018).

[186] H. Zheng, S. A. Claridge, A. M. Minor, A. P. Alivisatos, U. Dahmen, *Nano Letters* **9**, 2460 (2009).

[187] J. E. Evans, K. L. Jungjohann, N. D. Browning, I. Arslan, *Nano Letters* **11**, 2809 (2011).

[188] C. Luo, C. Wang, X. Wu, J. Zhang, J. Chu, *Small* **13**, 1604259 (2017).

[189] S. Keskin, *et al.*, *The Journal of Physical Chemistry Letters* **6**, 4487 (2015).

[190] S. W. Chee, U. Anand, G. Bisht, S. F. Tan, U. Mirsaidov, *Nano Letters* **19**, 2871 (2019).

[191] J. Yang, S. B. Alam, L. Yu, E. Chan, H. Zheng, *Micron* **116**, 22 (2019).

[192] J. Park, *et al.*, *Nano Letters* **15**, 4737 (2015).

[193] N. de Jonge, F. M. Ross, *Nature Nanotechnology* **6**, 695 (2011).

[194] R. Ramachandra, H. Demers, N. de Jonge, *Applied Physics Letters* **98**, 093109 (2011).

[195] P. Gentsch, H. Gilde, L. Reimer, *Journal of Microscopy* **100**, 81 (1974).

[196] R. Ramachandra, H. Demers, N. de Jonge, *Microscopy and Microanalysis* **19**, 93 (2013).

[197] H. Demers, N. Poirier-Demers, D. Drouin, N. de Jonge, *Microscopy and Microanalysis* **16**, 795 (2010).

[198] H.-B. Zhang, C. Yang, A. Takaoka, *Review of Scientific Instruments* **76**, 056106 (2005).

[199] F. Joachim, *Three-Dimensional Electron Microscopy of Macromolecular Assemblies* (Oxford University Press, Oxford & New York, 2006).

[200] J. Z. Chen, *et al.*, *Journal of Structural Biology* **161**, 92 (2008).

[201] N. de Jonge, W. C. Bigelow, G. M. Veith, *Nano Letters* **10**, 1028 (2010).

[202] N. Mohanty, M. Fahrenholtz, A. Nagaraja, D. Boyle, V. Berry, *Nano Letters* **11**, 1270 (2011).

[203] M. R. Hauwiller, J. C. Ondry, A. P. Alivisatos, *Journal of Visualized Experiments* (2018).

[204] D. J. Kelly, *et al.*, *Nano Letters* **18**, 1168 (2018).

[205] S. M. Ghodsi, C. M. Megaridis, R. Shahbazian-Yassar, T. Shokuhfar, *Small Methods* **3**, 1900026 (2019).

[206] J. S. Bunch, *et al.*, *Nano Letters* **8**, 2458 (2008).

[207] Q. Chen, *et al.*, *Nano Letters* **13**, 4556 (2013).

[208] J. Yang, S. B. Alam, L. Yu, E. Chan, H. Zheng, *Micron* **116**, 22 (2019).

[209] J. M. Yuk, *et al.*, *Science* **336**, 61 (2012).

[210] C. Wang, Q. Qiao, T. Shokuhfar, R. F. Klie, *Advanced Materials* **26**, 3410 (2014).

[211] S. Incerti, *et al.*, *Medical Physics* **45**, e722 (2018).